




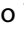













## Gyro-spintronic material science using vorticity gradient in solids

Yukio Nozaki <sup>a,b</sup>, Hiroaki Sukegawa <sup>c</sup>, Shinichi Watanabe <sup>a</sup>, Seiji Yunoki<sup>d</sup>, Taisuke Horaguchi <sup>a</sup>, Hayato Nakayama <sup>a</sup>, Kazuto Yamanoi <sup>a</sup>, Zhenchao Wen <sup>c</sup>, Cong He <sup>c</sup>, Jieyuan Song <sup>c</sup>, Tadakatsu Ohkubo <sup>c</sup>, Seiji Mitani <sup>c</sup>, Kazuki Maezawa <sup>a</sup>, Daichi Nishikawa <sup>a</sup>, Shun Fujii <sup>a</sup>, Mamoru Matsuo <sup>d,e,f,g</sup>, Junji Fujimoto <sup>e,h</sup> and Sadamichi Maekawa <sup>d</sup>

<sup>a</sup>Department of Physics, Keio University, Yokohama, Japan;

<sup>b</sup>Center for Spintronics Research Network, Keio University, Yokohama, Japan;

<sup>c</sup>Research Center for Magnetic and Spintronic Materials, National Institute for Materials Science, Tsukuba, Ibaraki, Japan;

<sup>d</sup>Center for Emergent Matter Science (CEMS), RIKEN, Center for Emergent Matter Science (CEMS), Wako, Saitama, Japan;

<sup>e</sup>Kavli Institute for Theoretical Sciences, University of Chinese Academy of Sciences, Beijing, China;

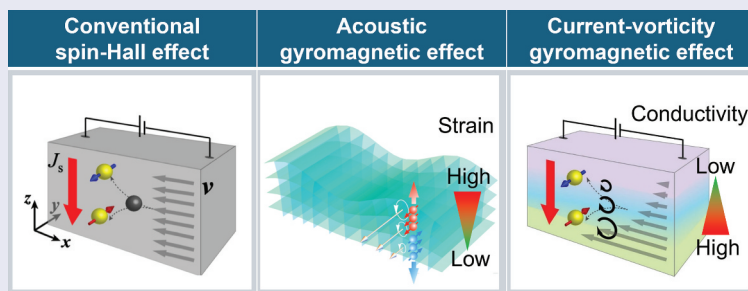
<sup>f</sup>CAS Center for Excellence in Topological Quantum Computation, University of Chinese Academy of Sciences, Beijing, China;

<sup>g</sup>Advanced Science Research Center, Japan Atomic Energy Agency, Tokai, Japan;

<sup>h</sup>Department of Electrical Engineering, Electronics, and Applied Physics, Saitama University, Saitama, Japan

### ABSTRACT

We present a novel method for generating spin currents using the gyromagnetic effect, a phenomenon discovered over a century ago. This effect, crucial for understanding the origins of magnetism, enables the coupling between various macroscopic rotational motions and electron spins. While higher rotational speeds intensify the effect, conventional mechanical rotations, typically, below 10,000 RPM, produce negligible results comparable to geomagnetic fluctuations, limiting applied research. Our studies demonstrate that spin current generation comparable to that of rare metals can be achieved through atomic rotations induced by GHz-range surface acoustic waves and the rotational motion of conduction electrons in metallic thin films with nanoscale gradient modulation of electrical conductivity. These effects, termed the acoustic gyromagnetic effect and the current-vorticity gyromagnetic effect, are significant in different contexts. The acoustic gyromagnetic effect is notable in high-conductivity materials like aluminum and copper, which are more abundant than conventional spintronics materials with strong spin-orbit interactions (SOIs). Conversely, the current-vorticity gyromagnetic effect requires a large conductivity gradient to produce current vorticity efficiently. This is achieved by using composition gradient structures from highly conductive metals to poorly conductive oxides or semiconductors. Consequently, unlike traditional strong-SOI materials, we can create highly efficient spin current generators with low energy dissipation due to reduced Joule loss.



We present an innovative method to generate spin currents using the gyromagnetic effect, an essential concept in magnetism. Our approach utilizes non-uniform spin-dependent scattering in GHz-range surface acoustic waves and the rotational motion of conduction electrons in metallic thin films with nanoscale conductivity gradients to produce spin currents. This research highlights two key mechanisms: the acoustic gyromagnetic effect in abundant, highly conductive materials like aluminum and copper, and the current-vorticity gyromagnetic effect in structures with large conductivity gradients, such as those transitioning from metals to oxides or semiconductors. Unlike conventional spintronics materials with strong spin-orbit interactions, our method enables efficient spin current generation with significantly lower energy dissipation. This advancement opens new avenues for spintronics, applying ubiquitous materials and reducing Joule losses, thereby enhancing device performance and energy efficiency.

### IMPACT STATEMENT

Our innovative method generates efficient spin currents via gyromagnetic effect using abundant materials with minimal energy loss, offering a significant advancement in spintronics by reducing reliance on rare, strong-SOI materials.

### ARTICLE HISTORY

Received 4 August 2024

Revised 9 October 2024

Accepted 6 November 2024

### KEYWORDS

Spin current; gyromagnetic effect; surface acoustic wave; gradient material; spintronics

1. Introduction

Fundamental electric devices such as transistors, random-access memory (RAM), and logic elements, which are essential for advanced information society, have improved in performance according to Moore Law [1]. However, the miniaturization of electronic devices leads to a serious problem in energy dissipation due to Joule heating. Recently, spin currents that carry spin angular momentum without electric current have been intensely studied to address Joule heating problems in electronic devices. For instance, spin current mediated spin-transfer torque (STT) [2–4] and spin-orbit torque (SOT) [5–9] for magnetization switching are being actively explored as recording methods for high-speed, energy-efficient magnetoresistive random-access memory (MRAM) [10–17]. Additionally, the concept of spin transistors, where the information carrier is switched from charge to spin, is also investigated to overcome the miniaturization limits of conventional transistor technology. However, spin transistors encounter significant challenges, such as inefficient spin injection and difficulty in their room-temperature operation.

Conventional theories of spin current generation in nonmagnetic metals are commonly based on spin-orbit interactions (SOI) derived from uniform spin-dependent scattering effects within materials or at interfaces and surfaces. The strength of SOI is notably large only in certain heavy metals with large atomic numbers, such as platinum, tantalum, tungsten, and bismuth. This restricts material choice in spintronics devices, leading to material limits of spin current generation.

To address this issue, an alternative principle for spin current generation using non-uniform spin-dependent scattering effects, which is not considered in conventional spintronics theory, has gained significant attention. As shown in Figure 1, there are two

pathways to solve this problem: spin current generation using the acoustic gyromagnetic effect and the current-vorticity gyromagnetic effect. It has been demonstrated that Rayleigh waves propagating on the surface of an elastic material can induce spin currents even in common metals like copper, comparable to those generated by traditional methods using strong SOI in heavy metals [18,19]. According to a microscopic theory considering the effects of curved spaces [20], spin current generation using Rayleigh waves is attributed to the dynamic and spatially varying spin-dependent scattering effects caused by lattice point displacement in copper crystals. This phenomenon, associated with the emergent magnetic field produced by lattice point rotation, is regarded as the ‘acoustic’ gyromagnetic effect, which will be discussed in Section 3.

Another effect, the ‘current-vorticity’ gyromagnetic effect, will be discussed in Section 4. It is based on the static and non-uniform scattering of electron spins in composition gradient materials, where electrical conductivity changes gradually along the film thickness. When an electric field is applied along the film plane, the vorticity of electric current is formed due to the gradient of electrical conductivity. This current vorticity produces an emergent magnetic field via the gyromagnetic effect. Finally, the gradient of the emergent magnetic field generates spin currents. These gyromagnetic effects are pronounced in non-magnetic materials with high electrical conductivity, making common metals like Al and Cu suitable for spin current generation, unlike conventional methods based on spin-orbit interactions in specific materials.

This paper is organized as follows: Section 2 reviews the theory of spin current generation via spin-vorticity coupling, an extension of the gyromagnetic effect to local electronic systems, and the use of its non-

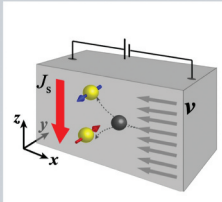
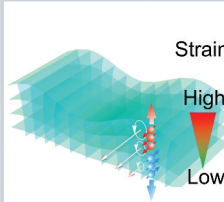
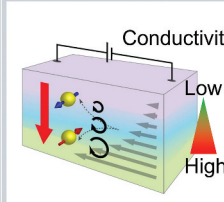
	Conventional spin-Hall effect	Acoustic gyromagnetic effect	Current-vorticity gyromagnetic effect
Charge-to-spin conversion			
Scattering source	Spin-orbit interaction (SOI)	Rotating atoms	Rotating electrons
Temporal and spatial feature	Static & uniform	Dynamic & non-uniform	Static & non-uniform
Materials	Pt, W, Ta, Bi (Strong SOI metals)	Al, Cu, Ag (High conductivity metals)	Al / Si, Cu / Cu-O (Large conductivity gradient)

Figure 1. Comparison between conventional and gyromagnetic charge-to-spin conversions from the view points of scattering source of electron spin, temporal and spatial feature, and typical materials appropriate for each method.

uniformity to generate spin currents. [Section 3](#) introduces studies demonstrating spin current generation comparable to that of rare metals through atomic rotations embedded in GHz-range surface acoustic waves (SAWs). [Section 4](#) discusses the rotational motion of conduction electrons in metallic thin films with nanoscale gradient modulation of electrical conductivity. [Section 5](#) provides unified discussions on the gyromagnetic effect. [Section 6](#) summarizes the findings of this review paper.

## 2. Background

### 2.1. History of theoretical research on gyromagnetic effect

After Oersted discovered that both permanent magnets and electric currents generate magnetic fields, Ampere and Lorentz hypothesized that the origin of magnetism in permanent magnets was due to molecular currents, i.e. currents circulating around molecules without resistance. The molecular current hypothesis was theoretically interpreted as the orbital motion of electrons, i.e. the Bohr model, through the development of quantum mechanics. Based on the hypothesis of molecular currents, Richardson predicted that the ratio of magnetization to angular momentum per unit volume would be  $e/2m$ , independent of materials, and proposed an experiment to verify this prediction [21].

According to the Richardson prediction, Einstein and de Haas succeeded to demonstrate the Richardsons experiment [22,23]. They suspended a cylindrical soft iron in an alternating magnetic field and detected resonantly the effect of magnetization on mechanical angular momentum by matching the frequency of alternating magnetic field with the natural frequency of its torsional oscillation. They found that the ratio of magnetization to angular momentum per unit volume was  $e/2m$ , as predicted. However, it has been recognized that the uncertainty assessment in the Einstein-de Haas experiment is insufficient, because the origin of soft iron's magnetism is spin angular momentum, whose gyromagnetic ratio differs by a factor of two compared to that in orbital angular momentum.

As an alternative experiment inspired by Richardson's prediction, Barnett successfully demonstrated its inverted effect [24,25]. Barnett measured the change in magnetization of a cylindrical iron rotated in a magnetic field using a fluxmeter and examined the rotational frequency dependence. He found that the ratio of magnetization to angular momentum per unit volume matched the expected value for soft iron, i.e.  $e/m$ . These experiments not only provided significant insights into the origin of magnetism in materials but also were epoch-making for demonstrating that the angular momenta in

magnetization and macroscopic rotational motions are compatible. However, despite the discovery of the gyromagnetic effect, research into its microscopic mechanisms has scarcely advanced until Mashhoon's theoretical work in 1988 [26].

Mashhoon extended the hypothesis of locality to investigate the coupling of rotation in non-inertial frames with neutron spins, deriving a spin-rotation coupling term in addition to the Sagnac term associated with the coupling of rotation and neutron orbital angular momentum [26]. This finding ensures the coupling between macroscopic rotational motion and the spin angular momentum of elementary particles in any materials. Namely, the gyromagnetic effect is a universal phenomenon not limited to ferromagnetic materials as originally examined, suggesting the broader applicability of the effect. Subsequently, Hehl and Ni investigated inertial effects on Dirac particles within the framework of special relativity, deriving a similar interaction between rotation and spin [27]. Based on these theories, Wallis et al. experimentally observed the Einstein-de Haas effect, a mechanical rotation effect in nanostructured magnetic materials, using a microcantilever [28]. Furthermore, Zolfagharkhani et al. detected mechanical torque due to spin flips when electrons pass through a junction of magnetic and non-magnetic metal nanowires using a torsional resonator [29].

### 2.2. Application of gyromagnetic effect to spintronics

Matsuo et al. explored the influence of mechanical rotation on spin currents (the flow of spin angular momentum), deriving a fundamental Hamiltonian that couples spin currents with mechanical rotation from the generally covariant Dirac equation. They found that the magnitude of the spin current is proportional to the frequency of mechanical rotation and the strength of the spin-orbit interaction in a rigidly rotating material [30–33]. This theory is extended from global rotation to local rotation characterized by vorticity, enabling a spin current generation that does not rely on strong spin-orbit couplings with the help of the gyromagnetic effect [18,20].

One of the promising methods is hydrodynamic spin current generation [34]. Indeed, hydrodynamic generation of spin current was successfully demonstrated from conducting liquid-metal flow in a narrow channel [35–38]. They measured the inverse spin Hall voltage produced by the spin current in a liquid-metal flow, where laminar and/or turbulent flow made vortical motion of liquid-metal atoms. An increase in the inverse spin Hall voltage with increasing the velocity of liquid-metal flow was clearly observed, supporting the gyromagnetic effect.

The gyromagnetic effect has been demonstrated not only in solid-state physics but also in high-energy

physics. The STAR Collaboration conducted non-central and ultra-relativistic collisions between gold nuclei, which create a high-temperature, low-viscosity fluid with energy densities that result in strong vortical structures [39]. These non-central collisions generate significant angular momenta, and strong vorticity may produce novel effects due to restored quantum chromodynamics symmetries. In gold nucleus collisions producing  $\Gamma$  baryons, they observed that the resulting quark-gluon plasma fluid is the most vortical system recorded, with  $\Gamma$  and hyperons displaying a few percent positive polarization.

Another proposal is acoustic spin current generation, where a rotational motion of atomic lattice points that is associated with propagating SAWs [20]. Experimental demonstration of such an acoustic spin current generation was reported by Kobayashi et al., who observed spin wave excitation in NiFe/Cu bilayers by propagating a SAW. The SAW produced an AC spin current in the Cu layer via gyromagnetic effect [18]. Kurimune et al. compared the magnitude of spin wave excitation among nonmagnetic metals with different electric conductivities. Similar to the theoretical speculation by Matsuo et al. [20], it was confirmed that nonmagnetic metals with higher electrical conductivity lead to stronger spin wave excitation [19].

### 3. Acoustic gyromagnetic effect

#### 3.1. General principles of surface acoustic waves

Elastic waves, i.e. plain waves of local strains propagating in elastic materials, have been widely used to study the gyromagnetic effects, which is associated with rotational motion of atoms. The frequencies of the elastic waves used to demonstrate the gyromagnetic effect are typically on the order of GHz, which is significantly lower than the electron relaxation frequency (e.g. approximately 50 THz at room temperature for copper). The amplitude and phase changes in these elastic waves are, therefore, described as classical sound waves rather than as quantum phonons. Consequently, in the gyromagnetic effect of elastic waves, the electron spins couples with a macroscopic angular momentum in the strain-induced vorticity of the lattice point velocity.

For elastic waves propagating through a metal with wavelengths much longer than the mean free path of the conduction electrons, the attenuation coefficient of the elastic wave is proportional to both the electrical conductivity and the square of the angular frequency [40]. Any SAW modes that include vertically or horizontally polarized shear wave, e.g. Rayleigh waves and Leaky SAWs, carry local angular momentum (i.e. non-zero vorticity) near the material surface and generate

the acoustic gyromagnetic effect. In such SAWs, the oscillatory motion of the lattice points is confined to a thickness with wavelength of the SAW on the surface.

For a Rayleigh wave propagating in the  $x$ -direction along the  $x$ - $y$  plane at  $z = 0$ , the time evolution of the lattice point displacements ( $u_x$ ,  $u_y$ ,  $u_z$ ) is given by the following equation [40]:

$$\mathbf{u} = \begin{pmatrix} u_x \\ u_y \\ u_z \end{pmatrix} = \begin{pmatrix} \left( e^{-k_l y} - \frac{2k_l k_t}{k_t^2 + k^2} e^{-k_t y} \right) i \Phi_0 e^{i(kx - \omega t)} \\ 0 \\ \left( -e^{-k_l y} + \frac{2k^2}{k_t^2 + k^2} e^{-k_t y} \right) \frac{k_l}{k} \Phi_0 e^{i(kx - \omega t)} \end{pmatrix} \quad (1)$$

Here,  $k$  and  $\omega$  are the wave number and angular frequency of the Rayleigh wave.  $k_l$  and  $k_t$  are given by  $\sqrt{k^2 - \omega^2/c_l^2}$  and  $\sqrt{k^2 - \omega^2/c_t^2}$ , where  $c_l$  and  $c_t$  are longitudinal and transverse wave velocities, respectively.  $\Phi_0$  is the scalar potential [41]. The trajectory of the lattice points is elliptical within the  $z$ - $x$  plane. According to the theory by Matsuo et al. [20], an effective magnetic field (Barnett field) along the  $y$ -axis on the electron spins is given by the half of the rotation of the velocity field of lattice displacements as shown in the following equation:

$$\Omega = \frac{1}{2} \nabla \times \partial_t \mathbf{u} = \begin{pmatrix} 0 \\ \Omega_y \\ 0 \end{pmatrix} = \begin{pmatrix} 0 \\ \frac{\omega^2 u_0}{c_t} e^{-k_t z} e^{i(kx - \omega t)} \\ 0 \end{pmatrix} \quad (2)$$

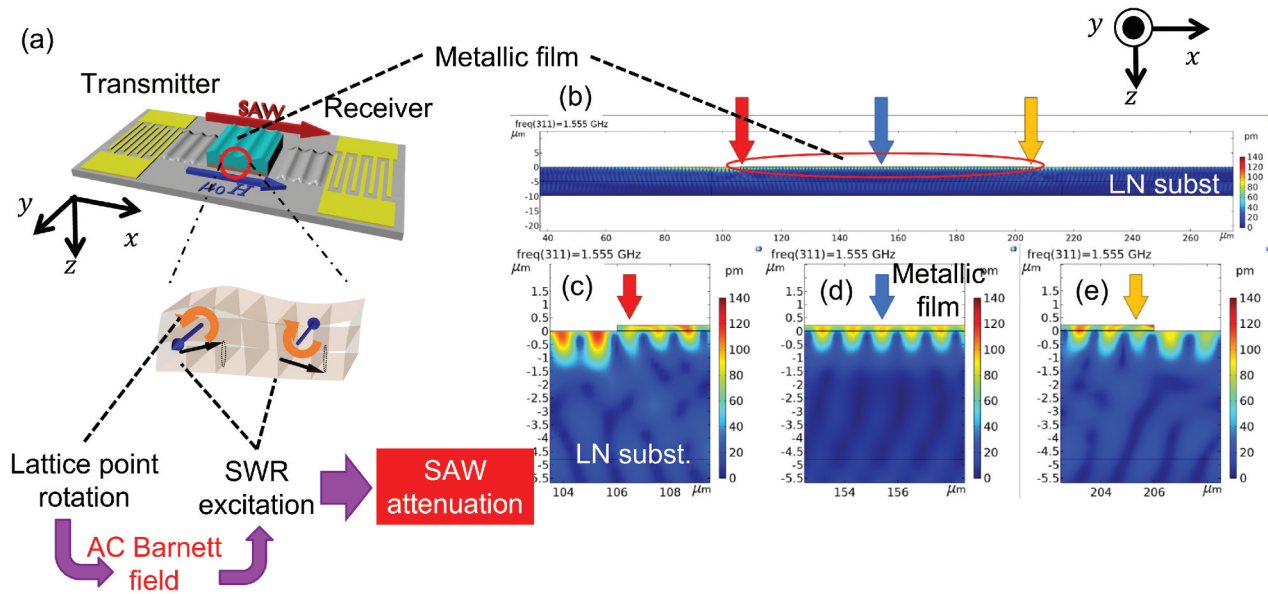
$$u_0 = |v(z=0)| = \frac{-k_t^2 + k^2}{k_t^2 + k^2} \frac{k_l}{k} \Phi_0. \quad (3)$$

#### 3.2. Generation and detection of surface acoustic waves

SAWs, characterized by high Q-factors and GHz-range carrier frequencies, propagate at speeds over three orders of magnitude slower than electromagnetic waves. These properties make SAWs highly suitable for use in microwave filter circuits and delay lines. As illustrated in Figure 2, to generate SAWs, a pair of interdigital transducers (IDTs) are generally fabricated on single crystalline ferroelectric substrates, e.g. LiNbO<sub>3</sub> and LiTaO<sub>3</sub>, known for their strong piezoelectric effects [42]. Each IDT can also detect SAWs by matching the structural period of the IDT with the SAW wavelength.

Applying an AC voltage to one of the IDTs creates a spatially modulated electric field in the substrate, which leads to a periodic electric polarization. The polarization induced via the inverse piezoelectric effect generates periodic lattice strains, which propagate in the form of SAWs along the substrate surface.





**Figure 2.** (a) Schematic configuration of SAW device and principle of spin wave resonance (SWR) excitation via SAW propagation. (b) Amplitude distribution of SAW propagating in a metallic thin film on LiNbO<sub>3</sub> (LN) substrate calculated using finite element method (FEM). The metallic film is composed of NiFe(20 nm) / Cu (200 nm) bilayer. Structural period of interdigital transducer is 2.4 μm, which determines the wavelength of SAW. (c–e) Magnified images at the regions indicated by red, blue, and yellow arrows in (b). (b)–(e) are reproduced by permission from [42], copyright [2023, The Japan Society of Applied Physics].

These SAWs can be electrically detected by another IDT through the inversion process. From the measurement of the  $S$ -parameter between transmitter and receiver IDTs using a vector network analyzer, one can evaluate the gyromagnetic effect, which occurs between the IDTs, as amplitude losses and phase shifts in the SAWs. Recently, Chen et al. proposed a method for detecting SAW attenuation in ferromagnetic thin films, demonstrating that SAW attenuation caused by acoustic ferromagnetic resonance excitation can be measured through anisotropic magnetoresistance-rectified direct-current voltages in ferromagnetic probe stripes embedded within SAW delay lines [43].

The piezoelectric properties of single crystalline LiNbO<sub>3</sub> and LiTaO<sub>3</sub> substrates strongly depend on those crystal orientation. These crystals have a trigonal structure with spontaneous polarization along the  $Z$ -axis. For instance, a 128°  $Y$ - $X$  LiNbO<sub>3</sub> substrate is obtained by cutting the single crystal such that its surface is rotated 128° with respect to the  $X$ -axis from the  $Y$ -plane (i.e.  $Y = 0$ ), allowing Rayleigh waves to be excited without spurious bulk or shear-horizontal (SH) waves. While it is true that LiNbO<sub>3</sub> substrates possess a higher electromechanical coupling coefficient (EMCC) for SH waves compared to LiTaO<sub>3</sub>, the 36°  $Y$ - $X$  LiTaO<sub>3</sub> substrate exhibits an SH wave EMCC that is more than ten times greater than that for Rayleigh waves on the same substrate. This characteristic makes LiTaO<sub>3</sub> particularly advantageous for devices designed to selectively exploit SH waves. Additionally, piezoelectric semiconductors, such as ZnO, GaAs, and AlN, can also excite SAWs. Sogawa et al. have demonstrated

band structure modulation by propagating SAWs through GaAs/AlAs quantum well structures [44–48]. High-frequency SAWs exceeding 10 GHz has been achieved in piezoelectric thin films fabricated on substrates with high sound velocities, which is proportional to the square root of Young's modulus/density, such as low-density single-crystal diamond [49,50].

To investigate gyromagnetic and magnetoelastic effects of SAWs in the absence of piezoelectric effects or with metallic films that shield the IDT electric field, a desired metallic thin film is fabricated on ferroelectric substrates capable of SAW excitation, and SAWs are injected externally as discussed in Sec. 3.3, 3.4 and 3.5. Figure 2(b–e) shows the numerical results of the amplitude distribution calculated using the finite element method (FEM) [42]. Here, a pair of Au (80 nm) IDTs with 0.6 μm width and spacing were formed on a 128°  $Y$ - $X$  LiNbO<sub>3</sub> substrate, with a 100 μm-wide NiFe (20 nm)/Cu (200 nm) metallic bilayer between them. The color intensity in Figure 2(b–e) represents the lattice point displacement under an applied AC voltage of 0.18 V (0.32 mW) at 1.555 GHz. The figure illustrates that SAWs generated by the IDTs successfully penetrate the metallic thin film, with the displacement amplitude decaying in the depth direction from the metallic film surface.

### 3.3. Quantitative evaluation of surface acoustic waves using magnetoelastic effects

To understand the physics of gyromagnetic effects caused by lattice strain in SAWs, it is essential to

establish quantitative methods. This subsection focuses on the magnetoelastic effect, which is more pronounced and better understood than gyromagnetic effects.

### 3.3.1. Optical imaging and quantification of SAW amplitude [51]

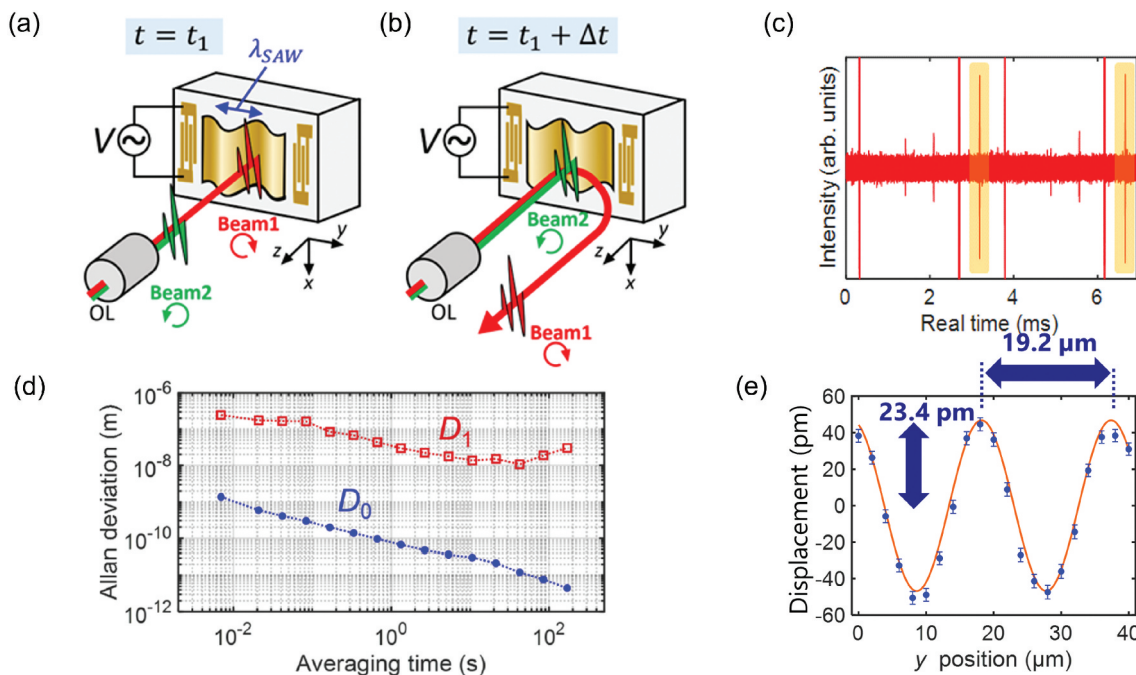
To accurately evaluate the absolute amplitude of SAWs propagating through a metallic thin film, a temporal-offset dual-comb vibrometer has been developed, as shown in Figure 3(a,b). This technique involves splitting an optical pulse into two pulses with a time offset, adjusted so that the two pulses reflect at the crests and troughs of the SAW oscillations. By performing dual-comb interferometry on the two pulses, which reflect at different displacement positions along the  $z$ -direction (i.e. vibration direction), using another femtosecond laser, we can measure the phase difference and estimate the absolute SAW amplitude.

Figure 3(c) shows the interference signal between one of the split optical pulses and another femtosecond laser. The interference signal displays multiple peaks, where the peak highlighted by yellow corresponds to the reflection from the SAW. The other peaks are due to stray light reflections from other optical components. Conventional optical interferometry suffers from mixed signals that compromise measurement accuracy, but the temporal-offset dual-comb vibrometer separates these stray light signals in

the time domain, allowing for ‘clean’ vibration measurements based solely on the SAW reflection.

Figure 3(d) shows the data-averaging time dependence of the Allan deviation of twice the measured vibration amplitude. The blue data points ( $D_0$ ) represent results from the time-offset dual-comb measurement, while the red points ( $D_1$ ) are based on traditional methods using one of the split pulses for distance measurement. Although the accuracy of both datasets improves with increased data-averaging time, the time-offset dual-comb method achieves  $10^{-2}$  to  $10^{-3}$  times better accuracy than conventional methods. Furthermore, while the accuracy of traditional methods plateaus after a certain averaging time, the time-offset dual-comb method continues to show improvement. Such a superior accuracy is attributed to the minimized phase uncertainty by comparing the phase difference between two pulses traveling along the same optical path.

Figure 3(e) illustrates the measured  $y$ -axis distribution of surface displacement of the SAW. A pair of IDT electrodes was fabricated on a LiNbO<sub>3</sub> substrate, with a Ti(3 nm)/Au(70 nm) bilayer film deposited between the electrodes. A radio-frequency signal generator applied a sinusoidal signal with a frequency of 180 MHz and an amplitude of 0.50 V to the IDT electrodes, injecting SAWs into the bilayer. The observed phase difference between the split pulses, corresponding to their  $z$ -position difference, oscillated sinusoidally with an amplitude of 23.4 pm. The period revealed that the SAW propagated through the bilayer with



**Figure 3.** (a, b) Schematic principle of time-offset dual-comb interferometric distance measurement. (c) Raw interferogram data measured during a single measurement interval, (d) averaging-time dependence of the Allan deviation of twice the measured vibration amplitude measured using conventional ( $D_1$ ) and developed ( $D_0$ ) methods, and (e) measured surface displacement distribution of SAW. Reproduced from [51].

a wavelength of 19.2  $\mu\text{m}$ , which is matched to the wavelength estimated from the applied frequency and SAW velocity. Namely, the signal amplitude in Figure 3(e) reflects the SAW vibration amplitude. By achieving clean interferometric measurements with minimal stray light interference, we can determine the absolute SAW vibration amplitude with a precision of 4 picometers.

### 3.3.2. Quantitative analysis of depth profile of strains in SAWs [52]

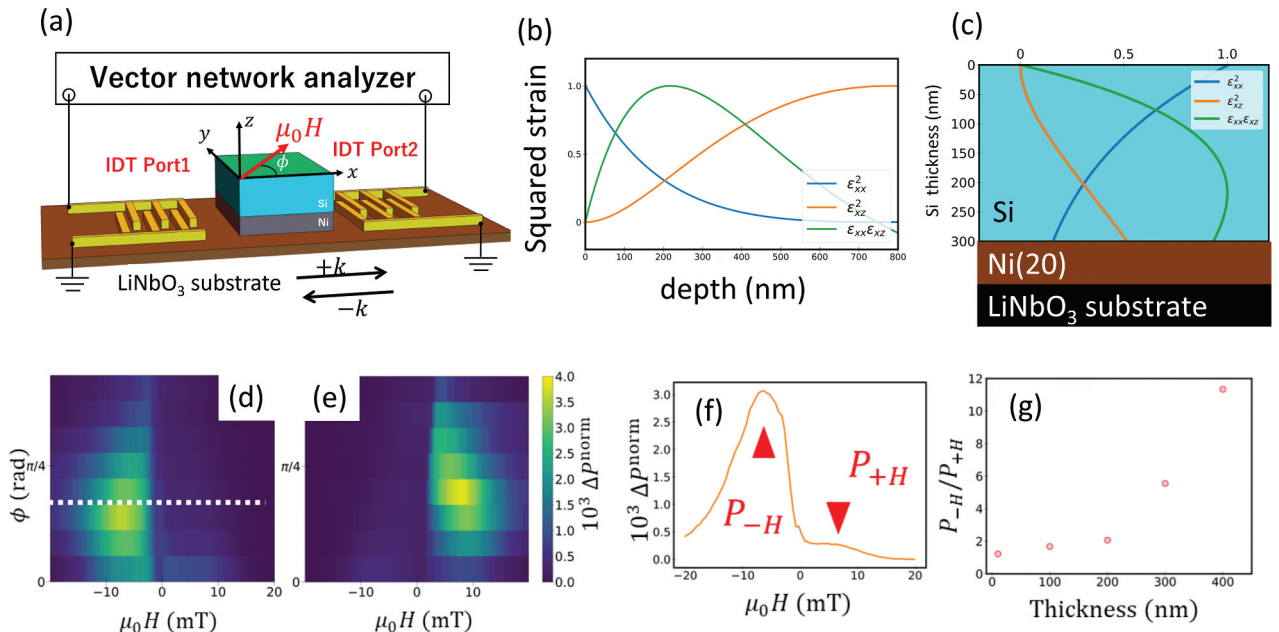
Understanding not only the absolute amplitude but also the depth profile of strains in Rayleigh waves are essential for quantitative analysis of their gyromagnetic effects. Here, we review recent research on the evaluation of depth profile of SAWs strains from the observation of an asymmetric SAW propagation in ferromagnetic Ni/semiconductor Si bilayer due to the magnetoelastic effect.

As shown in Figure 4 (a), a composite material was fabricated by depositing a 20-nm thick ferromagnetic Ni film on a 128° Y-X LiNbO<sub>3</sub> substrate with IDTs for SAW generation and detection, followed by the deposition of semiconductor Si thin film with a given thickness. When SAWs are injected into the composite material, the Ni lattice vibrates rapidly, generating spin waves via the magnetoelastic effect [53–62]. SAWs produce orthogonal effective fields owing to a longitudinal strain component  $\epsilon_{xx}$ , which does not change sign with propagation direction, and a shear

strain component  $\epsilon_{xz}$ , which changes the sign [55]. These strains also cause acoustic gyromagnetic effects. Capturing the depth distribution of these strain components is, therefore, key to quantifying gyromagnetic effects and understanding the mechanism of spin current generation due to non-uniform spin-dependent scattering effects.

Earlier work by Sasaki et al. has shown that the shear strain component produces non-reciprocal propagation in spin waves [59]. This study focuses on the ratio of shear to longitudinal strain, which increases as the ferromagnetic layer is embedded deeper from the surface (see Figure 4 (b, c)). By measuring how the non-reciprocity of spin wave propagation changes with the embedding depth of the ferromagnetic Ni film, the depth distribution of the strain ratio  $\epsilon_{xz}/\epsilon_{xx}$  can be determined. The change in spin wave amplitude excited in the Ni thin film by SAW injection was evaluated using S-parameter measurements with a vector network analyzer.

Here, spin waves are excited magnetoelastically using a SAW with a frequency of 1.85 GHz. As spin waves propagate through the Ni/Si composite, the amplitude of the SAW attenuates to compensate for magnetic dissipation. The attenuation of SAWs due to spin wave propagation was measured while sweeping an external magnetic field  $H$  rotated by  $\phi$  from the SAW propagation direction. Figures 4 (d) and 4 (e) are color plots of the SAW attenuation in the  $H$ - $\phi$  parameter plane for SAW propagation from IDT1 to IDT2



**Figure 4.** (a) Schematic setup for evaluating depth profile of strains in SAWs propagating in Si/NiFe bilayer deposited on LiNbO<sub>3</sub> substrate. (b) Numerical depth profile of squared strains,  $\epsilon_{xx}^2$ ,  $\epsilon_{zx}^2$  and  $\epsilon_{xx}\epsilon_{zx}$ , calculated for semi-infinite elastic plate. (c) Depth profile of squared strains in Si layer deposited on Ni(20) layer. Color plots of the SAW attenuation in the  $H$ - $\phi$  parameter plane for (d) SAW propagation from IDT1 to IDT2 and (e) the reverse direction (IDT2 to IDT1), respectively. (f) Cross-sectional view along the dotted line in (e). Si film thickness dependence of the magnitude of spin wave non-reciprocity, representing the ratio of forward to reverse spin wave intensities. Reproduced by permission from [52], copyright [2020, American Physical Society].



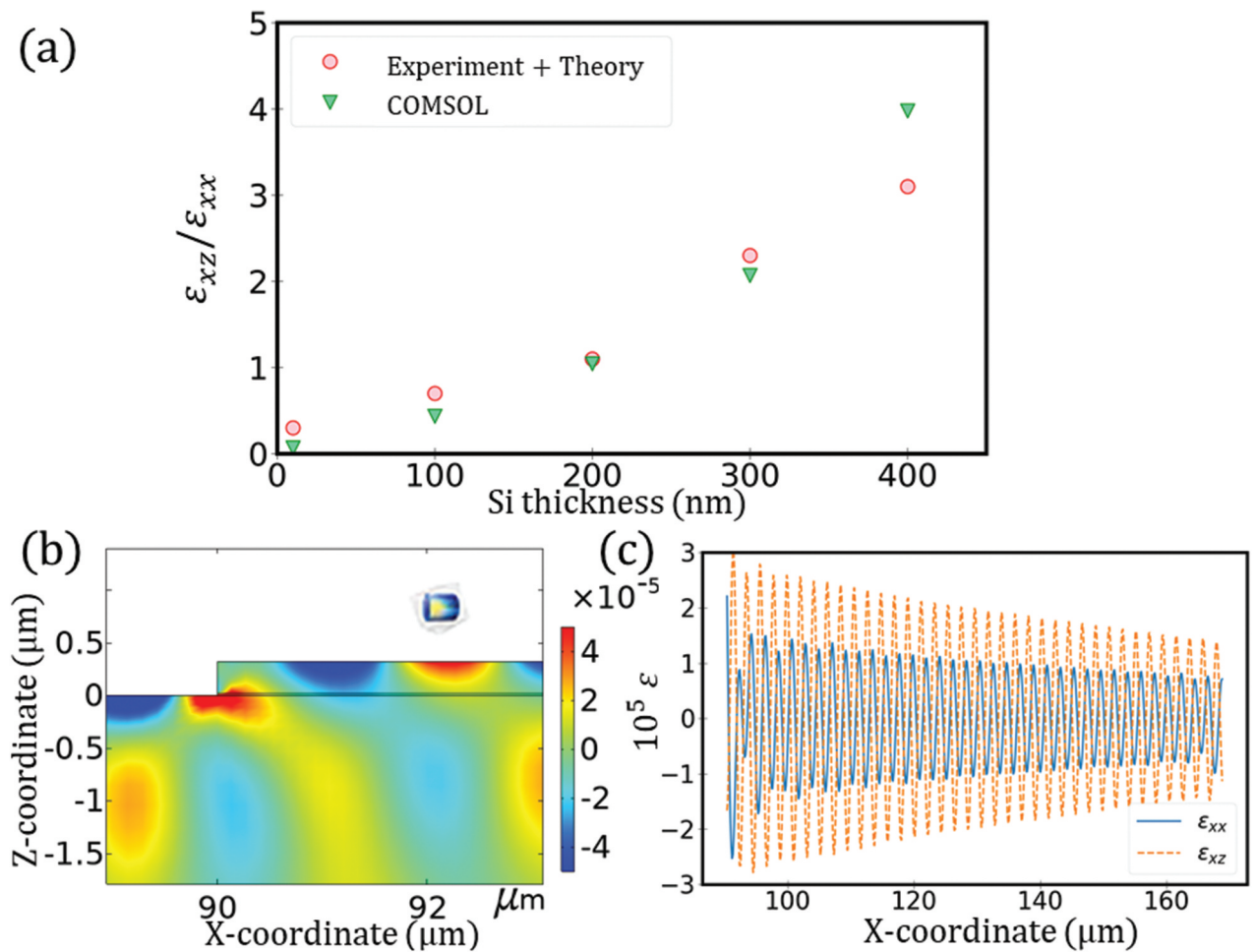
and the reverse direction (IDT2 to IDT1), respectively. Comparing Figures 4 (d) and 4 (e), the direction of non-reciprocity of spin wave intensity reverses with the SAW propagation direction, demonstrating unidirectionality in spin waves for a fixed external magnetic field direction. Similarly, the non-reciprocity of spin waves allows for modulation of the amplitude of SAWs propagating in a fixed direction by reversing the magnetic field [63]. As illustrated in Figure 4 (f), which shows a cross-sectional view along the dotted line in Figure 4 (d), there is a significant variation in the SAW attenuation intensity depending on the direction of the external magnetic field (i.e. the magnetization direction of the Ni film). The strong non-reciprocity observed in the Ni/Si composite material also suggests that the gyromagnetic effect, which occurs when a non-magnetoelastic material undergoes lattice rotation (see Section 3.4), can be neglected, as spin waves induced by the gyromagnetic effect do not demonstrate non-reciprocity [64].

Figure 4 (g) shows the Si film thickness dependence of the magnitude of spin wave non-reciprocity, representing the ratio of forward to reverse spin wave intensities  $P_{-H}/P_{+H}$ , where  $P_{+H}$  and  $P_{-H}$  are peak

amplitudes for positive and negative external fields, respectively, as indicated by triangles in Figure 4 (f). As the Si film thickness increases, embedding the Ni film deeper from the surface, the non-reciprocity increases, reaching up to 1200% for a 400 nm Si film. This level of non-reciprocity surpasses previously reported values for spin waves.

Figures 5 (a)–(c) show the Si film thickness dependence of the  $\epsilon_{xz}/\epsilon_{xx}$  ratio estimated from the magnitude of spin wave non-reciprocity, the cross-sectional distribution of strain intensity calculated by the two-dimensional finite element method (FEM) implemented in the frequency domain by COMSOL MULTIPHYSICS, and the attenuation of  $\epsilon_{xx}$  and  $\epsilon_{xz}$  in the SAW propagation direction, respectively. Figure 5 (a) provides the depth distribution of vorticity of lattice displacement velocity in SAWs. Comparing these results with the gyromagnetic effects of SAWs, therefore, advances the quantitative understanding of spin current generation mechanisms due to non-uniform spin-dependent scattering effects.

This study has also significant implications for engineering applications, because the non-reciprocity of spin waves can be dramatically increased only by



**Figure 5.** (a) Si film thickness dependence of the  $\epsilon_{xz}/\epsilon_{xx}$  ratio estimated from the magnitude of spin wave non-reciprocity, (b) cross-sectional distribution of strain intensity calculated using finite element method (FEM), and (c) attenuation of  $\epsilon_{xx}$  and  $\epsilon_{xz}$  in the SAW propagation direction. Preprinted with permission from [52], copyright [2020, American Physical Society].



fabricating a semiconductor Si on the surface of a magnetic material. This method is not limited to specific semiconductor or magnetic materials but can create devices with deeply formed magnetic thin films, resulting in large spin wave non-reciprocity. This paves the way for the realization of spin wave diodes [65], essential for functional operations of spin wave devices such as switching and logic calculations.

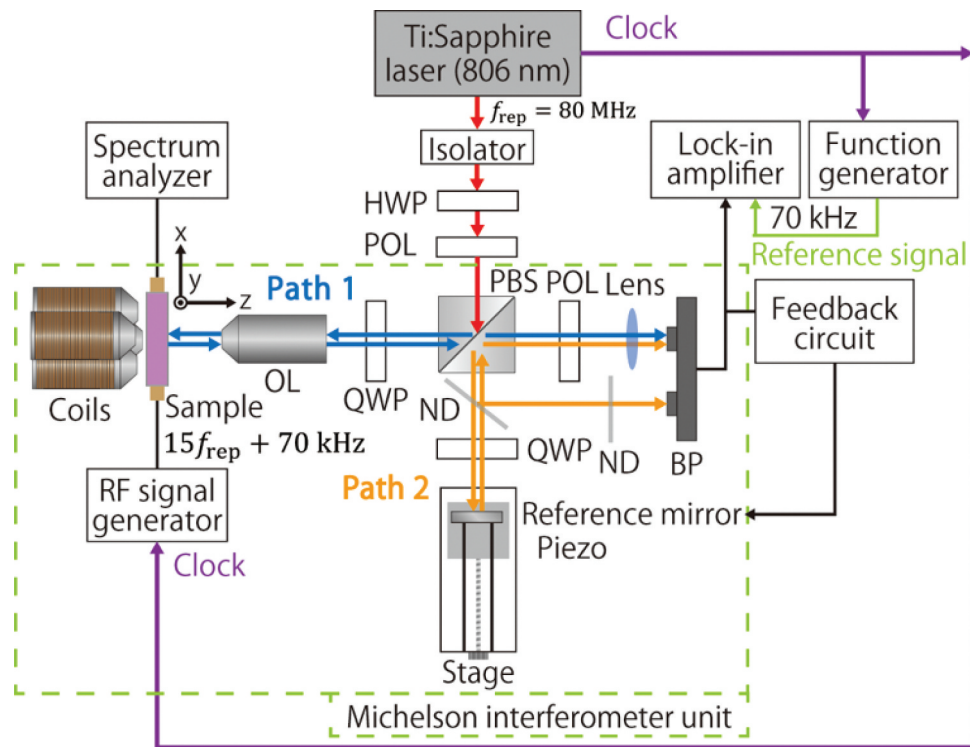
### 3.3.3. Amplitude and phase changes of SAW due to magnetoelastic coupling with spin waves [66,67]

While the method described in Section 3.3.1 provides extremely high precision in quantifying SAWs amplitude, it is time-consuming and impractical for actual device evaluation. To address this issue, another stroboscopic optical interferometric measurement technique has been developed, which successfully visualizes the changes in amplitude and phase of SAWs propagating in Ni thin films due to magnetoelastic effects.

Figure 6 shows the experimental setup for the stroboscopic optical interferometric measurement, which provides a modified method from the original work by Shao et al. [68]. The laser light output from an ultrashort titanium-sapphire laser pulse is split into Path1 and Path2 by reflecting or transmitting through a polarization beam splitter (PBS). The laser light in Path1 and Path2 reflects at the Ni thin film and a reference mirror, respectively, and recombines at the PBS. The combined beams are passed through

a polarizer (POL) to match their polarization states, and the interference signal is detected by a balanced photodetector. Because an ultrashort laser pulse with a short coherence length is used, the detector observes a significant interference signal only when the optical path lengths of Path1 and Path2 are identical. By using a feedback loop to control the position of the reference mirror to fix the interference signal at a specific voltage value, the ultra-small vibrations of the Ni thin film can be measured. Additionally, the SAW excitation frequency is set to 15 times the repetition frequency of the ultrashort pulse laser plus with an offset of 70 kHz, capturing the dynamic vibration amplitude of the SAW in a stroboscopic manner.

The ferromagnetic resonance absorption was electrically measured while simultaneously measuring the SAW vibration using the stroboscopic optical interferometry technique. The SAW excited by the IDT electrodes propagates across the Ni thin film. When the SAW excitation frequency with 1.2 GHz matched the precession frequency of the magnetization in the Ni thin film (i.e. resonance condition), the SAW amplitude decreased as it passed through the thin film due to the mechanical rotation-spin conversion via the magnetostrictive effect. This result is consistent with previous electrical measurements reported by Weiler et al. [53]. By measuring the SAW transmittance electrically while varying the applied magnetic field, we observed a clear ferromagnetic resonance



**Figure 6.** Experimental setup for the stroboscopic optical interferometric measurement. The laser light output from an ultrashort pulse titanium-sapphire laser is split into Path1 and Path2 by reflecting or transmitting through a polarization beam splitter (PBS). The laser light in Path1 and Path2 reflects at the sample (Ni thin film) and a reference mirror, respectively, and recombines at the PBS. The combined beams are passed through a polarizer (POL) to match their polarization states, and the interference signal is detected by a balanced photodetector (BP). Preprinted with permission from [67], copyright [2024, American Physical Society].

absorption peak as shown in Figure 7 (a). Furthermore, using the stroboscopic optical interferometry both under resonance and non-resonance conditions, we clearly observed a decrease in SAW amplitude and a change in SAW phase under resonance conditions through spatially resolved imaging as shown in Figure 7 (b). It is noted that there have been several reports on spatially resolved imaging of conversion between mechanical rotation and spin using photoemission electron microscopy and X-ray magnetic circular dichroism imaging [69], as well as Brillouin light scattering experiments [70]. However, the measurement speed of these methods is slow, and there are no reports on the quantitative evaluation of the amplitude and phase profiles of a SAW coupled to magnons across the entire length of a device. Therefore, the results in Figure 7 represent the first spatially resolved imaging experiment that quantitatively captures the complete profile changes (i.e. amplitude and phase) of SAW vibrations due to mechanical rotation-spin conversion across the entire length of the device.

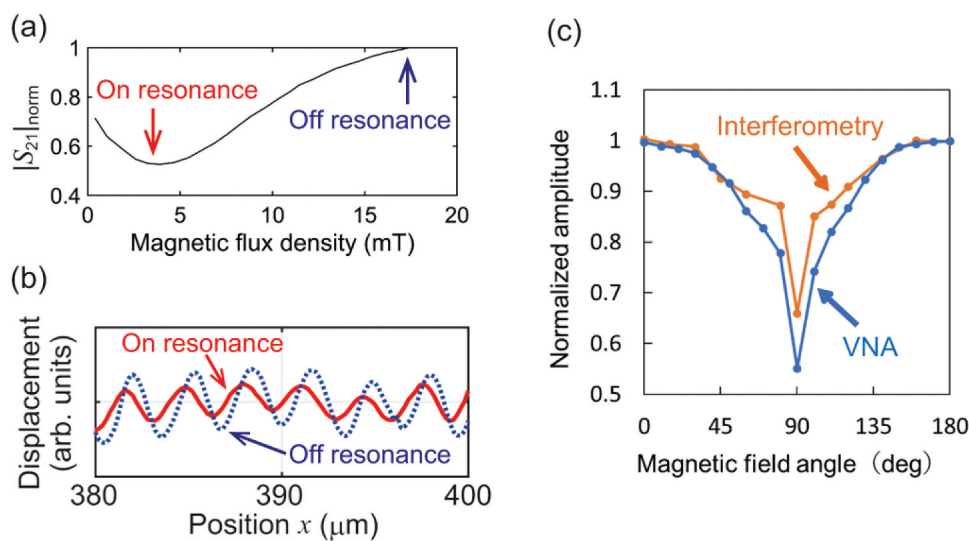
Here, we conducted a quantitative comparison of the SAW attenuation measured by the conventional vector network analyzer method and the stroboscopic optical interferometry. To identify the observation conditions, we extracted the SAW attenuation at the end of the propagation path in the Ni film for the stroboscopic optical interferometry. Figure 7 (c) compares the change in the SAW attenuation when the external field is rotated, while the field strength is fixed at 4.94 mT, which is close to the resonance condition in Figure 7 (a). Similar angular dependence is observed, although

there is some quantitative inconsistency, with the stroboscopic optical interferometry results showing smaller amplitude changes. Possible reasons for these differences include the effects of SAW reflection by the IDT electrodes and polarization rotation specific to optical interferometry.

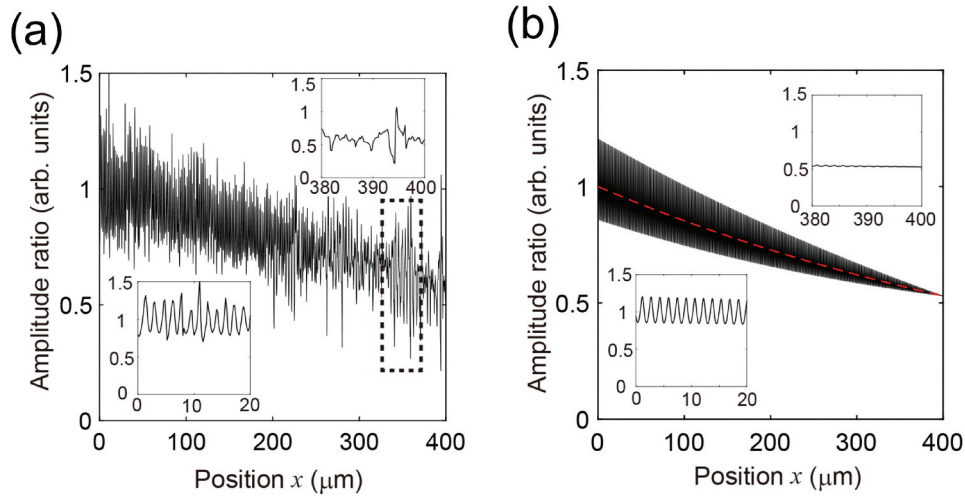
### 3.3.4. Imaging of interference effects of magnetoelastic waves [67]

In devices using IDT electrodes for the generation and detection of SAWs, the detected SAWs undergo the Bragg reflection by detecting IDT electrode, interfering with the primary SAWs. Here, we discuss the interference effects of SAWs coupled with spin waves in detail using the stroboscopic optical interferometry method described in Sec. 3.3.1.

Figure 8(a) shows the spatial distribution of the ratio of surface displacement amplitudes of SAWs propagating through the Ni thin film measured under ferromagnetic resonance and non-resonance conditions. The resonance condition of the Ni thin film could be tuned by adjusting the resonance frequency with an external magnetic field to either match (i.e. resonance) or not match (i.e. non-resonance) the SAW frequency. Under resonance conditions, the amplitude of the SAW decreased with the propagation due to magnon-phonon coupling. However, the SAW attenuation was not uniform; it oscillated while decaying. To explore the origin of the oscillation, we considered the effect of reflected SAWs from the detection of IDT electrodes on the experimentally observed spatial profile of the



**Figure 7.** (a) Electrically measured SAW transmittance as a function of external magnetic flux density. Ferromagnetic resonance absorption peak clearly appears. (b) Spatially resolved imaging of SAWs observed at on resonance and off resonance conditions for the spin wave excitation. (c) Comparison of the change in the SAW attenuation when the external field is rotated while the field strength is fixed at 4.94 mT, which is close to the resonance condition in (a). Blue and orange closed circles represents the data measured by a vector network analyzer and stroboscopic optical interferometry, respectively. Preprinted with permission from [67], copyright [2024, American Physical Society], and from [66], copyright [2023, IEEE].



**Figure 8.** Spatial distribution of the ratio of surface displacement amplitudes of SAWs propagating through the Ni thin film measured under ferromagnetic resonance and non-resonance conditions. (a) Experimental and (b) numerical results. Preprinted with permission from [67], copyright [2024, American Physical Society].

amplitude ratio in Figure 8(a), in addition to the propagation of the primary SAWs. Figure 8(b) shows the results of numerical simulation. The comparison revealed that the interference between primary SAWs coupled to magnons, or magnetoelastic waves, and the secondary magnetoelastic waves reflected by the IDT electrode resulted in part of the surface vibration becoming a standing wave, thereby causing a spatial amplitude oscillation. Additionally, we assumed the reflection coefficient for the IDT electrodes to be the same as that evaluated from the S-parameter measurement in our numerical simulation. The good agreement between experimental results and simulation validates the accuracy of our analysis.

The SAWs propagating through the Ni thin film can also be regarded as magnetoelastic waves with magnon-phonon coupling. Figure 8 demonstrates that the propagation distance of magnetoelastic waves is several millimeters, which is extremely long, indicating that interference effects within the sample cannot be ignored. Generally, the propagation distance of magnons in metallic magnetic materials, such as Ni, is very short, on the order of several micrometers, but the propagation distance of magnetoelastic waves coupled with SAWs is over several millimeters, significantly impacting device operation. This result is considered beneficial for the future realization of long-distance transmission in magnetic devices.

### 3.4. Spin wave excitation by gyromagnetic effects of surface acoustic waves

#### 3.4.1. Spin wave excitation in non-magnetoelastic NiFe thin films by SAWs [64]

Similar to the experimental setup for the magnetoelastic spin wave excitation using SAWs, ferromagnetic

NiFe thin films, whose magnetoelastic effect is negligible, are deposited between IDT electrode pairs that generate and detect SAWs, and Rayleigh-type SAWs are injected. In the case of non-magnetoelastic NiFe film, due to the relativistic gyromagnetic effect (i.e. Barnett effect) caused by lattice rotation, the magnetic torque is exerted on the magnetization of NiFe, and spin waves with wavelengths and frequencies equal to those of the SAW are resonantly excited. Since the Barnett effect is proportional to the vorticity of the lattice motion of the SAW, the displacement of lattice rotation in the SAW can be determined by the intensity of excited spin waves. However, since the magnetoelastic effect of ferromagnetic thin films can also excite spin waves, it is important to evaluate spin waves originating from the Barnett effect for accurate quantification of SAWs. The Barnett effect and magnetoelastic effect could be separated and measured from the differences in the dependence on the magnetic field angle and frequency as follows:

The magnetization direction, where a maximum magnetic torque is obtained, depends on whether the Barnett effect or magnetoelastic effects from longitudinal and shear strains,  $\epsilon_{xx}$  and  $\epsilon_{xz}$ , are dominated. In the case of Rayleigh-type SAWs propagating in  $x - y$  plane along  $x$  axis, the lattice points displace in an ellipse in the  $z - x$  plane so that the vorticity vector of the velocity field of the lattice displacement points in the  $y$  axis. The vorticity temporally evolves along the  $x$  axis while changing its sign in a period with the wavelength of the SAW. Consequently, the Barnett field due to the lattice rotation points in the  $y$  axis so that the magnetic torque is maximized when the magnetization vector is perpendicular to the  $y$  axis. Contrary, the effective magnetic field of the magnetoelastic effect due to  $\epsilon_{xx}$  of the Rayleigh-type SAW is produced in the direction inclined by  $\pm\pi/4$  with

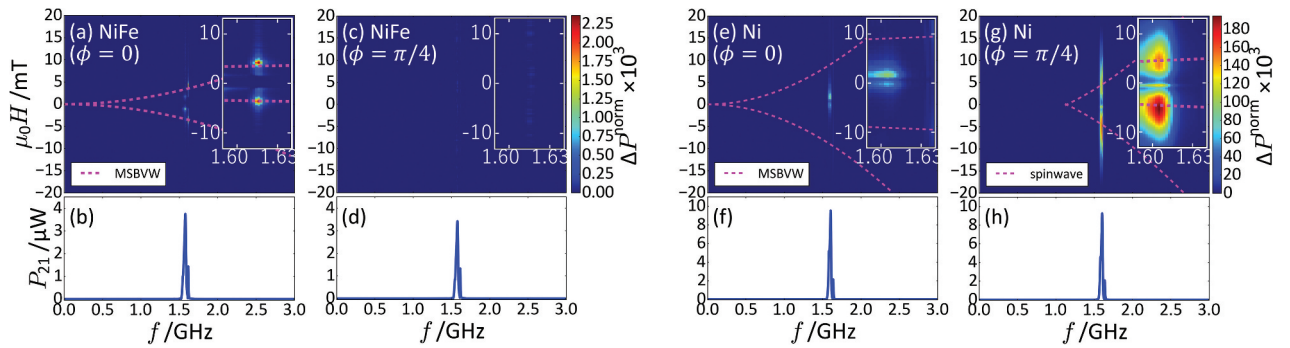
respect to the  $x$  axis in the  $x - y$  plane. Furthermore, the effective magnetic field of the magnetoelastic effect due to  $\epsilon_{xz}$  points in the  $z$  axis direction [55]. The magnetic torques due to these three magnetic fields have, therefore, different magnetization orientations that maximize them, allowing separation based on the magnetization orientation dependence of the spin wave intensity induced by the SAW.

$$\Delta P^{\text{norm}}(f, H) = \frac{|\mathbf{P}_{21}(f, H) - \mathbf{P}_{21}(f, H_{\text{ref}})|}{P_{21}(f_{\text{res}}, H_{\text{ref}})}, \quad (4)$$

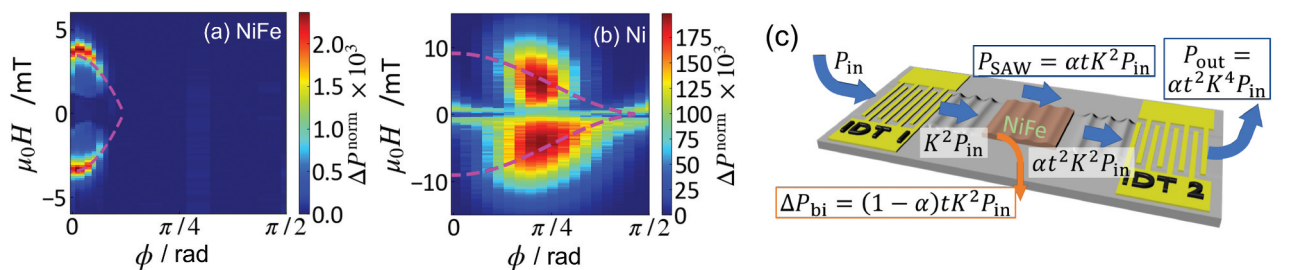
where  $\mathbf{P}_{21}(f, H)$  is the complex power of the transmitted microwave calculated from  $S_{21}$  at a given frequency  $f$  and external magnetic field with magnitude of  $H$ .  $\mu_0 H_{\text{ref}}$  is the reference magnetic field with  $-20$  mT, which is sufficient to saturate the magnetization. By subtracting  $\mathbf{P}_{21}(f, H_{\text{ref}})$  from  $\mathbf{P}_{21}(f, H)$ , the influence of field-independent signals can be ignored. As a control experiment, Figures 9 (e) and 9 (g) show color plots of  $\Delta P^{\text{norm}}$  measured for Ni thin films, which have a larger magnetoelastic effect than NiFe. The graphs below the color plots show the frequency variation of microwave transmission coefficient of the SAW devices used in each experiment. SAWs are injected into the ferromagnetic thin films at a peak frequency around 1.6 GHz. The dashed lines in the color plots indicate the conditions where spin waves

are resonantly excited in the ferromagnetic thin films. From Figure 9, it is found that the spin wave is intensely excited when the magnetization of NiFe thin films is oriented along the  $x$  axis, where the magnetic torque due to the Barnett field is maximized. In contrast, for Ni thin films, strong spin waves were observed when the magnetization was oriented in the direction where the magnetic torque due to the longitudinal strain component  $\epsilon_{xx}$  of the magnetoelastic effect is maximized. Figures 10(a,b) show detailed results of the magnetic field angle dependence of the SAW attenuation, clearly indicating that the spin wave excitation in NiFe thin films is predominantly due to the Barnett effect. Furthermore, as discussed in Sec. 3.6, the frequency dependence of the spin wave intensity varies depending on whether the spin wave is excited via the Barnett effect or magnetoelastic effect.

From the intensity of gyromagnetic spin wave resonance (SWR) excited in the NiFe film, we can evaluate the averaged amplitude of lattice oscillation in the Rayleigh-SAW. Figure 10(c) schematically shows the energy loss diagram in the SAW device. Here,  $P_{\text{in}}$  and  $P_{\text{out}}$  are the input and output microwave power, respectively.  $P_{\text{SAW}}$  is the microwave amplitude transmitted through the NiFe film, and  $\Delta P_{\text{bi}}$  is the microwave absorption owing to the SWR excitation.  $K^2$  is electromechanical coupling constant



**Figure 9.** Color plot of reduced SAW attenuation  $\Delta P^{\text{norm}}$  for (a,c) NiFe and (e,g) Ni films as a function of frequency and external magnetic field, which is applied at angles of (a,e) 0 and (c,g)  $\pi/4$  from the propagation direction of SAW. Graphs below the color plots (b,d,f,h) show the frequency variation of microwave transmission coefficient  $P_{21}$  of the SAW devices used in each experiment. Preprinted with permission from [64], copyright [2020, American Physical Society].



**Figure 10.** Color plot of reduced SAW attenuation  $\Delta P^{\text{norm}}$  for (a) NiFe and (b) Ni films as a function of angle for magnetic field application and external magnetic field. The frequency of the SAW was fixed at 1.6 GHz. (c) Schematically energy loss diagram in the SAW device. Preprinted with permission from [64], copyright [2020, American Physical Society].



for IDT,  $t$  is the SAW transmission ratio across the interface between NiFe film and LiNbO<sub>3</sub> substrate which is determined by the acoustic impedance mismatch, and  $\alpha$  is SAW transmission ratio in the NiFe film, which becomes less than unity when the spin wave is excited.  $\Delta P^{\text{norm}}$  is, therefore, given by  $\{P_{\text{out}}(\alpha) - P_{\text{out}}(\alpha = 0)\}/P_{\text{out}}(\alpha = 0) = 1 - \alpha$ , where the value of  $P_{\text{out}}(\alpha = 1)$ , can be evaluated from  $S_{21}$  at a non-resonant state. According to the energy diagram, we can derive an analytical relationship between  $\Delta P^{\text{norm}}$  and effective SAW amplitude  $u_0$  as follows:

$$\Delta P^{\text{norm}} = \frac{\omega \chi''_{yy} |h_B|^2 V_{\text{FM}}}{2P_{\text{SAW}}} \quad (5)$$

$$|h_B| = \frac{\omega^2 u_0}{2\gamma c_t}, \quad (6)$$

where  $\omega$  is the angular frequency of SAW and  $V_{\text{FM}}$  is the volume of ferromagnetic materials, where the SAW propagates.  $\chi_{yy}$  is  $(y,y)$  component of the Polder susceptibility tensor.  $|h_B|$  is the absolute amplitude of the Barnett field. Finally, the strength of the Barnett field is evaluated at 1.3  $\mu\text{T}$ , which corresponds to the lattice displacement of 6.8 picometer for  $-5$  dBm microwave input at 1.6 GHz. This displacement is smaller than the value obtained through optical measurements as discussed in Sec. 3.3.1. The electrically evaluated displacement represents an average over the depth, whereas the optical method measures the maximum surface displacement, explaining the discrepancy between the two methods.

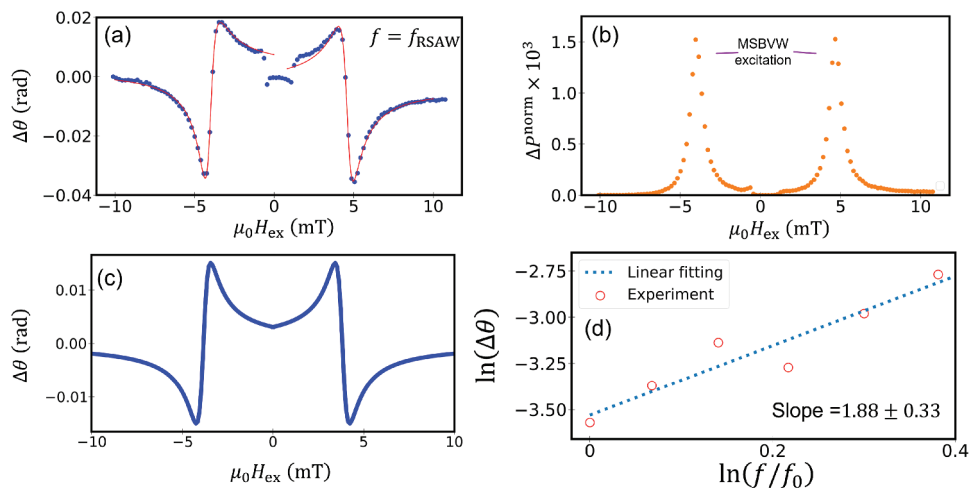
Magneto-optical techniques, such as MOKE, offer a promising approach for visualizing spin accumulation [71,72]. These techniques provide a potential direction for future experimental studies on the acoustic gyromagnetic effect.

### 3.4.2. Reciprocity in gyromagnetic effect of surface acoustic waves [73]

In Sec. 3.4.1, we review the gyromagnetic SWR excitation via the Barnett field. Such a gyromagnetic effect should be reciprocal, as seen in the original experiments by Barnett, Einstein, and de Haas. In the acoustic gyromagnetic effect, it is succeeded to observe acceleration and deceleration of SAW caused by the Einstein-de Haas (EdH) torque, which comes from the back action of the SWR excitation via Barnett field. Figure 11(a) shows the gyromagnetic phase shift of SAW, which is simultaneously observed with the gyromagnetic attenuation as shown in Figure 11(b). A bipolar change in the phase shift, representing acceleration and deceleration of the SAW, is observed at spin wave resonant fields. Here, we evaluate the bipolar phase shift by solving the following elastic equation for RSAW with the EdH torque.

$$\rho \partial_t^2 u_i = \partial_{x_j} \sigma_{ij}^E + \partial_{x_j} \sigma_{ij}^{\text{EdH}}, \quad (7)$$

where  $\rho$  is the mass density of elastic materials used for SAW waveguide,  $\sigma_{ij}^E$  and  $\sigma_{ij}^{\text{EdH}}$  are stresses owing to electromechanical and EdH torques, respectively. The first and second terms of the right side show forces associated with internal stress and additional stress owing to the EdH torque, which is produced by a back action of magnetic torque owing to the Barnett effect. The EdH torque contributes to the off-diagonal elements of an antisymmetric stress tensor. By solving the transverse and longitudinal components of the lattice displacement by applying a free boundary condition at the surface, the velocity modulation of SAW owing to the EdH torque is deduced as shown in the following equation:



**Figure 11.** (a) Gyromagnetic phase shift and (b) gyromagnetic attenuation of SAW measured for NiFe films as a function of external magnetic field. (c) Numerically evaluated EdH phase shift. (d) Double-logarithmic plot of the phase shift as a function of reduced frequency. Preprinted with permission from [73], copyright [2021, American Physical Society].

$$c'_R = c_R - \frac{\xi \chi_{yy}(H)}{4\rho\gamma^2\mu_0 c_t}, \quad (8)$$

where,  $\xi$  is a parameter determined by the transverse and longitudinal velocity component of bulk acoustic wave [40]. The field variation of  $\chi_{yy}(H)$  obeys anti-symmetric Lorentzian function. Namely, the acceleration and deceleration of the SAW appears depending on the sign of  $\chi_{yy}$ . The velocity modulation leads to a change in wavenumber of the SAW. Finally, the phase of SAW at the end of NiFe rectangle with a length of  $L$  is modulated according to the following equation:

$$\Delta\theta = L\Delta k \approx \frac{L\omega^3\chi_{yy}(H)}{4\rho\gamma^2\mu_0\xi c_t^2}. \quad (9)$$

From this equation, we can calculate the phase modulation of SAW as a function of external field at a given frequency. Figure 11(c) shows the numerically evaluated EdH phase shift. The calculated magnitude is similar to the experiment (see Figure 11(a)), although extrinsic loss of angular momentum conversion is not considered. Figure 11(d) shows the double-logarithmic plot of the phase shift as a function of reduced frequency. The dotted line indicates the best fit with a linear function. From Eq. 9, the amplitude of  $\Delta\theta$  is expected to be proportional to the square of  $\omega$  because  $\chi_{yy}$  is inversely proportional to  $\omega$ . The slope is consistent with the analytical solution of the EdH phase shift, which is steeper than in the magnetoelastic effect. This frequency variation of  $\Delta\theta$  supports that the EdH phase shifts occur in NiFe film, suggesting the reciprocity in the acoustic gyromagnetic effect.

### 3.5. Spin current generation in ubiquitous nonmagnetic metals by propagating surface acoustic waves [18,19]

Here, a demonstration of spin current generation using acoustic gyromagnetic effect in ubiquitous non-magnetic metals is discussed. Generally, non-equilibrium spin state is necessary for spin current generation. According to the microscopic theory [20,34], there are three effects that lead to non-equilibrium spin state. First is an energy shift of grand state due to the gyromagnetic Barnett field. Second is an angular momentum transfer from mechanical rotation. And third is an additional spin-flip relaxation via spin-vorticity coupling (SVC). As shown in the following spin diffusion equation, that is derived from the generalized Boltzmann equation with the SVC effects, two different spin sources are expected in the SVC theory.

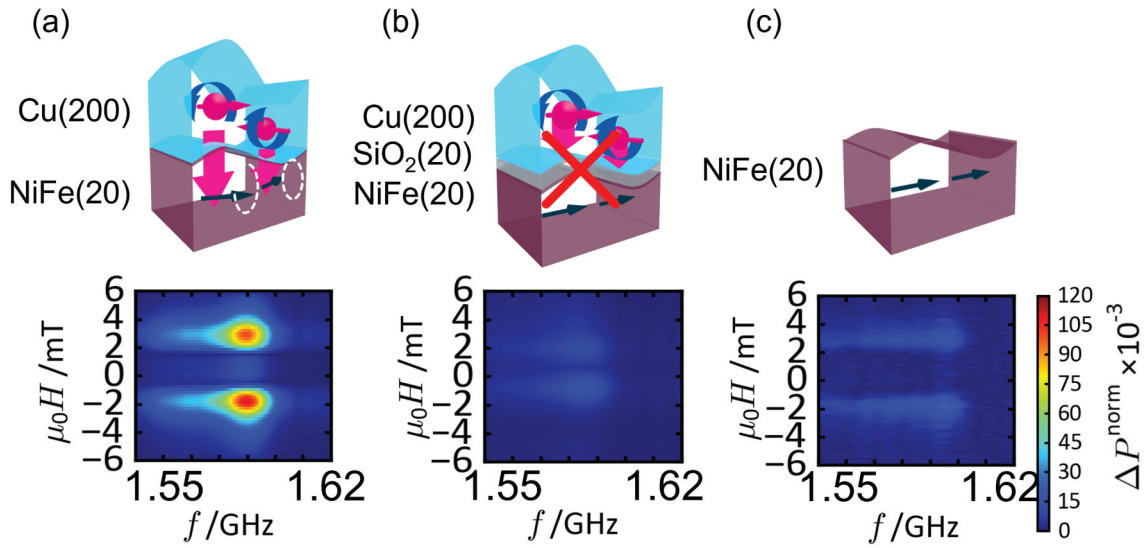
$$(\partial_t - D_s^2 + \tilde{\tau}_{sf})\delta\mu_s = -\frac{\hbar}{2}\partial_t\Omega - \hbar\frac{\zeta\Omega}{\tilde{\tau}_{sf}}. \quad (10)$$

The first source term in the left side of the spin diffusion equation depends on the temporal variation in the vorticity  $\partial_t\Omega$ , while the second one can be originated from the stationary vorticity  $\Omega$ . Indeed, a spin current generation with the stationary vorticity has been successfully demonstrated in hydrodynamic systems [35,36]. Here, the inverse spin Hall voltage produced by the spin current in a liquid mercury flow was measured, where laminar and/or turbulent flow made vortical motion of mercury atoms. An increase in the inverse spin Hall voltage was observed by increasing the velocity of mercury flow, that is consistent with the theory for the gyromagnetic effect. However, in such a liquid flow, it is hard to increase the vorticity higher than MHz order.

To increase the vorticity up to GHz order, we can use the vorticity in SAWs. As shown in Sec. 3.3, the Rayleigh SAW comprises elliptical particle motions in the vertical plane parallel to the wave vector. The vorticity of the elliptical motions produces the AC-Barnett field even in nonmagnetic metals. In the Rayleigh SAW, the magnitude of vorticity decays exponentially along the depth direction. Consequently, the gradient of such a non-uniform AC-Barnett field produces a temporally and spatially varying spin current. To demonstrate such a spin current generation using the SAW, the following experiments have been conducted.

Similar to the device used for studying gyromagnetic effect, a bilayer consisting of nonmagnetic Cu and ferromagnetic NiFe is deposited between IDT electrodes on a piezoelectric substrate. When the SAW propagates at the bilayer as schematically shown in Figure 12(a), a periodic AC spin current is generated in Cu via SVC and is diffused toward NiFe. Such a spin current periodically gives an alternating spin-transfer torque onto the magnetization and spin waves are subsequently excited. Owing to an energy balance in the bilayer, a damping of spin wave in the NiFe layer leads to SAW attenuation. Namely, we can evaluate the AC spin current from the SAW attenuation in such a bilayer system. The SAW attenuation propagating in the bilayer was measured using a method similar to the previous Barnett effect experiment.

Figures 12(a–c) show the color plots of SAW attenuation as a function of SAW frequency and external magnetic field for Cu/NiFe bilayer and its control samples. In these devices, the SAWs were intensely generated at 1.59 GHz. The external magnetic field was applied along the propagating direction of the SAW, where the spin-transfer torque from the spin current produced via gyromagnetic effect became maximum. A strong SAW attenuation appeared when the external field was applied so that the spin wave

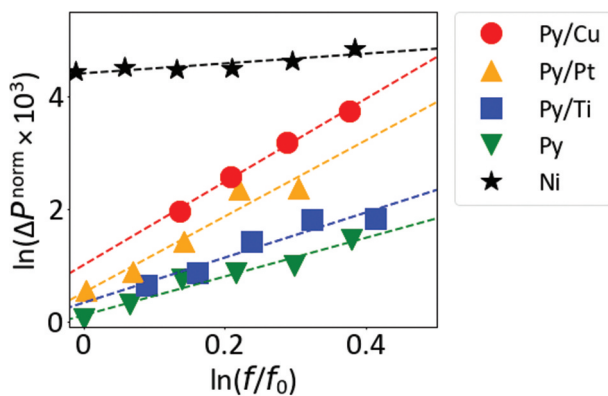


**Figure 12.** Color plots of SAW attenuation as a function of SAW frequency and external magnetic field measured for (a) NiFe(20)/Cu(200) bilayer, (b) NiFe(20)/SiO<sub>2</sub>(20)/Cu(200) trilayer, and (c) NiFe(20) single layer. All thicknesses are in nm. Preprinted with permission from [18], copyright [2017, American Physical Society].

resonance was excited, although the SAW attenuation was strongly suppressed by inserting a 20-nm-thick insulating SiO<sub>2</sub> film at the interface between Cu and NiFe or removing Cu film. These results qualitatively support that the spin current is generated in Cu via gyromagnetic effect and is injected to adjacent NiFe film.

### 3.6. Material dependence of acoustic gyromagnetic effects for understanding its microscopic mechanisms [19,74]

In this section, we will discuss the acoustic gyromagnetic effect from the view point of material science. Figure 13 shows the double logarithm plot of reduced SAW attenuation as a function of reduced SAW frequency. Stars and upside down triangles represent the data for Ni and NiFe single films, respectively. Here,



**Figure 13.** Double-logarithmic plot of the reduced SAW amplitude as a function of reduced frequency. Preprinted with permission from [19], copyright [2020, American Physical Society].

highly conductive Cu, poorly conductive Ti, and strong-SOI Pt for SC generator were compared to evaluate electric conductance- and SOI-dependencies of the efficiency of spin current generation, because it is theoretically predicted that the amplitude of spin current is proportional to the electrical conductivity and is independent of SOI strength. As shown in Figure 13, the intensity of magnetoelastic waves induced by SAWs significantly varies not only with the type of ferromagnetic material (e.g. high magnetostriction materials like Ni and low magnetostriction materials like NiFe) but also with the type of adjacent non-magnetic material. Furthermore, the slope of the double-logarithmic plot in Figure 13 differs considerably across materials. This indicates that the acoustic gyromagnetic effect exhibits distinct frequency dependencies, suggesting that multiple mechanisms could dominate depending on the material. In this review, we showed acoustic spin wave resonance excitations using magnetoelastic field (Sec. 3.3), Barnett field (Sec. 3.4), and spin-transfer torque (Sec. 3.5). This spin wave resonance can be distinguished from the difference in frequency variations of the spin wave amplitude. As shown in Eq. 2, the vorticity of the Rayleigh-SAW, i.e. local angular momentum, is proportional to the square of the angular frequency and amplitude of lattice deformation. The y-component of the vorticity  $\Omega^y$ , which leads to spin accumulation via the gyromagnetic effect, decays exponentially from the surface. The amplitude of the spin current is proportional to the gradient of the spin accumulation. Namely, the spin current is expected to be proportional to cubic and/or quartic of frequency for spin current sources with stationary and time-derivative of vorticity. In the case of Barnett field in ferromagnet, its amplitude is

simply proportional to vorticity itself, thus its amplitude shows 2nd power law with respect to frequency. The magnetoelastic field is typically proportional to the strain tensor, whose intensity is proportional to the frequency.

The following power loss formula [19]

$$\Delta P_{bi} \approx \frac{\gamma}{2\alpha} \left[ \frac{f^2}{f_z^2} \frac{\hbar^2}{4e^2 M_s d^2} |J_s|^2 + M_s |h_B^y|^2 + M_s |h_{ME}^{IP}|^2 + \frac{f^2}{f_z^2} M_s |h_{ME}^{OP}|^2 \right], \quad (11)$$

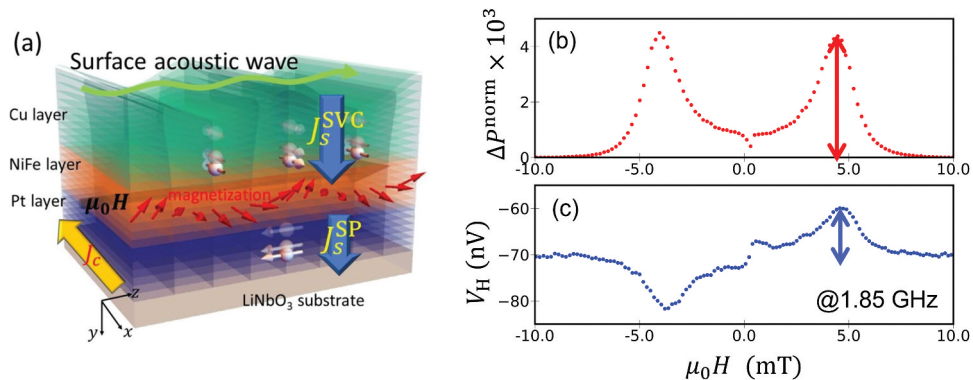
is associated with spin wave resonance by spin current  $J_s$ , Barnett field  $h_B^y$ , and inplane- and out-of-plane-magnetoelastic fields,  $h_{ME}^{IP}$  and  $h_{ME}^{OP}$ . Here,  $M_s$  and  $d$  are the saturation magnetization and thickness of the ferromagnetic layer.  $f_z$  is the material-dependent frequency, given by  $\gamma M_s / (2\pi\mu_0)$ . As shown in Fig. 10(c),  $\Delta P^{norm}$  is defined as  $\Delta P_{bi} / P_{SAW}$ . Since  $P_{SAW}$  scales with  $\omega u_0^2$ , the frequency dependence of  $\Delta P^{norm}$  is reduced by one order compared to  $\Delta P_{bi}$ . Therefore, the power law exponent for the frequency dependence of  $\Delta P_{bi}$  can be determined by adding 1 to the slope of the double-logarithmic plot in Figure 13. The magnitudes of  $h_{ME}^{IP}$  and  $h_{ME}^{OP}$  are proportional to frequency  $f$ , while that of  $h_B^y$  is in proportion to the square of  $f$ . The amplitudes of AC-spin current originated from  $\partial_t \Omega$  and  $\Omega$  in Eq. 10 show much higher-order frequency variations, i.e.  $f^4$  and  $f^3$ , respectively. Consequently, the frequency dependence of the SWR intensity strongly depends on the type of stimulus so that a predominant factor of the SWR excitation can be identified. All plots in Figure 13 are well fitted by linear functions, and the value of gradient gives the order of power law for  $\Delta P^{norm}$  with respect to frequency. The estimated slope of 3.4 for NiFe suggests that the Barnett effect, i.e. second term in right side of Eq. 11, predominantly appears because of its negligible magnetoelastic effect. It is also concluded that the magnetoelastic fields due to longitudinal and shear strains coexist in Ni film because the gradient is between 1 and 3, which are the power numbers of frequency dependence for the third and fourth terms in right side of Eq. 11, respectively. Indeed,

a nonreciprocal spin wave resonance has been observed in Ni, which is also attributed to the coexistence of longitudinal and shear strains [59]. In the case of bilayers, a much higher power law with frequency than the cases in Ni and NiFe single film is observed. NiFe/Cu and NiFe/Pt bilayers show approximately 7th power law with frequency. This means that the spin wave resonance is predominantly excited via spin-transfer torque with stationary vorticity  $\Omega$  in Eq. 10. In other words,  $\partial_t \Omega$  in Eq. 10 does not contribute to the acoustic spin current generation. This is reasonable by considering that the SAW frequency is much lower than the electron relaxation frequency. When a poorly conductive Ti is combined with NiFe, the order of the power law clearly decreases from 7th to 5th. The result qualitatively supports that the spin current generated via SVC can be increased in high electrical conductivity metals as expected theoretically.

Finally, the conversion efficiency of angular momentum in SAW is discussed. From the SVC theory, the acoustic spin current originated from  $\Omega$  is deduced as the following equation:

$$j_s = \frac{\sigma_0}{e} \frac{\partial}{\partial z} \delta \mu_s \approx -i\zeta \frac{\hbar \sigma_0 u_0 \omega^3}{2ec_t^2} \frac{z}{\lambda_s} e^{i(kx - \omega t)}, \quad (12)$$

where  $\sigma_0$  and  $\lambda_s$  are the electrical conductivity and spin diffusion length of the nonmagnetic layer, respectively.  $\zeta$  is a renormalization factor, which is originated from the coarse-graining procedure of the lattice motion and represents the conversion efficiency of angular momentum from lattice into electron spins. It is hard to determine the magnitude of  $\zeta$  numerically in practical spin devices. Below, we tried to determine  $\zeta$  experimentally from the analytical relationship between the amplitudes of SAW deformation and AC spin current. As schematically shown in Figure 14(a), the amplitude of the AC spin current can be evaluated from the inverse spin Hall voltage produced in Pt/NiFe/Cu trilayer by applying SAW. The spin wave resonance in the NiFe (see Figure 14(b)) pumps DC spin current into an adjacent Pt layer, which leads to an inverse spin Hall voltage as shown in Figure 14(c). According to the conventional



**Figure 14.** (a) Schematic principle for measuring SAW-related AC spin current using spin-pumping effect in Pt/NiFe/Cu trilayer film. (b) SAW absorption and (c) inverse spin Hall voltage caused by spin wave resonance excitation. Preprinted with permission from [74], copyright [2020, American Physical Society].



theories for spin pumping and magnetization dynamics [75], the AC spin current can be evaluated from the inverse spin Hall voltage. Moreover, as shown in Sec. 3.4.1, the SAW amplitude can be determined from the SAW attenuation. Finally, the value of  $\zeta$  in Eq. 12 is obtained as large as  $2.6 \times 10^6$ , which is four orders of magnitude larger than the value reported for liquid mercury flow [34]. Generally, the conversion efficiency of angular momentum is improved for systems with smaller difference in the energy scale. Such a large renormalization factor is attributed to that the frequency of SAW vorticity is six orders of magnitude higher than in the liquid mercury flow.

The acoustic gyromagnetic effect induced by SAWs is understood as an inertial torque caused by lattice rotation acting on the conduction electron spin. However, the specific spin confinement conditions responsible for generating this torque have been rarely addressed, and it is still unclear which material systems can best enhance the effect. Investigating how crystallinity influences the acoustic gyromagnetic effect could offer valuable insights into how variations in spin confinement affect the phenomenon. Additionally, studying the temperature dependence of the intensity and frequency response of magnetoelastic waves induced by the effect is crucial for deepening our understanding from a materials science perspective and represents a key area for future research.

#### 4. Current-vorticity gyromagnetic effect

In this section, an overview of recent research on the vorticity in electron motion and its coupling with electron spins is provided. Early works that demonstrate the generation of vorticity in electron motion are reviewed first. After that, alternative methods using composition gradient interface (CGI) between materials with different electrical conductivity, which produce current vorticity, are outlined. Finally, the characteristic electron-spin conversion behavior observed in CGIs is discussed, highlighting the origins of the coupling between electron motion vorticity and electron spins.

#### 4.1. Vorticity in electron motion

Various systems in nature can commonly provide vortical motion, which couples with electron spins via gyromagnetic effect, which is referred to as spin-vorticity coupling (SVC). In the SVC theory, the total angular momentum, i.e. the sum of macroscopic vortical motion and the microscopic angular momentum of electrons is conserved not only globally but also locally. As a consequence, a gradient of macroscopic angular momentum generates spin currents. This subsection introduces several pioneering studies that propose methods for generating macroscopic electric current vorticity aimed at coupling with electron spins.

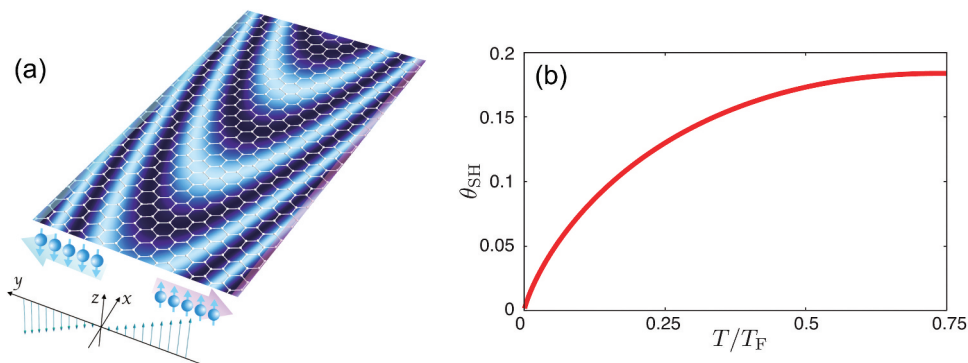
##### 4.1.1. Electron fluids in graphene [76]

In monolayer graphene, electron scattering is mainly governed by Coulomb interactions between electrons. In this system, the flow of electrons is regarded as a classical liquid with viscosity. A finite flow channel of the electron liquid, therefore, produces nonuniform current distribution accompanied by vorticity, which leads to non-equilibrium spin states via the following SVC:

$$H = -\frac{1}{2} \mathbf{S} \cdot \boldsymbol{\Omega}(\mathbf{r}), \quad (13)$$

$$\boldsymbol{\Omega}(\mathbf{r}) = \nabla \times \mathbf{u}(\mathbf{r}). \quad (14)$$

where  $\mathbf{S}$  is the spin of conduction electrons and  $\mathbf{u}(\mathbf{r})$  is the drift velocity of the electrons. By solving the Navier–Stokes equation for electron flow and the spin diffusion equation that includes the SVC, the spin Hall effect arises in graphene, whose spin Hall angle is approximately at 0.1 in both Poiseuille and Jeffery–Hamel flows, surpassing the value of platinum commonly used in conventional spin Hall devices. Graphene, known for its weak spin–orbit interaction and long spin diffusion length, is a promising spintronic material alternative to rare metals like platinum. Figure 15 (a) schematically shows that in the Poiseuille flow region, a current flowing in the  $x$ -direction generates a spin current in the  $y$ -direction. Figure 15 (b) presents the numerical



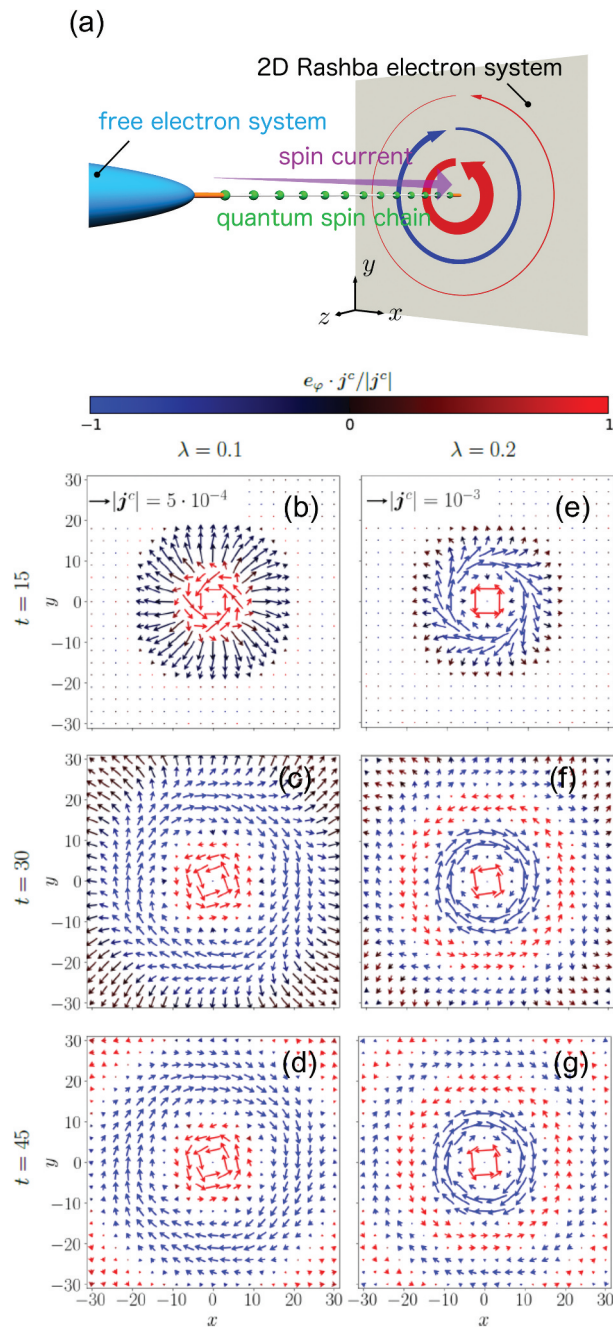
**Figure 15.** (a) Current-spin conversion due to spin-vorticity coupling in graphene. (b) Temperature dependence of the spin Hall angle ( $\theta_{SH}$ ) in graphene (with  $T_F$  denoting the Fermi temperature, approximately 100 K) Reprinted from [76].

temperature dependence of the spin Hall angle ( $\theta_{SH}$ ) in graphene.  $T_F$  denotes the Fermi temperature, estimated to be approximately at 100 K. The computational framework based on fluid dynamics equations can also be applied to the non-uniform current flows expected in gradient materials.

#### 4.1.2. Current-vorticity generation via spin currents in Rashba systems [77,78]

As shown in Figure 16(a), the current distribution was calculated using the block Lanczos density matrix renormalization group method when a 2D Rashba

electron system is connected to a quantum spin chain, and spinon spin current is injected. Figures 16 (b–d) and (e–g) illustrate the time evolution of current vortices generated in the 2D Rashba electron system with two different SOI amplitudes. By injecting a spinon spin current perpendicular to the 2D Rashba electron system locally, current vortices are generated in the 2D Rashba electron system. Furthermore, the rotation direction of the current vortex reverses depending on the distance from the injecting point. Fujimoto et al. also investigate the current vortex generation by another spin injection



**Figure 16.** (a) Numerical model for calculating current distribution using the block Lanczos density matrix renormalization group method. A 2D Rashba electron system is connected to a quantum spin chain, and free electrons are injected. Time evolution of current vortices generated in the 2D Rashba electron system. (b–d) and (e–g) are the results calculated for reduced SOI strength  $\lambda = 0.1$  and  $0.2$ , respectively. Preprinted from [77], copyright [2021, American Physical Society].

method, local spin pumping [78]. In future electronics, spin currents are used due to its lower energy loss compared to charge currents for energy and information transfer. It is expected that not only diffusive current but also hydrodynamic regimes of current flow, such as laminar and turbulent states, are rapidly increasing in importance for controlling of spin current. The generation of current vortices from spin currents as shown in Figure 16 represents one of the expansions of spintronics into the hydrodynamic regime. Additionally, since current vortices can generate magnetic fields and electromagnetic waves, this finding significantly broadens the scope of spintronics as a next-generation quantum technology.

#### 4.1.3 Current vorticity in geometrical structures [79]

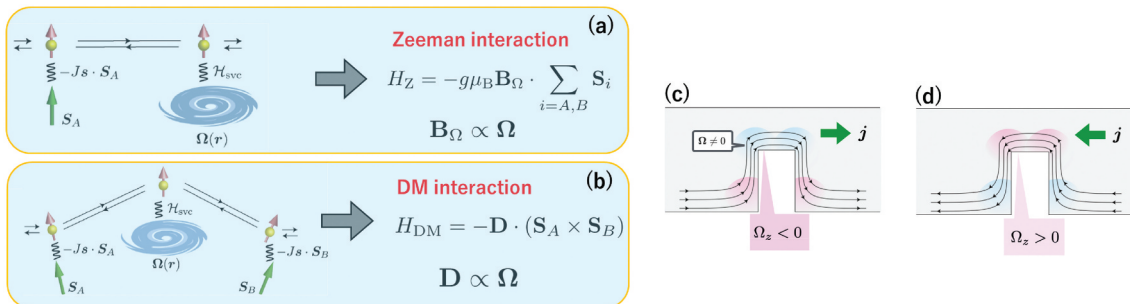
Fujimoto et al. theoretically investigated the effective interactions on localized spins (proportional to magnetization) as electrons couple not only with localized spin via s–d interaction but also with macroscopic current vorticity via SVC in metals. According to their theory, the second-order perturbation leads to effective Zeeman coupling on localized spins via SVC as shown in Figure 17(a). The effective Zeeman magnetic field  $B_\Omega$  is proportional to the vorticity  $\Omega$ . Additionally, they found another higher-order effect in SVC as depicted in Figure 17(b), where third-order perturbation induces effective Dzyaloshinsky–Moriya (DM) interaction between two localized spins through vorticity coupling. The strength of the DM interaction  $D$  also proportional to the vorticity  $\Omega$ . Since the vorticity of the current  $\Omega = \nabla \times \mathbf{v}$  is given by the rotation of the drift velocity field  $\mathbf{v}$ ,  $B_\Omega$  and  $D$  can reverse their sign by changing the current direction. As shown in Figure 17(c,d), when current flows through a sample with a notch structure, positive and negative current vortices form near the edges (indicated in red and blue in the figure). Therefore, effective Zeeman coupling and DM interaction with reversed signs occur in these

regions, and they can be reversed by changing the current direction. Their theory may explain the experiments on magnetic skyrmion creation and annihilation in FeGe thin films with a notch structure [80]. Utilizing such macrostructures could lead to the development of new spin materials mediated by current vortices.

#### 4.2. Fabrication and structural analysis of gradient materials

In the methods presented in Section 4.1.1–4.1.3, electron fluid viscosity, spin–orbit interaction, or geometrical structures were essential for generating current vorticity. Alternatively, if a spatial gradient in electrical conductivity is established, a non-uniform distribution arises in drift currents under an applied electric field, generating current vorticity. To achieve charge-to-spin current conversion efficiently in gradient structures composed of materials with different electrical conductivities, it is essential to identify key factors in structural and material parameters. Namely, we need well-defined gradient structures with achieving atomic-level control over thin film growth. Various methods for fabricating gradient materials with nanoscale conductivity gradients in the film thickness direction have been proposed, e.g. (i) creating a compositional gradient by oxidizing the surface of metallic thin films, (ii) gradual control of atomic diffusion of sputtering particles with high kinetic energies, and (iii) epitaxial growth with precise compositional changes during sputtering.

While the method (i) is the simplest way to produce compositional gradient structures, it is challenging to control the oxidation depth precisely and reproducibly at the nanoscale. In contrast, method (iii) involves the precise modulation of composition at the atomic layer level while growing epitaxially, resulting in extremely smooth gradient interfaces with controlled crystal



**Figure 17.** Schematic principle for (a) effective Zeeman coupling and (b) effective Dzyaloshinsky–Moriya (DM) interaction, which is mediated by spin-vorticity coupling between conduction electron spin and macroscopic current vorticity and localized spins. Current vorticity generated when current flows through a sample with a notch structure. (c) Positive and (d) negative current vortices form near the edges (indicated in red and blue in the figure). Reproduced by permission from [79], copyright [2021, American Physical Society].



structures. It is suitable for evaluating the spin current generation characteristics due to the gyromagnetic effect of current vorticity at compositionally gradient interfaces. However, method (iii) is restricted to material combinations with high lattice compatibility and stable crystal structures, despite compositional changes. This limitation makes it difficult to vary physical parameters such as electrical conductivity, mobility, carrier concentration, mean free path, and spin-orbit interaction, which may affect the coupling between current vorticity and spin angular momentum. Method (ii), on the other hand, realizes gradient structures by physically diffusing atoms using the momentum of sputtering particles. This method allows for a broader range of material combinations compared to epitaxial growth with compositional changes.

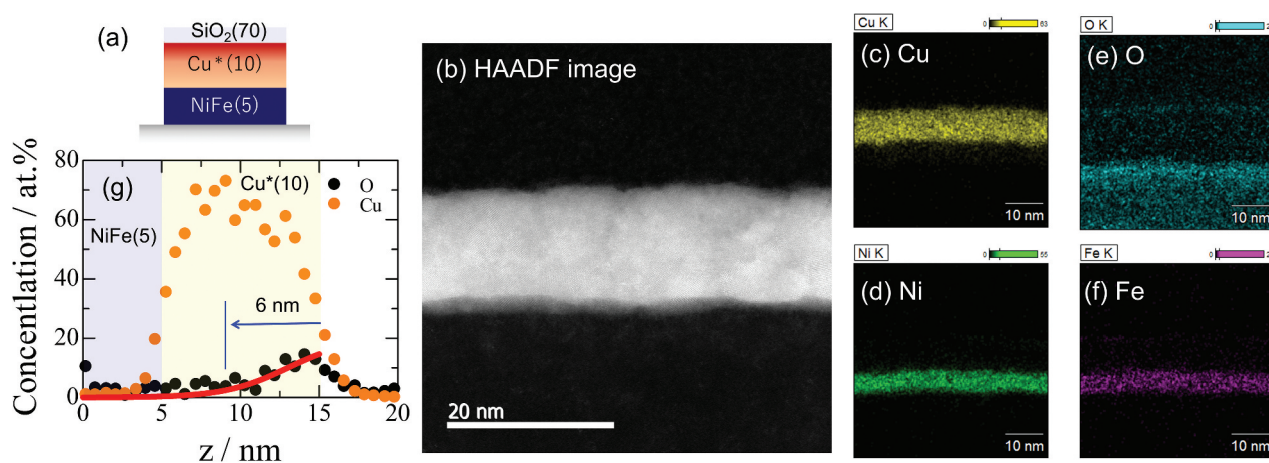
Thus, it is important to understand the characteristics of each method and select the appropriate one according to the purpose when fabricating gradient materials. This subsection briefly introduces these fabrication methods and their structural analyses.

#### 4.2.1. Gradient modulation of oxidization level

The progress of oxidization at the surface of metallic thin film is generally established by the nucleation of oxide island on surface followed by the diffusion of oxygen in depth direction. Figure 18 shows the high-angle annular dark field scanning transmission electron microscope (HAADF-STEM) image and energy-dispersive X-ray spectroscopy (EDS) profile for the bilayer consisting of 5 nm thick NiFe and 10 nm thick surface-oxidized Cu. To achieve a gradient modulation of oxidization level, the Cu film was exposed for 40 hours in air at room temperature. 70 nm thick SiO<sub>2</sub> was then capped to stop the oxidization. As shown in Figure 18(g), the penetration of oxygen atoms was stopped approximately at 6 nm from the

surface. According to the study by Masudome et al., who utilized time-of-flight secondary ion mass spectrometry (ToF-SIMS) for chemical depth profiling of Cu-oxide films, a few nm thick Cu(OH)<sub>2</sub>/CuO/Cu<sub>2</sub>O layered structure was formed at the naturally oxidized Cu film [81]. The electric conductivities of these Cu oxides and Cu hydroxide are much lower than the value for bare Cu. The gradual decrease in oxygen composition along the thickness direction is attributed to the decrease in the volume ratio of these Cu oxides and Cu hydroxide with low electric conductivities. Namely, such a gradient oxide, therefore, leads to the electric current vorticity with applying electric field along the film plane.

In a pioneer work by An et al., such a surface-oxidized Cu film displays a large spin torque comparable to the value for Pt [83]. They conducted the spin torque (ST-) FMR experiment, whose principle is summarized in Appendix A.1., on the bilayer consisting of NiFe and surface-oxidized Cu. In the spin-torque FMR measurement, amplitudes of symmetric and anti-symmetric components are measured to evaluate damping-like and field-like spin torques, respectively. The anti-symmetric component is also produced by the Oersted field torque so that the magnitude of the symmetric component is, therefore, a good indicator for the spin-torque generation. From the analysis of spin-torque FMR spectrum, they found that the surface-oxidized Cu shows a spin-torque efficiency as large as Pt. However, the origin of spin torque in such a surface-oxidized bilayer is still controversial, e.g. SVC due to current vorticity [82], enhancement of spin-orbital coupling (SOC) caused by the hybridization with oxide atoms [84,85]. It has also been reported that the interface between copper and its oxides shows large orbital REE [86], which can give rise to a torque on adjacent magnetic thin film via SOC.



**Figure 18.** (a) Schematic cross section of bilayer consisting of composition gradient Cu oxide and ferromagnetic NiFe layers. (b-f) High-angle annular dark field scanning transmission electron microscope (HAADF-STEM) image and (g) energy dispersive X-ray spectroscopy (EDS) profile for the bilayer consisting of 5 nm thick NiFe and 10 nm thick surface-oxidized Cu. Preprinted from [82], copyright [2019, American Physical Society].



#### 4.2.2. Composition gradient using atomic diffusion in alternating deposition layers [87]

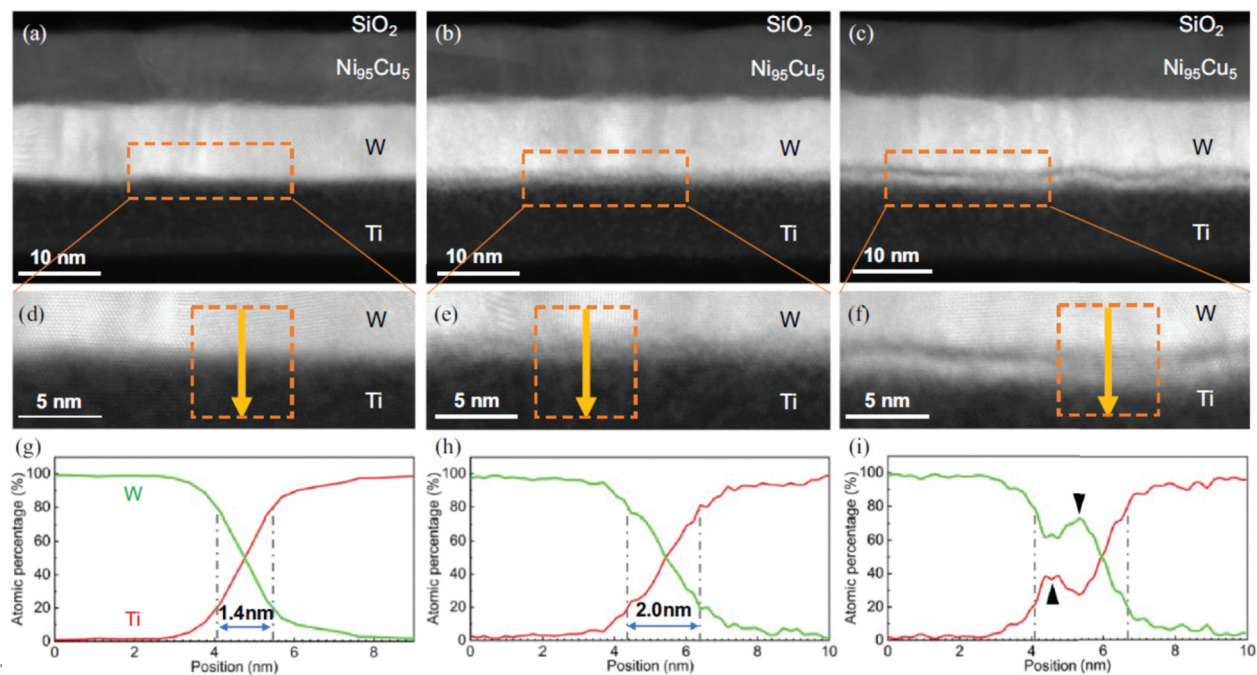
To demonstrate spin current generation by current vorticity in composition-graded materials, it is crucial to fabricate materials with graded electrical conductivity across various systems. Investigating the correlation between the conductivity gradient structure and spin current generation efficiency, along with non-reciprocal charge-to-spin current conversion, will distinguish this phenomenon from the conventional spin Hall effect driven by reciprocal bulk or interfacial spin-orbit interactions (SOI). In this section, we introduce graded materials with nanoscale modulation of high-conductivity  $\alpha$ -tungsten ( $\alpha$ -W) and low-conductivity titanium (Ti), along with evaluations of their structure and chemical composition.

Samples were fabricated by inserting a  $W(t_i/2)/Ti(t_i/2)$  bilayer between 10 nm thick Ti and  $\alpha$ -W layers using magnetron sputtering, followed by a deposition of ferromagnetic Ni-Cu alloy on top. Here, the value of  $t_i$  is ranging from 0 to 2 nm at intervals of 0.5 nm. In this process, post-sputtered particles are mixed with the previously deposited material, resulting in a structure where the composition continuously changes from Ti to W at the interface between 10 nm thick Ti and W layers. According to the binary alloy phase diagram [88], Ti and W scarcely dissolve in each other at the atomic level. However, as the sputtered particles are rapidly cooled on the substrate, a metastable phase with atomic level mixing will appear. Both electron and spin scattering in the gradient region are strongly

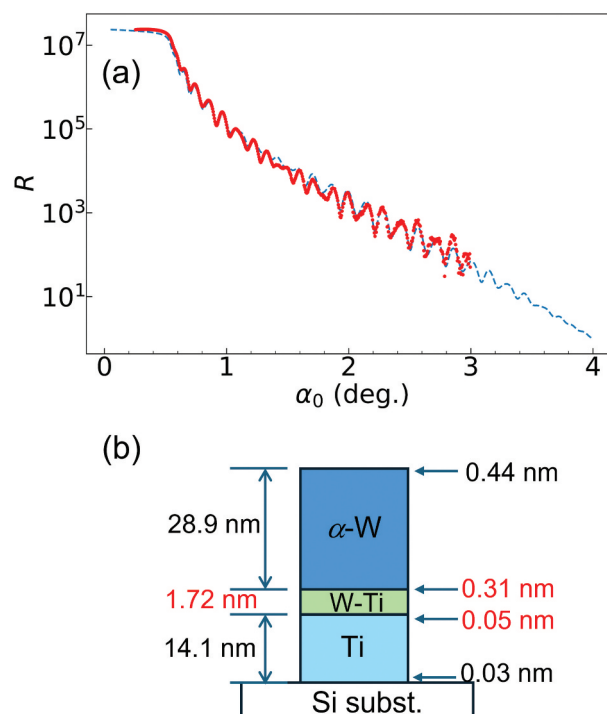
affected by whether Ti and W are mixed at the atomic level or form fine microstructures such as microcrystals. Namely, it is significant to evaluate the microstructures of the graded interface, which generates the spin current by the current vorticity.

Figures 19(a), (b) and (c) show HAADF-STEM images of the Ti/W interface with an insertion layer thickness  $t_i$  of 0, 1.0, and 2.0 nm, respectively. Figures 19(d), (e) and (f) are the magnified images of the dashed boxed area in Figures 19(a), (b) and (c), respectively. The interface with  $t_i = 1.0$  nm is a mixed state, whereas Ti and W begin to separate from each other in sample with  $t_i = 2.0$  nm. Such microstructures depend not only on the insertion layer thickness but also on deposition conditions such as substrate temperature and sputtering rate. Figures 19(g), (h) and (i) show averaged compositional distributions along the stacking direction for samples with  $t_i = 0, 1.0$ , and 2.0 nm, respectively. For samples with  $t_i = 0$  and 1.0 nm, the compositional distribution can be well fitted with a tanh function, with the composition gradient width  $L$  approximately corresponding to the insertion layer thickness  $t_i$ . When the insertion layer exceeds the atomic mixing thickness ( $<1$  nm), the layers begin to separate into Ti and W.

Blue circles in Figure 20(a) present the X-ray reflectivity (XRR) as a function of X-ray incident angle measured for the Ti/W bilayer with  $t_i$  of 1 nm. From the XRR profile, which is measured near the total reflection condition with X-rays incident at extremely low angles, we can determine interfacial



**Figure 19.** HAADF-STEM images and corresponding EDS profiles for samples with  $t_i$  equal to (a), (d), and (g) 0 nm, (b), (e), and (h) 1.0 nm, and (c), (f), and (i) 2.0 nm. The corresponding EDS profiles (g), (h), and (i) were generated from the region enclosed by the dashed box in the HAADF-STEM images (d), (e), and (f), respectively. Preprinted from [87], copyright [2023, American Physical Society].



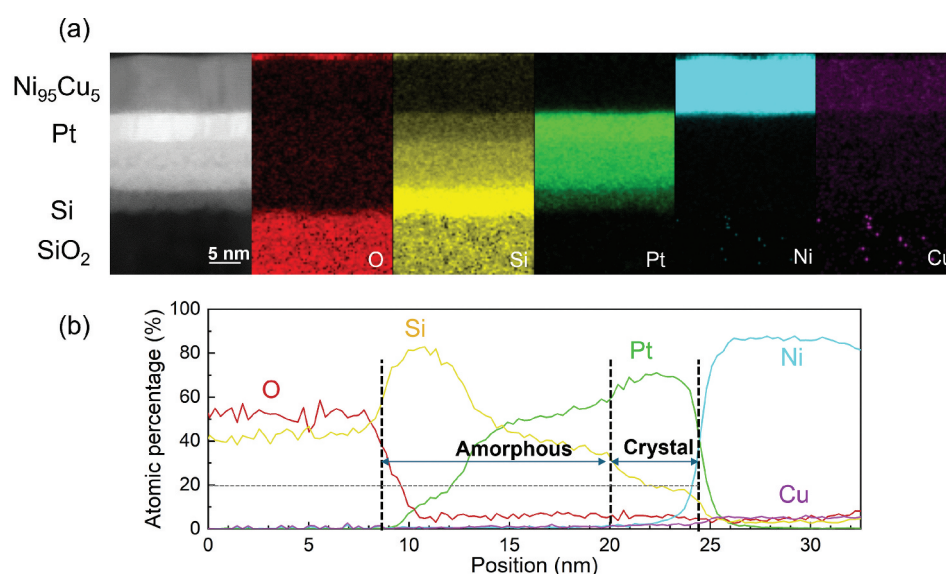
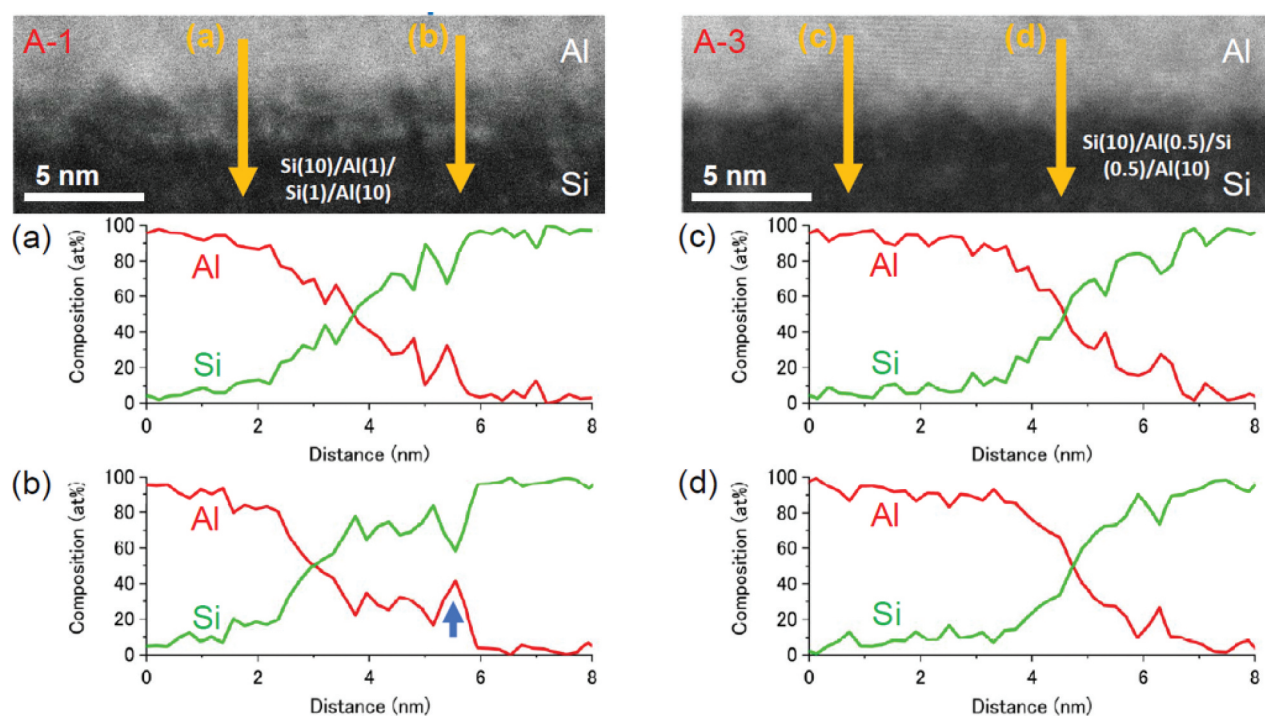
**Figure 20.** (a) X-ray reflectance (XRR) as a function of X-ray incident angle measured for the Ti/W bilayer with  $t_i$  of 1 nm. Blue and red circles represent the experimental and numerical data, respectively. (b) Three-layer model used to analyze the XRR profile of Ti/W gradient material with  $t_i = 1.0$  nm, along with the analytically obtained values for thickness and roughness of each layer and interface.

roughness, film density, and film thickness. The XRR pattern was analyzed using a three-layer model illustrated in Figure 20(b), where the gradient interface was approximated as a uniformly mixed alloy layer. Red circles in Figure 20(a) show the numerically evaluated XRR pattern using the three-layer model. The  $R$  factor, representing the discrepancy between measurement and numerical analysis, is 2.7%, which is less than half of the value for sample with  $t_i = 2.0$  nm. The total amount of thickness and roughness of the alloy layer obtained from the numerical analysis is 2.1 nm, consistent with the cross-sectional observation shown in Figure 19(h).

To increase the difference in electrical conductivity, namely, to improve the efficiency of spin current generation by the current vorticity, we have also fabricated composition gradient materials with nanoscale modulation of high-conductivity polycrystalline metal (Al) and low-conductivity amorphous semiconductor (Si). Figure 21 shows the HAADF-STEM images and corresponding EDS profiles for Si/Al interfaces with  $t_i = 1.0$  and 2.0 nm. The binary alloy phase diagram shows that Si and Al scarcely dissolve in each other at the atomic level [89]. As shown in Figure 21, a few nm-wide composition gradient interface is successfully produced in the sample with  $t_i = 1.0$  nm,

meanwhile some Al agglomeration appears in the sample with  $t_i = 2.0$  nm. These trends are similar to the case in Ti/W samples.

However, the interfacial structure changes drastically when Al is replaced by Pt. Figure 22 shows the HAADF-STEM image and corresponding EDS elemental distribution profile of Si/Pt sample fabricated similarly to Si/Al sample. Here, the insertion layer thickness  $t_i$  was 1.5 nm. Unlike the Si/Al bilayer film with a compositional gradient interface, the width of the mixed region becomes much wider than the thickness of the insertion layer. This suggests that there are appropriate elemental combinations for which a nanometer-scale compositional gradient can be achieved using alternating deposition technique. Si and Al form a non-soluble system with few intermetallic compounds, while the Si/Pt phase diagram contains many intermetallic compounds [91]. When sputtered particles are mixed, they tend to stabilize thermodynamically at specific compositional ratios, preventing the formation of a thermodynamically non-equilibrium compositional gradient structure. Therefore, achieving a compositional gradient interface through alternating sputtering requires combining elements with significant differences in electrical conductivity and without solubility regions or intermetallic compounds in their binary alloy phase diagrams.



**Figure 22.** (a) HAADF-STEM images and (b) corresponding EDS profiles for Si/Pt sample with  $t_i = 1.5$  nm.

#### 4.2.3. Material development toward epitaxial composition gradients [92,93]

Compositional gradients using epitaxial thin films are promising for investigating the effectiveness of spin current generation by current vortices. The use of continuous composition gradient solid solutions based on epitaxial thin films can eliminate the effects of grain boundaries and crystal misorientation that are unavoidable in polycrystalline thin films. Here, we introduce the development of metallic epitaxial systems for the formation of resistive nano-gradients:

Ru/Cu nano-layered structure [92] and non-equilibrium Ru-Mo alloys [93]. It is well known that when a metallic element is doped into another metallic element, the electrical resistivity increases with its concentration (Nordheim rule). Therefore, if the alloy composition can be modulated in a nanoscale region within a compositional range that can sustain epitaxial growth, epitaxial resistive nano-gradient structures can be fabricated. In addition, using epitaxial growth, atomic layers can easily be controlled, and thus nano-stacked structures between different

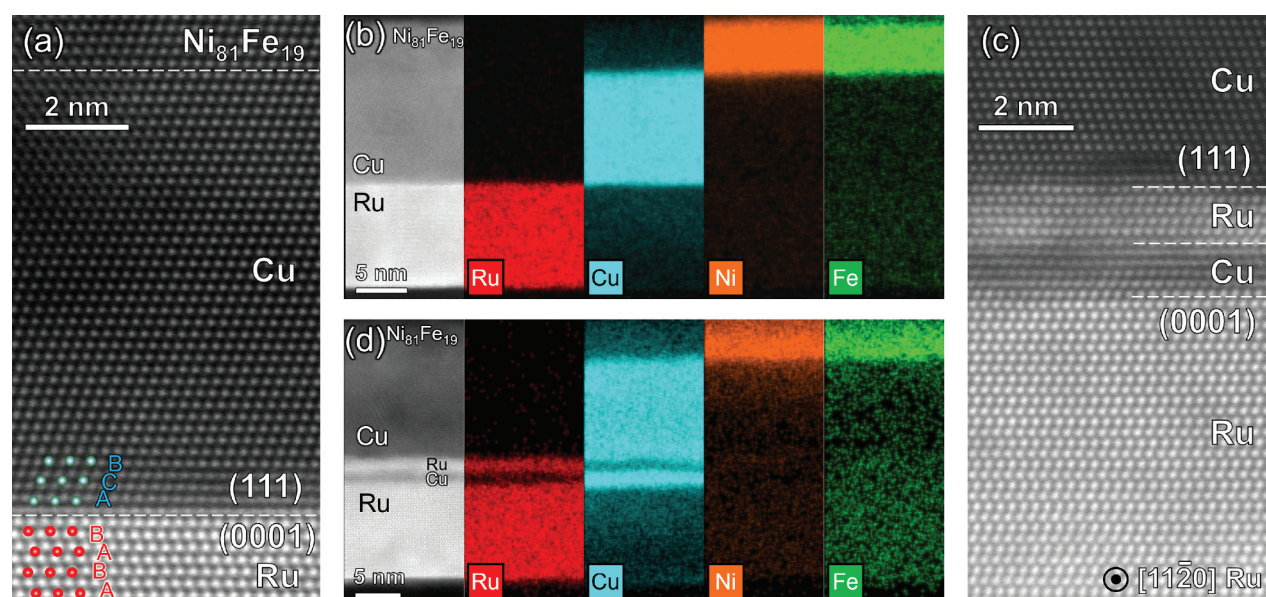


metals or alloys can also be prepared. Therefore, in addition to nano-compositional gradients, nano-layered structures can also be used to develop new spin current generation layers. To prepare such epitaxial gradient structures stably, it is important to (1) combine elements with close lattice spacings to achieve epitaxial heterostructures with high crystallinity and (2) use elements with high melting points to prevent composition homogenization by atomic diffusion in the nano gradients during the device fabrication processes.

First, the nano-stacked structures using epitaxial growth of Ru/Cu are introduced [92]. Since Ru-Cu is a completely immiscible system and the lattice mismatch between hcp-Ru(0001) and fcc-Cu(111) is small, an extremely sharp interface can be realized. Figures 23(a) and (b) show the cross-sectional HAADF-STEM images and EDS elemental maps of the epitaxial Ru(0001)/Cu(111)/NiFe(111) lattice-matched structure deposited by magnetron sputtering on a sapphire(0001) substrate, respectively. As shown in Figure 23(b), the elemental maps indicate that each interface is chemically sharp. In addition, when the nano-stacked structure with Cu 1 nm/Ru 1 nm was inserted at the Ru/Cu interface, relatively sharp and lattice-matched nano-stacking was realized at each Ru/Cu interface, as shown in Figure 23(c) and (d). Figure 24 shows the unidirectional spin Hall magnetoresistance (USMR) measurement results for the Ru/Cu structure and the stacks with nano-Ru/Cu layers. The principle and measurement method are briefly summarized in Appendix A.2. Figure 24 (a) shows

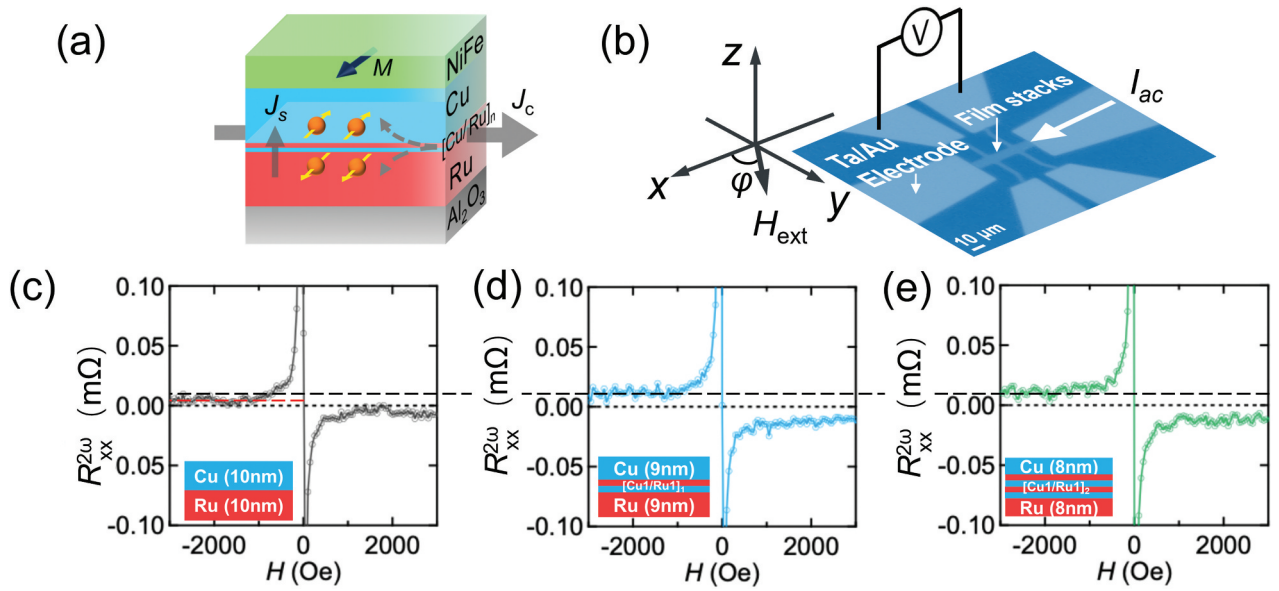
the schematic of the full stack structure and Figure 24(b) shows the Hall bar structure for the USMR measurement. Figures 24(c), (d), and (e) show the magnetic field dependence of Ru/Cu (no nano-insertion), Ru/[Cu/Ru]<sub>1</sub>/Cu, and Ru/[Cu/Ru]<sub>2</sub>/Cu structures, respectively (current density  $J_c = 14 \text{ MA/cm}^2$ ). The signal at high magnetic fields increases by a factor of 3 for the structures (d) and (e) with the nano-stacked layers. This result indicates an increase in the spin-charge conversion efficiency due to the artificial nano-stacking.

Next, we present an example of non-equilibrium alloys of Ru and Mo as a promising compositional gradient epitaxial system. Since both Ru and Mo have high melting points, it may be promising if a wide compositional range could be continuously modulated as an epitaxial film. In the bulk, the Ru side of the Ru-Mo system has an hcp structure, and the Mo side has a bcc structure; it shows a two-phase separation between the two near the Ru<sub>50</sub>Mo<sub>50</sub> composition. As shown schematically in Figure 25(a), the introduction of a 0.7 nm thick Ru layer on a sapphire (0001) substrate led to epitaxial growth of Ru-Mo alloy films. Here, the Ru-Mo was deposited by magnetron co-sputtering of pure Ru and pure Mo at a substrate temperature of 700 °C. Figure 25(b) shows a cross-sectional STEM image of the Ru<sub>50</sub>Mo<sub>50</sub> film in which A-B type atomic stacking is realized. Figure 25(c) shows the EDS elemental maps of the Ru<sub>50</sub>Mo<sub>50</sub> film. There is almost no atomic diffusion from the substrate. These observations indicate the formation of an atomically homogeneous hcp non-equilibrium Ru-

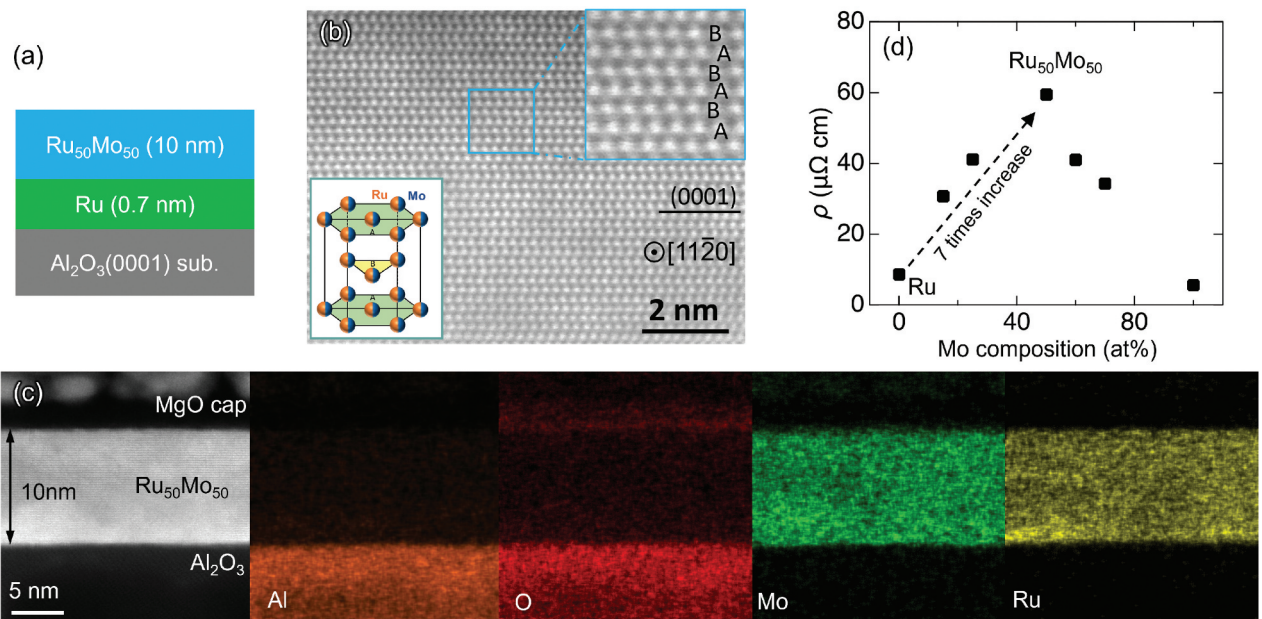


**Figure 23.** (a) and (c) Cross-sectional HAADF-STEM images of epitaxial Ru/Cu based stacks on Al<sub>2</sub>O<sub>3</sub> (0001) substrates: (a) Ru (10 nm)/Cu (10 nm)/NiFe, and (c) Ru (9 nm)/Cu (1 nm)/Ru (1 nm)/Cu (9 nm)/NiFe. (b) and (d) The corresponding EDS elemental maps of the stacks of (a) and (c), respectively. STEM and EDS images were reproduced with permission from [92], copyright [2023, IOP Publishing].





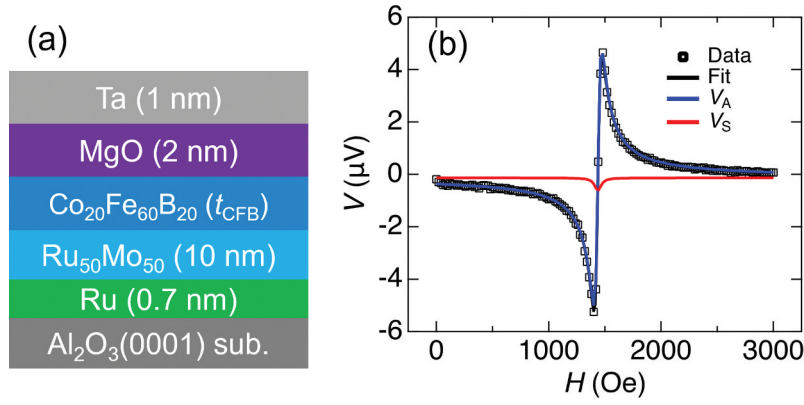
**Figure 24.** (a) Schematic of the full stack structure with Ru/Cu layers. (b) Hall bar structure for the USMR measurement. (c), (d), and (e) Magnetic field dependence of USMR signals; (c) Ru/Cu, (d) Ru/[Cu/Ru]<sub>1</sub>/Cu, and (e) Ru/[Cu/Ru]<sub>2</sub>/Cu structure. Figures were reproduced with permission from [92], copyright [2023, IOP Publishing].



**Figure 25.** (a) Schematic of the stack structure of an Ru<sub>50</sub>Mo<sub>50</sub> epitaxial layer. (b) HAADF-STEM image of the Ru<sub>50</sub>Mo<sub>50</sub> epitaxial layer. (c) EDS maps of the Ru<sub>50</sub>Mo<sub>50</sub> epitaxial layer. (d) Nominal Mo composition dependence of film resistivity  $\rho$ . Inset of (b): atomic model of the non-equilibrium Ru<sub>50</sub>Mo<sub>50</sub> alloy. Reproduced from [93].

Mo(0001) film, as schematically shown in the atomic model in the inset of (b). Figure 25(d) shows the nominal Mo composition dependence of the film resistivity  $\rho$ . The  $\rho$  increases significantly with increasing Mo composition according to the Nordheim rule. The  $\rho$  of the Ru<sub>50</sub>Mo<sub>50</sub> is about 7 times higher than that of a pure Ru film. Next, a stack with an Ru<sub>50</sub>Mo<sub>50</sub>/CoFeB magnetic layer as schematically shown in Figure 26(a) was fabricated to evaluate the spin Hall efficiency ( $\xi_{DL}$ ) using ST-FMR measurements. As

shown in Figure 26(b), the symmetric signal ( $V_s$ ) is much smaller than the antisymmetric signal ( $V_A$ ), indicating that the spin current generation in the RuMo alloy film is small. In fact, the  $\xi_{DL}$  was estimated to be 0.4% from the CoFeB thickness dependence. Thus, RuMo non-equilibrium alloys can realize epitaxial growth over a wide Mo composition range, and the spin Hall effect is very small, which will be a suitable material system for investigating the spin current generation effect via current vorticity.



**Figure 26.** (a)  $\text{Ru}_{50}\text{Mo}_{50}/\text{CoFeB}$  stack structure for ST-FMR measurements. (b) Typical ST-FMR signals and fits for CoFeB ( $t_{\text{CFB}} = 5.6$  nm). Reproduced from [93].

### 4.3. Spin-torque efficiency in composition gradient materials

In this subsection, we outline the spin-torque efficiency characteristics of gradient materials that support spin current generation from current-vorticity gradients.

#### 4.3.1. Surface-oxidized copper films [82]

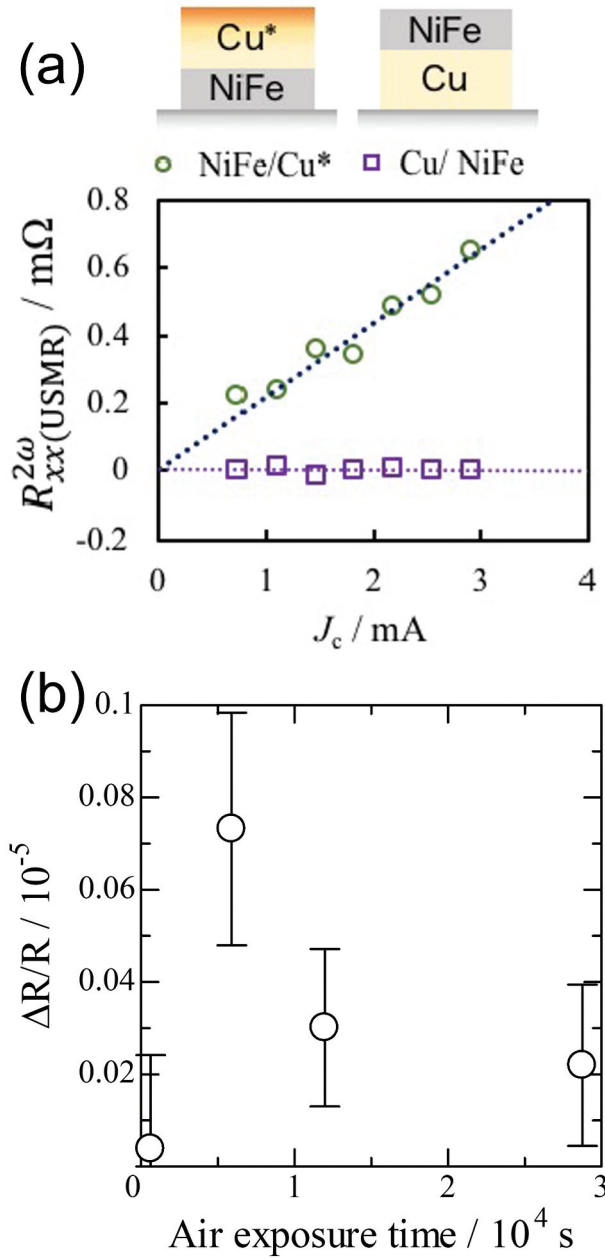
The charge-to-spin conversion efficiency for surface-oxidized Cu thin film was evaluated by measuring the USMR effect. Figure 27(a) shows the magnitude of the USMR signal  $R_{xx}^{2\omega}$  as a function of charge current  $J_c$  for surface-oxidized Cu layer covered with ferromagnetic NiFe layer. For comparison, the data for bilayer consisting of non-oxidized Cu and NiFe are also shown as open squares in Figure 27(a). The surface-oxidized Cu shows a linear increase in  $R_{xx}^{2\omega}$  with  $J_c$ , while  $R_{xx}^{2\omega}$  for non-oxidized Cu is negligible. The charge-to-spin conversion efficiencies evaluated from the slope in Figure 27(a) for surface-oxidized Cu is comparable to Pt as reported by An et al. [83], who demonstrated the AC- rather than the DC-spin current generation.

Figure 27(b) shows the USMR signals for surface-oxidized Cu layer covered with ferromagnetic NiFe as a function of oxygen exposure time, showing a peak at 6000 s. The oxidation is generally progressed by the nucleation of oxide island on surface followed by the diffusion of oxygen [94]. The width of the transition region of oxidation, therefore, increase with the diffusion, which leads to a decrease in the spin current produced via the SVC of current vorticity. If the spin current is attributed to the bulk or interfacial SOI of copper oxide, the amplitude should saturate according to the oxidation level as reported for uniformly oxidized Cu layer [84]. The peak of the USMR signal supports that the spin current is generated via SVC in the surface-oxidized Cu layer. The initial increase in the USMR signal for the exposure time below 6000 s may be attributed to an insufficient oxidation of the copper surface.

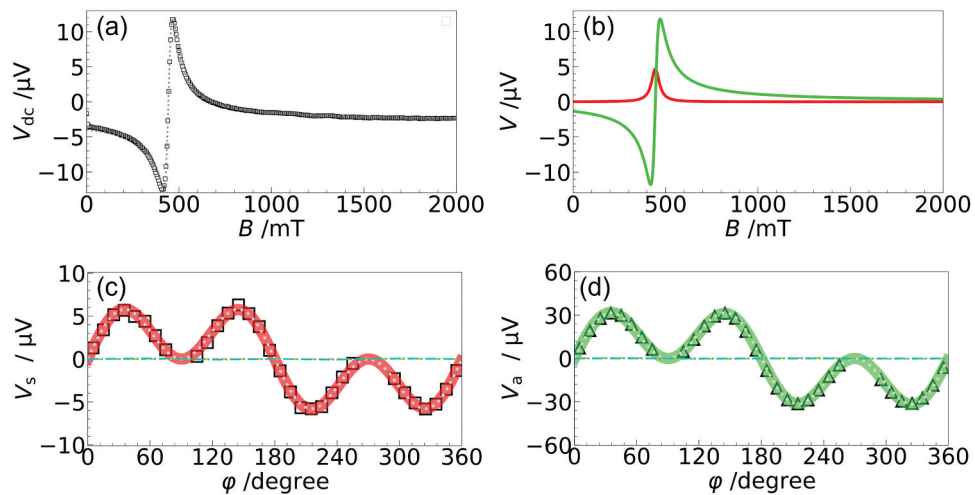
#### 4.3.2. Si/Al composition gradient materials [90]

The spin current generation efficiency for Si/Al composition gradient material was evaluated from the spin-torque efficiency  $\xi_{\text{FMR}}$  by means of the ST-FMR method using ferromagnetic Ni-Cu alloy, whose saturation magnetization  $M_s$  is lower than the commonly used ferromagnets such as NiFe and FeCo alloys. Such a low  $M_s$  ferromagnet is useful to improve the sensitivity for spin torque, whose magnitude is inversely proportional to  $M_s$ . Figures 28 (a) and (b), respectively, show the ST-FMR spectrum and its symmetric and anti-symmetric Lorentzian components for Si/Al composition gradient material with  $t_i$  of 0.5 nm. From the field angle dependence of the amplitudes of symmetric and antisymmetric Lorentzian components as shown in Figure 28 (c) and (d), respectively, it was confirmed that Si/Al gradient materials generate spin currents polarized in the same direction as that produced via the conventional spin Hall effect.

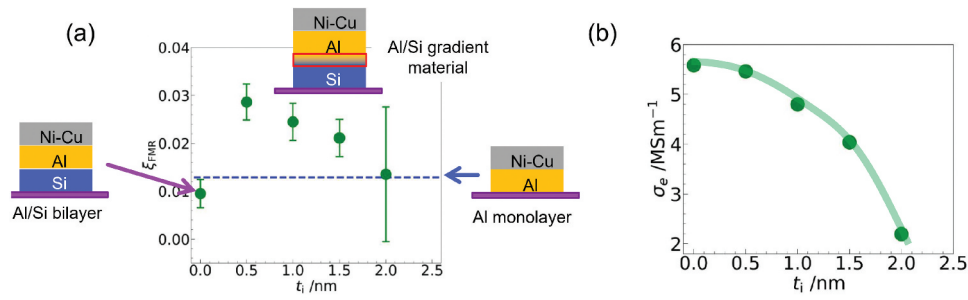
Figure 29(a) shows  $\xi_{\text{FMR}}$  for Si/Al composition gradient materials as a function of insertion layer thickness (i.e. Al/Si bilayer film thickness)  $t_i$ . Si/Al composition gradient materials with thinner insertion layer show larger spin-torque efficiency, although zero insertion does not increase  $\xi_{\text{FMR}}$  from the value for a single Al layer ( $\xi_{\text{FMR}} = 0.01$ ). The result indicates that steep Si/Al interfaces no longer contribute to spin current generation. For an insertion layer thickness of 0.5 nm, the efficiency reaches to half that of strong-SOI Pt ( $\xi_{\text{FMR}} = 0.06$ ). In contrast, as shown in Figure 29(b), the electrical conductivity for Si/Al composition gradient materials increases with decreasing the insertion layer thickness. Namely, unlike conventional strong-SOI materials such as Pt, Ta, and  $\beta$ -W, composition gradient materials can achieve both high efficiency of spin current generation and high electrical conductivity by decreasing the insertion layer thickness. For applications in spintronic devices such



**Figure 27.** (a) USMR signals for NiFe layer covered with surface-oxidized Cu layer (circles) as a function of electric current. Open squares are the results for control sample consisting of non-oxidized Cu and NiFe. (b) Air exposure time dependence of the USMR ratio for NiFe layer covered with surface-oxidized Cu layer. Preprinted from [82], copyright [2019, American Physical Society].



**Figure 28.** (a) Spin-torque FMR spectrum for bilayer film consisting of Ni-Cu alloy and Si/Al composition gradient material with  $t_f$  of 0.5 nm. (b) Symmetric and anti-symmetric Lorentzian components in (a). Amplitudes of symmetric and anti-symmetric Lorentzian component as a function of angles for in-plane magnetic field applications. Reproduced from [90].



**Figure 29.** (a) Spin-torque efficiency and (b) electrical conductivity as a function of insertion layer thickness  $t_i$  for Si/Al composition gradient materials. Reproduced from [90].

as MRAMs, it is crucial not only to generate large spin currents but also to minimize Joule loss by reducing electrical resistance. Therefore, further thinning of the nanoscale layer and improving its uniformity may significantly enhance both spin current generation efficiency and electrical conductivity. Utilizing epitaxial growth techniques for precise control over nanoscale layer structures could potentially improve the figure of merit, which is given by the product between spin Hall conductivity and electrical conductivity.

Additionally, results indicating an optimal insertion layer thickness for maximizing the spin torque efficiency are similar trend to those found in the oxidation time dependence of the efficiency of spin current generation in surface-oxidized copper film as shown in Figure 27(b). Both results are attributed to that the amount of spin accumulation due to current vorticity via SVC increases with narrowing the width of gradient in electrical conductivity, meanwhile excessively steep compositional changes diminish spin accumulation due to the current vorticity. When the length scale of the compositional gradient becomes sufficiently shorter than the mean free path of conduction electrons in the gradient regions, electron scattering due to the current vorticity may not occur, potentially resulting in the absence of SVC effects.

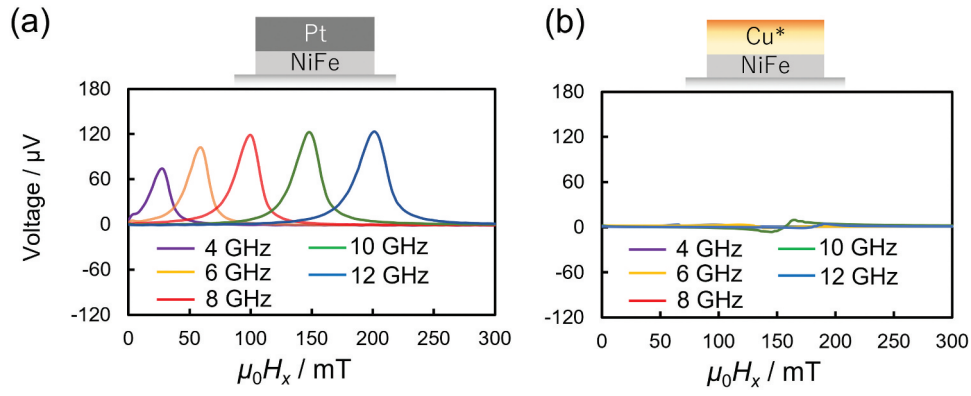
#### 4.4. Nonreciprocal spin current generation in composition gradient materials

To uncover the mechanisms underlying spin current generation in nano-scale gradient materials, it is helpful to understand the asymmetry (nonreciprocity) in efficiencies between charge-to-spin and spin-to-charge conversions. In the case of gyromagnetic effect using lattice rotation in SAWs, the reciprocity is demonstrated in ferromagnetic NiFe films by observing the phenomenon based on second-order interaction through the conversion from rotational motion to spin angular momentum (Barnett effect) and its inverse (Einstein-de Haas effect), validating

the reciprocity of gyromagnetic effects [64,73]. In contrast, experiments on composition gradient materials using surface-oxidized Cu film report the conversion from current vorticity (i.e. rotational motion of electrons) to spin current, while the reverse conversion does not occur [82]. To evaluate the efficiency of reciprocal conversion, i.e. spin-to-charge current conversion, the inverse spin-Hall effect due to DC spin current [95], whose injection is realized by the spin-pumping effect [96–98], has been measured. A microwave with an amplitude of 20 dBm and a frequency of 8 GHz was applied to generate an RF magnetic field to excite the FMR in ferromagnetic NiFe layer, which pumped a DC spin current into adjacent nonmagnetic layer. We can evaluate the spin-to-charge conversion efficiency of the nonmagnetic layer by measuring the Hall voltage due to the inverse SHE. Figures 30(a) and (b) show the Hall voltage  $V_{\text{ISHE}}$  as a function of the external magnetic field for bilayers with Pt and surface-oxidized Cu for the nonmagnetic layers, respectively [82]. From the peak amplitude ratio of  $V_{\text{ISHE}}$ , the spin-to-charge current conversion efficiency for surface-oxidized Cu is evaluated at only 5.6% of that for Pt, which is much lower than the charge-to-spin conversion efficiency ratio ( $\approx 71\%$ ). This value is almost the same as that obtained for non-oxidized Cu film ( $\approx 4.2\%$ ). Such a large asymmetry in the conversion efficiency suggests the existence of nonreciprocal mechanisms in the charge-to-spin conversion in the composition gradient materials.

Significant nonreciprocity in charge-to-spin current conversion has been observed in gradient materials other than copper oxides. Horaguchi et al. fabricated Si/Al composition gradient materials and found that the charge-to-spin current conversion efficiency was comparable to the value for Pt, although the inverse spin Hall voltage owing to the spin pumping was negligible [90]. Moreover, Nakayama et al. demonstrated that the linewidth of the ST-FMR spectrum for Ti/W composition gradient materials was independent of the CGI width, meanwhile the CGI-related variations in the spin-torque efficiency  $\xi_{\text{FMR}}$  show a local maximum at a particular CGI width [87].





**Figure 30.** Inverse spin Hall voltage for bilayers consisting of (a) NiFe/Pt and (b) NiFe/surface-oxidized Cu bilayers as a function of external magnetic field applied along the electric current. Microwave fields with frequencies in the range from 4 to 12 GHz were applied to pump spin current to the adjacent nonmagnetic layer. Preprinted from [82], copyright [2019, American Physical Society].

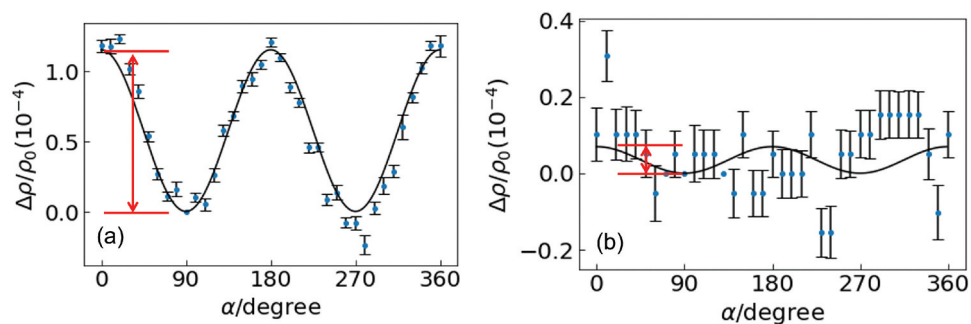
The spin Hall magnetoresistance effect (SMR) is one of the promising effects for demonstrating a second-order interaction consisting of both current-to-spin and spin-to-current conversions [99–102]. If the conversion between charge- and spin-currents is nonreciprocal regardless of the presence of current vorticity, the SMR no longer occurs. Zheng et al. observed the SMR in a bilayer film composed of surface-oxidized copper and ferromagnetic Fe [103], demonstrating both current-to-spin and spin-to-current conversion interactions. However, it has been also reported that the electric current flowing through the ferromagnetic layer causes another magneto-resistive effect similar to the SMR, e.g. anomalous Hall magnetoresistance effect [104,105]. To exclude the artifact due to the conductive ferromagnetic layer, it is crucial that the SMR effect is examined using a non-conducting ferromagnet, such as Yttrium Iron Garnet (YIG). Figures 31(a) and (b) illustrate the magnetic field angle dependencies of the SMR for bilayer films composed of Pt and surface-oxidized Cu, respectively, deposited on an insulating ferromagnetic YIG. In Pt/YIG, a sinusoidal variation with a period of  $\pi$  rad appears, meanwhile in surface-oxidized copper/YIG, an SMR of less than one-tenth of Pt is observed. It is noted that, in the SMR experiment, current vortices exist in the

surface-oxidized Cu layer. Namely, such a small SMR in surface-oxidized Cu film implies that the nonreciprocal current-spin conversion occurs regardless of the presence of current vorticity.

This strong nonreciprocity in current-to-spin conversion is a phenomenon commonly observed in gradient materials. Understanding its origin is therefore expected to lead to significant advancements in elucidating the spin current generation mechanisms in such systems, and this remains a key topic for future research.

#### 4.5. Contribution of spin-orbit interaction and structural disturbance in current-vorticity mediated gyromagnetic effects [87]

To examine the contribution of SOI in the gyromagnetic coupling between electron spin and current vorticity, we compared the sign of CGI-related change in spin-torque efficiency between Si/Al and Ti/W composition gradient materials. Si and Al show positive SOI, although Ti and W show negative SOI. If SOI contributes to the gyromagnetic coupling between current vortices and electron spins, spin current is generated in Ti/W sample with opposite polarity compared to Si/Al sample, which possesses positive SOI.



**Figure 31.** Spin Hall magnetoresistance for (a) YIG/Pt and (b) YIG/surface-oxidized Cu bilayers as a function of angle of in-plane magnetic field from the electric current direction.

Furthermore, in the gyromagnetic coupling with current vorticity, the spatial distribution of current density may significantly influence spin current generation characteristics. To investigate the effect of interfacial undulation on spin current generation, intentionally disrupted Ti/W gradient materials were fabricated by depositing them at high deposition rates, thereby structurally altering the gradient. Figures 32(a) and (b) show the surface morphology of Ti/W composition gradient materials fabricated by low-rate and high-rate sputtering conditions, respectively. Increasing the sputtering rates of Ti and W by factors of 4 and 2, respectively, resulted in a substantial increase in the root mean square roughness and peak-to-valley values of the gradient materials as seen in Figures 32(c) and (d). As observed in AFM images, numerous island-like structures originating from aggregation were formed.

Figure 32(e) depicts the insertion layer thickness dependence of spin-torque efficiency measured for samples with small surface undulations. The spin Hall effect in bulk  $\alpha$ -W with negative SOI induces negative spin-torque efficiency in Ti/W gradient materials. Conversely, similar to Si/Al gradient materials, spin-torque efficiency increases positively with decreasing insertion layer thickness and sharply decreases under conditions without an insertion layer. If emergent magnetic fields due to current vorticity reverse with SOI polarity, spin-torque efficiency must increase in opposite directions for Ti/W gradient materials compared to Si/Al gradient materials. Thus,

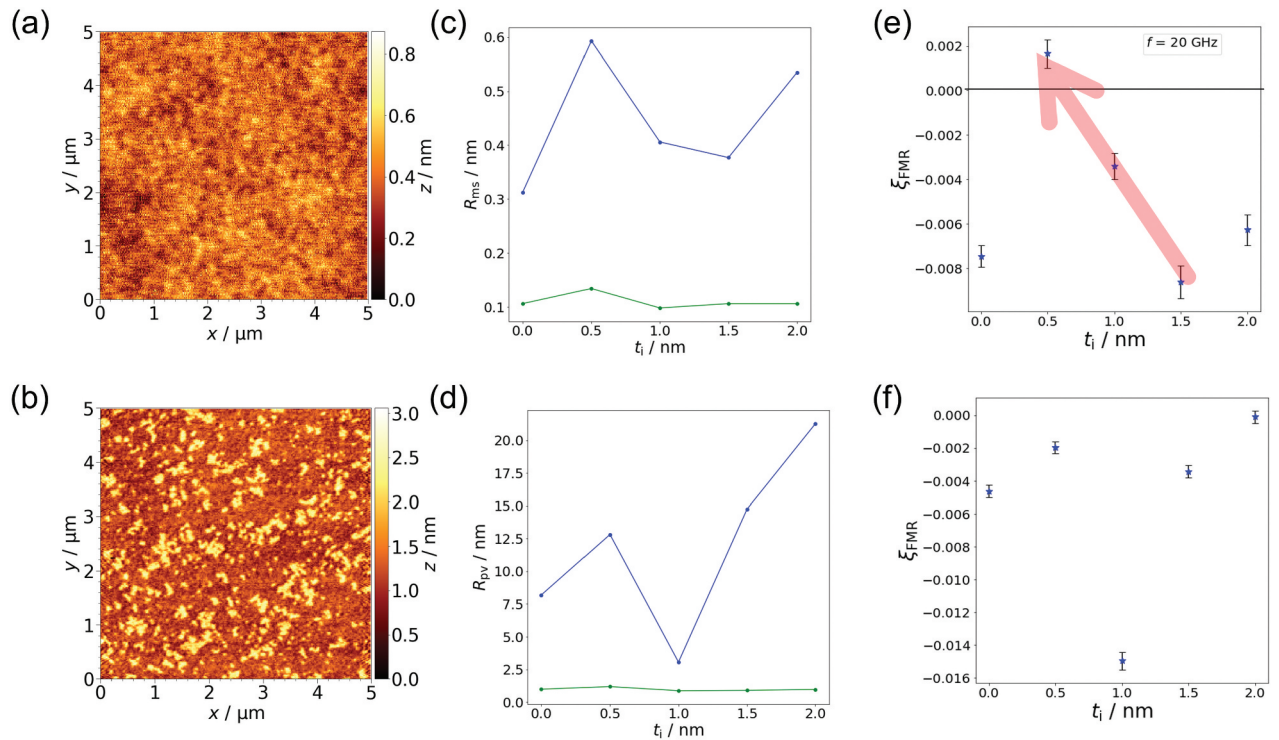
Figure 32(e) suggests that the coupling between current vorticity and electron spins via gyromagnetic effects does not depend on SOI polarity.

Figure 32(f) shows the insertion layer thickness dependence of spin-torque efficiency measured for samples with large surface undulations. Unlike the positive increase in spin-torque efficiency observed under low-rate deposition conditions, significant dispersion in spin-torque efficiency was observed, with no clear positive trend. These results suggest that interface flattening is crucial for spin current generation via current-vorticity gyromagnetic effects.

## 5. Unified discussions on the gyromagnetic effect

In this final section, we aim to provide a unified view of the acoustic and current-vorticity gyromagnetic effects from a materials science perspective, comparing them with the original gyromagnetic effect.

The gyromagnetic effect, as discussed in Section 3, is a universal angular momentum transfer phenomenon that occurs across an extremely broad frequency range from a few Hz to  $10^{21}$  Hz and has been observed in various systems. In spintronics, the acoustic and current-vorticity gyromagnetic effects, both of which employ nanoscale-engineered thin films, are key manifestations of this phenomenon.



**Figure 32.** Atomic force micrograph of Ti/ $\alpha$ -W composition gradient materials with  $t_i = 1.0$  nm fabricated by (a) low rate and (b) high rate sputtering. (c) Root mean square roughness  $R_{\text{rms}}$  and (d) peak to valley distance  $R_{\text{pv}}$  as a function of insertion layer thickness  $t_i$ . Blue and green dots indicate the data for samples prepared at high- and low-deposition rates, respectively. Spin-torque efficiency  $\xi_{\text{FMR}}$  for samples fabricated by (e) low rate and (f) high rate sputtering as a function of  $t_i$ . Preprinted from [87], copyright [2023, American Physical Society].

In the original gyromagnetic effect in ferromagnetic materials, magnetization is controlled through the rigid-body rotation of the material, which acts as an effective magnetic field. In contrast, the excitation of spin currents or spin waves in the acoustic and current-vorticity gyromagnetic effects requires two inputs: the spin polarization direction and the propagation direction of the flow. Rather than uniform rotation, these effects rely on spatially nonuniform rotation, or vorticity, marking an extension of the gyromagnetic effect from uniform to nonuniform motion.

The current-vorticity gyromagnetic effect has distinct features. While the original and acoustic gyromagnetic effects involve angular momentum transfer between electron spins and lattice rotation, the current-vorticity gyromagnetic effect does not involve lattice motion. Instead, it stems from the spatial nonuniformity of electric current specifically, the vorticity generated by the electron flow and its interaction with spins. This represents a closed system within the electron ensemble, where the system has no moving parts, marking a new class of gyromagnetic effect.

In the acoustic gyromagnetic effect, the lattice rotation creates an effective magnetic field that influences electron spins, while feedback from the spins generates mechanical torque on the lattice. This interaction allows for the tuning of both the lattices mechanical motion and the electron spins. In contrast, the current-vorticity gyromagnetic effect operates within a nonequilibrium electron many-body system, independent of lattice motion, relying on two-electron correlations (J. Fujimoto et al., in preparation). Here, spatially nonuniform many-body effects are controlled without mechanical components. Although condensed matter physics has developed extensive knowledge of electron many-body effects, most of this knowledge pertains to homogeneous materials, making the control of these effects in gradient materials a significant challenge for both fundamental physics and materials science.

By expanding the scope of gyromagnetic effects from uniform to nonuniform motion, from homogeneous to inhomogeneous materials, and from systems with moving parts to those without, the exploration of spintronics materials science using the gyromagnetic effect is just beginning. Even a century after its discovery, the gyromagnetic effect continues to inspire new research directions across various fields. We believe that our approach, rooted in materials science, will complement and drive further advancements in fundamental physics.

## 6. Summary

We reviewed recent advancements in applying gyromagnetic effects in solid-state devices, such as the excitation of spin waves and the generation of spin currents via lattice rotational motion of

SAWs and the orbital rotational motion of conduction electrons in compositionally graded materials. Spin waves generated by the spin-transfer torque, due to the gradient of the Barnett field, are significantly stronger than those directly induced by the Barnett field in magnetic materials. As theoretically predicted by Matsuo et al., the electrical conductivity, rather than the spin Hall angle of nonmagnetic materials, determines the spin current intensity. However, the observed spin current intensity difference between Cu and Pt is smaller than expected from their electrical conductivity, indicating another gyromagnetic effect mediated by SOI. Additionally, the frequency dependence of the spin current generation efficiency and the Barnett field confirms that higher frequencies enhance spin current generation. These findings, attributed to the non-uniformity of gyromagnetic effects, offer crucial insights for their application in spintronics devices.

While spin currents have been generated in metals with weak SOI using Rayleigh waves, these currents are alternating and nonuniform, unsuitable for magnetization switching devices. Conversely, previous studies on the gyromagnetic effect of vortical flow in liquid mercury have demonstrated DC spin currents generation, though liquid-metal devices applications are limited. To utilize gyromagnetic effects for magnetization switching in solids, static vorticity creation is necessary, achievable through the vorticity of currents acting as macroscopic fluids in solids. In mercury experiments, vorticity gradients were created via friction with the flow tube. In solids, as conduction electron drift velocity is proportional to local electrical conductivity, materials with a gradient in electrical conductivity are required.

Spin current generation in nanometer-thick composition gradients can occur without strong-SOI elements. Thinner composition gradients yield larger spin currents, whereas sharp interfaces do not. Furthermore, the gradient material does not convert spin-to-charge current, a nonreciprocity due to vortical flow of free electrons acting as a novel spin current source. Si/Al gradient materials can achieve less dissipative spin current circuits with higher electrical conductivity than strong-SOI materials.

Implementing gradient materials in MRAM requires generating large spin currents while minimizing signal attenuation and delay via reduced wiring resistance. The product of electrical conductivity and spin Hall conductivity for gradient materials with a 0.5 nm insertion layer is more than ten times that of Pt. This demonstrates the superiority of Si/Al gradient materials over



conventional spin current generation materials. Additionally, Si and Al used as low and high electrical conductivity materials, respectively, are abundant near the Earth's surface, unlike rare metals like Pt and W used in conventional MRAM. This makes them sustainable spintronics materials that require less energy and effort for resource procurement, contributing to reduced carbon dioxide emissions. We believe our results will pave the way for the development of a new field in gyro-spintronics material science.

## Acknowledgments

The authors thank D. Kobayashi, Y. Kurimune, G. Okano, S. Tateno, M. Okano, and A. Iwasaki of Keio University for their assistance with the experiments, K. Tang and T. Scheike of NIMS for their experimental support. The authors also thank T. Funato for theoretical discussions. This work was partly supported by JST CREST (Grant No. JPMJCR19J4), Grants-in-Aid for Scientific Research (Grant No. 24H00322, 24H02233, 23K26165, 23H01839, 22K13997, 21H04565), a JSPS KAKENHI Grant-in-Aid for Research Activity Start-up (Grant No. 22K20359), and the MEXT Quantum Leap Flagship Program (MEXT Q-LEAP) (Grant No. JPMXS0118067246). Part of this work was conducted at the AIST Nano-Processing Facility supported by the "Nanotechnology Platform Program" of the Ministry of Education, Culture, Sports, Science and Technology (MEXT), Japan (Grant No. JPMXP09-F-21-AT-0085).

## Disclosure statement

No potential conflict of interest was reported by the author(s).

## Funding

The work was supported by the Core Research for Evolutional Science and Technology [JPMJCR19J4]; Japan Society for the Promotion of Science [Grants-in-Aid for Scientific Research / 23H01839]; Japan Society for the Promotion of Science [Grants-in-Aid for Scientific Research / 21H04565]; Ministry of Education, Culture, Sports, Science and Technology [Quantum Leap Flagship Program / JPMXS0118067246]; Ministry of Education, Culture, Sports, Science and Technology [Nanotechnology Platform Program / JPMXP09-F-21-AT-0085]; Japan Society for the Promotion of Science [Grants-in-Aid for Scientific Research / 24H00322]; Japan Society for the Promotion of Science [Grants-in-Aid for Scientific Research / 24H02233]; Japan Society for the Promotion of Science [Grants-in-Aid for Scientific Research / 23K26165]; Japan Society for the Promotion of Science [Grants-in-Aid for Scientific Research / 22K13997]; Japan Society for the Promotion

of Science [Grant-in-Aid for Research Activity Start-up / 22K20359].

## Notes on contributors



**Yukio Nozaki** PhD, Professor in the Department of Physics, School of Science and Technology, Keio University. Graduated from the School of Science and Technology, Keio University in 1993 and obtained a PhD in Science from Keio University in 1998. Served as Assistant Professor (1998–2006) and Associate Professor (2006–2010) at the Graduate School and Faculty of Information Science and Electrical Engineering, Kyushu University. Since 2010, he has been with Keio University, first as an Associate Professor (2010–2016) and now as a Professor (2016–present). His research focuses on Magnetic Physics and Spintronics.



**Hiroaki Sukegawa**, Group Leader of the Spintronics Group at the Research Center for Magnetic and Spintronic Materials in the National Institute for Materials Science (NIMS). Obtained Ph.D. in Materials Science from Tohoku University in 2007. Served as a Researcher at NIMS in (2007–2014), Senior Researcher (2014–2018), Principal Researcher (2018–2023), and Group Leader (2023–present). His research interests include magnetic thin films and spintronics devices.



**Shinichi Watanabe**, PhD, Professor in the Department of Physics, School of Science and Technology, Keio University. Graduated from the Department of Physics at the University of Tokyo in 1997 and obtained a Doctor of Science degree from the University of Tokyo in 2002. Served as a Postdoctoral Fellow at the Swiss Federal Institute of Technology, Lausanne (2002–2004) and as a Research Associate in the Department of Physics, Faculty of Science, at the University of Tokyo (2004–2011). Since 2011, he has been with Keio University, first as an Associate Professor (2011–2019) and currently as a Professor (2019–present). His research focuses on optical spectroscopy in condensed matter physics.



**Seiji Yunoki**, Dr. Eng., Team Leader and Chief Scientist at RIKEN, Japan. He obtained his Doctor of Engineering from the Department of Applied Physics at Nagoya University, Japan, in 1996. He spent several years abroad, including time at the National High Magnetic Field Laboratory in the USA, Groningen University in the Netherlands, SISSA in Italy, and Oak Ridge National Laboratory in the USA, before joining RIKEN in 2008. His research focuses on condensed matter physics.





**Taisuke Horaguchi**, PhD, Assistant Professor in the Department of Applied Physics, Faculty of Science, Fukuoka University. Graduated from the School of Science and Technology, Keio University, in 2017, and earned a PhD in Science from the same university in 2022. From 2022 to 2024, served as a Project Assistant Professor at the School of Science and Technology, Keio University. Currently, he holds the position of Assistant Professor at Fukuoka University (2024–present). His research interests include Magnetic Physics and Spintronics.



**Hayato Nakayama**, graduated from the School of Science and Technology, Keio University in 2022 and obtained an M. S. of Science from Keio University in 2024. Apr. 2024 - current Keio University, Ph.D. course of Science, His research focuses on Magnetic Physics and Spintronics.



**Kazuto Yamanoi**, PhD, Assistant Professor in the Department of Physics, School of Science and Technology, Keio University. Graduated from the Faculty of Science, Fukuoka University in 2012 and obtained a PhD in Physics from Kyushu University in 2017. Postdoctoral Researcher (2018–2019) at the London centre for Nanotechnology, University College London. Since 2019, he has been with Keio University, now as an Assistant Professor (2019–present). His research focuses on Magnetic Physics and Spintronics.



**Zhenchao Wen**, PhD, Senior Researcher in the Research Center for Magnetic and Spintronic Materials, National Institute for Materials Science (NIMS). He received the B.S. degree in physics from Lanzhou University, China, in 2005, and M.S. and Ph.D. degrees in condensed matter physics from the Institute of Physics, Chinese Academy of Sciences, in 2007 and 2010, respectively. From 2010 to 2015, he was a Postdoctoral Researcher in NIMS. In 2015, he moved to the Institute for Materials Research, Tohoku University, as a Postdoctoral Researcher, and a specially appointed Assistant Professor, in 2016. From 2018, he joined NIMS as a Senior Researcher. His research interests include spintronics and magnetic materials, especially, magnetic tunnel junctions, Heusler alloys, and topological materials.



**Cong He**, Cong He received PhD in materials science and engineering at Chongqing University, China, in 2020. He was a postdoctoral researcher in NIMS, Japan, from 2020–2024. In June 2024, he joined Hunan University, China, and worked as an associate professor. His research interests include transmission electron microscopy, microstructure characterization of ultra-thin magnetic films and engineering alloys.



**Jieyuan Song**, PhD, Postdoctoral Researcher in the Research Center for Magnetic and Spintronic Materials, National Institute for Materials Science (NIMS). He received the B. S. degree in Space Science from Shandong University, China, in 2019, M.S. degree in Applied Physics and Ph.D. degree in Materials Science from the University of Tsukuba in 2021 and 2024, respectively. From 2024, he joined NIMS as a Postdoctoral Researcher. His research interests include spintronics and magnetic materials, especially, magnetic tunnel junctions, tunnel magnetoresistance, and spin-orbit torque devices.



**Tadakatsu Ohkubo**, Dr. T. Ohkubo is Deputy Director of the Research Center for Magnetic and Spintronic Materials at NIMS. He received his Ph.D. from Osaka University in 2001 on the microstructural characterization of amorphous alloys by electron microscopy. In 2002, he joined NIMS as a senior researcher for magnetic materials research. He became the leader of the Nanostructure Analysis Group in 2006. Then, he served in his current position since 2021. His expertise includes multiscale characterization of magnetic materials (permanent magnets, soft magnetic materials), spintronic devices, semiconductor devices, and structural materials by FIB-SEM, (S)TEM, and atom probe tomography.



**Seiji Mitani**, Managing Researcher of the Research Center for Magnetic and Spintronic Materials, NIMS. Obtained a PhD in Engineering from Nagoya University in 1993. Served as a Research Associate (1993–2001) and Associate Professor (2001–2008) at the Institute for Materials Research, Tohoku University. Since 2008, he has been with NIMS, as a Chief Researcher (2008–2009), Group Leader (2009–2023), and Director (2021–2024). He also has an adjunct position at University of Tsukuba (Professor 2010–present). His research focuses on magnetic nanostructures and spintronics.



**Kazuki Maezawa**, B. S., Graduate student in the Department of Physics, Faculty of Science and Technology, Keio University. Graduated from the Faculty of Science and Technology, Keio University in 2023 and obtained a B. S. degree. His research focuses on Spintronics and Optical physics.



**Daichi Nishikawa**, M.S., Researcher at the Access Service Systems Laboratory, Nippon Telegraph, and Telephone Corporation. Graduated from the School of Science and Technology, Keio University, in 2018. Obtained an M.S. in Science from Keio University and completed the Ph.D. coursework (without degree) at Keio University in 2024. Currently working as a researcher (2024–present). His research focuses on optical and spintronics technologies.



**Shun Fujii**, Shun Fujii received a B. S. degree in Electronics and Electrical Engineering from Keio University, Yokohama, Japan, in 2016, an M.S. degree in 2018, and a Ph.D. degree from the Faculty of Science and Technology, Keio University in 2020. After his Ph.D., he joined the Quantum Optoelectronics Research Team, RIKEN Center for Advanced Photonics, Japan, in October 2020. He has been an Assistant Professor with the Department of Physics, Faculty of Science and Technology, Keio University since September 2022. His research interests include ultrafast lasers and nonlinear optics and their applications in micro- and nano-scale structures such as high-Q microresonator technologies.



**Mamoru Matsuo**, PhD, Associate Professor at the Kavli Institute for Theoretical Sciences, University of Chinese Academy of Sciences (2018-present). He received a Ph.D. in Science from the University of Tokyo in 2008. He held positions at KEK, Tohoku University, and Kyoto University before joining the Japan Atomic Energy Agency (2012–2017) and Tohoku University (2017–2018). His research focuses on spintronics, particularly spin transport driven by the gyromagnetic effect.



**Junji Fujimoto**, Dr. Sci., Assistant Professor in the Department of Electrical Engineering, Electronics, and Applied Physics, Saitama University, Japan. Graduated from the Department of Materials Engineering Science, Graduate School of Engineering Science, Osaka University, Japan, and obtained a Doctor of Science from Osaka University in 2015. His research field is condensed matter physics, particularly spintronics.



**Sadamichi Maekawa**, Visiting Senior Fellow at RIKEN Center for Emergent Matter Science. Obtained Dr. Sci., at Tohoku University in 1975. He is also Visiting Chair Professor at Kavli Institute for Theoretical Sciences of University of Chinese Academy of Sciences (Beijing), Professor Emeritus at Tohoku University, and a member of Advisory Board of Honda Memorial Foundation, Institute for Electro-Magnetic Materials and Advanced Technology Institute. His research focuses on condensed matter theory, especially, spintronics and superconductivity.

## ORCID

Yukio Nozaki <http://orcid.org/0000-0002-7262-0124>  
 Hiroaki Sukegawa <http://orcid.org/0000-0002-4034-7848>  
 Shinichi Watanabe <http://orcid.org/0000-0003-4116-0679>  
 Taisuke Horaguchi <http://orcid.org/0009-0000-7435-6075>  
 Hayato Nakayama <http://orcid.org/0009-0006-0510-2454>

Kazuto Yamanoi <http://orcid.org/0000-0001-5356-0712>  
 Zhenchao Wen <http://orcid.org/0000-0001-7496-1339>  
 Cong He <http://orcid.org/0000-0002-7548-9344>  
 Jieyuan Song <http://orcid.org/0000-0001-6846-2875>  
 Tadakatsu Ohkubo <http://orcid.org/0000-0003-3548-1951>  
 Seiji Mitani <http://orcid.org/0000-0002-1348-0774>  
 Kazuki Maezawa <http://orcid.org/0009-0009-0549-914X>  
 Daichi Nishikawa <http://orcid.org/0009-0000-4557-9296>  
 Shun Fujii <http://orcid.org/0000-0002-0998-366X>  
 Mamoru Matsuo <http://orcid.org/0000-0003-1303-7614>  
 Junji Fujimoto <http://orcid.org/0000-0002-5669-1299>  
 Sadamichi Maekawa <http://orcid.org/0000-0002-4237-7741>

## References

- [1] Moore GE. Cramming more components onto integrated circuits. *Electronics*. 1965;38(8):114–117. doi:10.1109/JPROC.1998.658762
- [2] Slonczewski JC. Current-driven excitation of magnetic multilayers. *J Magn Magn Mater*. 1996;159(1): L1–L7. doi:10.1016/0304-8853(96)00062-5
- [3] Berger L. Emission of spin waves by a magnetic multilayer traversed by a current. *Phys Rev B*. 1996;54(13):9353–9358. doi:10.1103/PhysRevB.54.9353
- [4] Stiles MD, Zangwill A. Anatomy of spin-transfer torque. *Phys Rev B*. 2002;66(1):014407. doi:10.1103/PhysRevB.66.014407
- [5] Manchon A, Zhang S. Theory of nonequilibrium intrinsic spin torque in a single nanomagnet. *Phys Rev B*. 2008;78(21):212405. doi:10.1103/PhysRevB.78.212405
- [6] Manchon A, Zhang S. Theory of spin torque due to spin-orbit coupling. *Phys Rev B*. 2009;79(9):094422. doi:10.1103/PhysRevB.79.094422
- [7] Miron IM, Gaudin G, Auffret S, et al. Current-driven spin torque induced by the Rashba effect in a ferromagnetic metal layer. *Nat Mater*. 2010;9(3):230–234. doi:10.1038/nmat2613
- [8] Miron IM, Garello K, Gaudin G, et al. Perpendicular switching of a single ferromagnetic layer induced by in-plane current injection. *Nature*. 2011;476(7359):189–193. doi:10.1038/nature10309
- [9] Liu L, Pai CF, Li Y, et al. Spin-torque switching with the giant spin Hall effect of tantalum. *Science*. 2012;336(6081):555–558. doi:10.1126/science.1218197
- [10] Hosomi M, Yamagishi H, Yamamoto T, et al. A novel nonvolatile memory with spin torque transfer magnetization switching: spin-RAM. In: IEEE International Electron Devices Meeting, 2005. IEDM Technical Digest, Washington, DC. IEEE; 2005. p. 459. <https://cir.nii.ac.jp/crid/1363951794575226752>
- [11] Kawahara T, Takemura R, Miura K, et al. 2MB spin-transfer torque RAM (SPRAM) with bit-by-bit bidirectional current write and parallelizing-direction current read. In: 2007 IEEE International Solid-State Circuits Conference. Digest of Technical Papers, San Francisco, CA; 2007. p. 480–617.
- [12] Beach R, Min T, Horng C, et al. A statistical study of magnetic tunnel junctions for high-density spin torque transfer-MRAM (STT-MRAM). In: 2008 IEEE International Electron Devices Meeting, San Francisco, CA; 2008. p. 1–4.



- [13] Kishi T, Yoda H, Kai T, et al. Lower-current and fast switching of a perpendicular TMR for high speed and high density spin-transfer-torque MRAM. In: 2008 IEEE International Electron Devices Meeting, San Francisco, CA; 2008. p. 1–4.
- [14] Chung S, Rho KM, Kim SD, et al. Fully integrated 54nm STT-MRAM with the smallest bit cell dimension for high density memory application. In: 2010 International Electron Devices Meeting, San Francisco, CA; 2010. p.12.7.1–12.7.4.
- [15] Worledge DC, Hu G, Trouilloud PL, et al. Switching distributions and write reliability of perpendicular spin torque MRAM. In: 2010 International Electron Devices Meeting, San Francisco, CA; 2010. p.12.5.1–12.5.4.
- [16] Kim W, Jeong JH, Kim Y, et al. Extended scalability of perpendicular STT-MRAM towards sub-20nm MTJ node. In: 2011 International Electron Devices Meeting, Washington, DC; 2011. p.24.1.1–24.1.4.
- [17] Rizzo ND, Houssameddine D, Janesky J, et al. A fully functional 64 MB DDR3 ST-MRAM built on 90 nm CMOS technology. IEEE Trans Magn. 2013;49(7):4441–4446. doi:10.1109/TMAG.2013.2243133
- [18] Kobayashi D, Yoshikawa T, Matsuo M, et al. Spin current generation using a surface acoustic wave generated via spin-rotation coupling. Phys Rev Lett. 2017;119(7):077202. doi:10.1103/PhysRevLett.119.077202
- [19] Kurimune Y, Matsuo M, Maekawa S, et al. Highly nonlinear frequency-dependent spin-wave resonance excited via spin-vorticity coupling. Phys Rev B. 2020;102(17):174413. doi:10.1103/PhysRevB.102.174413
- [20] Matsuo M, Ieda J, Harii K, et al. Mechanical generation of spin current by spin-rotation coupling. Phys Rev B. 2013;87(18):180402. doi:10.1103/PhysRevB.87.180402
- [21] Richardson OW. A mechanical effect accompanying magnetization. Phys Rev (Series I). 1908;26(3):248–253. doi:10.1103/PhysRevSeriesI.26.248
- [22] Einstein A. Experimenteller nachweis der ampèreschen molekularströme. Naturwissenschaften. 1915;3(19):237–238. doi:10.1007/BF01546392
- [23] Einstein A, de Haas WJ. Experimental proof of the existence of Ampere's molecular currents. In: Koninklijke Nederlandsche Akademie van Wetenschappen Proceedings, Amsterdam, Netherlands; 1915. Vol. 18(1):696–711.
- [24] Barnett SJ. On magnetization by angular acceleration. Science. 1909;30(769):413. doi:10.1126/science.30.769.413.a
- [25] Barnett SJ. Magnetization by rotation. Phys Rev. 1915;6(4):239–270. doi:10.1103/PhysRev.6.239
- [26] Mashhoon B. Neutron interferometry in a rotating frame of reference. Phys Rev Lett. 1988;61(23):2639–2642. doi:10.1103/PhysRevLett.61.2639
- [27] Hehl FW, Ni WT. Inertial effects of a Dirac particle. Phys Rev D. 1990;42(6):2045–2048. doi:10.1103/PhysRevD.42.2045
- [28] Wallis TM, Moreland J, Kabos P. Einstein–de Haas effect in a NiFe film deposited on a microcantilever. Appl Phys Lett. 2006 09;89(12):122502. doi:10.1063/1.2355445
- [29] Zolfagharkhani G, Gaidarzhy A, Degiovanni P, et al. Nanomechanical detection of itinerant electron spin flip. Nat Nanotechnol. 2008;3(12):720–723. doi:10.1038/nnano.2008.311
- [30] Matsuo M, Ieda J, Saitoh E, et al. Effects of mechanical rotation on spin currents. Phys Rev Lett. 2011;106(7):076601. doi:10.1103/PhysRevLett.106.076601
- [31] Matsuo M, Ieda J, Saitoh E, et al. Spin current generation due to mechanical rotation in the presence of impurity scattering. Appl Phys Lett. 2011;98(24):242501. doi:10.1063/1.3597220
- [32] Matsuo M, Ieda J, Saitoh E, et al. Spin-dependent inertial force and spin current in accelerating systems. Phys Rev B. 2011;84(10):104410. doi:10.1103/PhysRevB.84.104410
- [33] Hirohata A, Baba Y, Murphy BA, et al. Magneto-optical detection of spin accumulation under the influence of mechanical rotation. Sci Rep. 2018;8(1):1974. doi:10.1038/s41598-018-20269-5
- [34] Matsuo M, Ohnuma Y, Maekawa S. Theory of spin hydrodynamic generation. Phys Rev B. 2017;96(2):020401. doi:10.1103/PhysRevB.96.020401
- [35] Takahashi R, Matsuo M, Ono M, et al. Spin hydrodynamic generation. Nat Phys. 2016;12(1):52–56. doi:10.1038/nphys3526
- [36] Takahashi R, Chudo H, Matsuo M, et al. Giant spin hydrodynamic generation in laminar flow. Nat Commun. 2020;11(1):3009. doi:10.1038/s41467-020-16753-0
- [37] Tabaei Kazerooni H, Thieme A, Schumacher J, et al. Electron spin-vorticity coupling in pipe flows at low and high Reynolds number. Phys Rev Appl. 2020;14(1):014002. doi:10.1103/PhysRevApplied.14.014002
- [38] Tokoro M, Takahashi R. Spin hydrodynamic generation in low-melting-point pure metal. Phys Rev Appl. 2022;17(6):L061003. doi:10.1103/PhysRevApplied.17.L061003
- [39] Adamczyk L, Adkins JK, Agakishiev G, et al. Global hyperon polarization in nuclear collisions. Nature. 2017;548(7665):62–65. doi:10.1038/nature23004
- [40] Landau LD, Lifshitz EM. Theory of elasticity. 3rd ed. London (UK): Pergamon Press; 1986.
- [41] Cleland AN. Foundations of nanomechanics: from solid-state theory to device applications. 1st ed. Springer Adv Texts In Phys; 2002. doi:10.1007/978-3-662-05287-7 Berlin, Heidelberg.
- [42] Nozaki Y. Acoustic gyromagnetic effect. JSAP Rev. 2023;2023:230203. doi:10.11470/jsaprev.230203
- [43] Chen C, Han L, Liu P, et al. Direct-current electrical detection of surface-acoustic-wave-driven ferromagnetic resonance. Adv Mater. 2023;35(38):2302454. doi:10.1002/adma.202302454
- [44] Sogawa T, Santos PV, Zhang SK, et al. Transport and lifetime enhancement of photoexcited spins in GaAs by surface acoustic waves. Phys Rev Lett. 2001;87(27):276601. doi:10.1103/PhysRevLett.87.276601
- [45] Sanada H, Sogawa T, Gotoh H, et al. Acoustically induced spin-orbit interactions revealed by two-dimensional imaging of spin transport in GaAs. Phys Rev Lett. 2011;106(21):216602. doi:10.1103/PhysRevLett.106.216602
- [46] Sogawa T, Sanada H, Gotoh H, et al. Spatially modulated photoluminescence properties in dynamically strained GaAs/AlAs quantum wells by surface acoustic wave. Appl Phys Lett. 2012;100(16):162109. doi:10.1063/1.3703309
- [47] Sogawa T, Sanada H, Gotoh H, et al. Dynamic control of photoluminescence polarization properties in GaAs/AlAs quantum wells by surface acoustic waves. Phys Rev B. 2012;86(3):035311. doi:10.1103/PhysRevB.86.035311

- [48] Sanada H, Kunihashi Y, Gotoh H, et al. Manipulation of mobile spin coherence using magnetic-field-free electron spin resonance. *Nat Phys.* 2013;9(5):280–283. doi:10.1038/nphys2573
- [49] Yamanouchi K, Sakurai N, Satoh T. SAW propagation characteristics and fabrication technology of piezoelectric thin film/diamond structure. In: *Proceedings. IEEE Ultrasonics Symposium, Montreal, Canada; 1989. Vol. 1. p. 351–354.*
- [50] Fujii S, Yamada H, Omori T, et al. One-port SAW resonators fabricated on single-crystal diamond. In: 2013 IEEE MTT-S International Microwave Symposium Digest (MTT), Seattle, WA; 2013. p. 1–3.
- [51] Iwasaki A, Nishikawa D, Okano M, et al. Temporal-offset dual-comb vibrometer with picometer axial precision. *APL Photonics.* 2022;7(10):106101. doi:10.1063/5.0099155
- [52] Tateno S, Nozaki Y. Highly nonreciprocal spin waves excited by magnetoelastic coupling in a Ni/Si bilayer. *Phys Rev Appl.* 2020;13:034074. doi:10.1103/PhysRevApplied.13.034074
- [53] Weiler M, Dreher L, Heeg C, et al. Elastically driven ferromagnetic resonance in nickel thin films. *Phys Rev Lett.* 2011;106(11):117601. doi: 10.1103/PhysRevLett.106.117601
- [54] Weiler M, Huebl H, Goerg FS, et al. Spin pumping with coherent elastic waves. *Phys Rev Lett.* 2012;108(17):176601. doi:10.1103/PhysRevLett.108.176601
- [55] Dreher L, Weiler M, Pernpeintner M, et al. Surface acoustic wave driven ferromagnetic resonance in nickel thin films: theory and experiment. *Phys Rev B.* 2012;86(13):134415. doi:10.1103/PhysRevB.86.134415
- [56] Gowtham PG, Moriyama T, Ralph DC, et al. Traveling surface spin-wave resonance spectroscopy using surface acoustic waves. *J Appl Phys.* 2015;118(23):233910. doi:10.1063/1.4938390
- [57] Labanowski D, Jung A, Salahuddin S. Power absorption in acoustically driven ferromagnetic resonance. *Appl Phys Lett.* 2016;108(2):022905. doi:10.1063/1.4939914
- [58] Xu M, Puebla J, Auvray F, et al. Inverse Edelstein effect induced by magnon-phonon coupling. *Phys Rev B.* 2018;97(18):180301. doi:10.1103/PhysRevB.97.180301
- [59] Sasaki R, Nii Y, Iguchi Y, et al. Nonreciprocal propagation of surface acoustic wave Ni / LiNbO<sub>3</sub>. *Phys Rev B.* 2017;95(2):020407. doi:10.1103/PhysRevB.95.020407
- [60] Verba R, Lisenkov I, Krivorotov I, et al. Nonreciprocal surface acoustic waves in multilayers with magnetoelastic and interfacial Dzyaloshinskii-Moriya interactions. *Phys Rev Appl.* 2018;9(6):064014. doi:10.1103/PhysRevApplied.9.064014
- [61] Verba R, Tiberkevich V, Slavin A. Wide-band non-reciprocity of surface acoustic waves induced by magnetoelastic coupling with a synthetic antiferromagnet. *Phys Rev Appl.* 2019;12(5):054061. doi:10.1103/PhysRevApplied.12.054061
- [62] Walowski J, Kaufmann MD, Lenk B, et al. Intrinsic and non-local Gilbert damping in polycrystalline nickel studied by Ti: sapphire laser fs spectroscopy. *J Phys D: Appl Phys.* 2008;41(16):164016. doi:10.1088/0022-3727/41/16/164016
- [63] Ma M, Chen C, Xu H, et al. Enhanced radiation efficiency by resonant coupling in a large bandwidth magnetoelectric antenna. *Adv Funct Mater.* 2024;34(48):2408699. doi:10.1002/adfm.202408699
- [64] Kurimune Y, Matsuo M, Nozaki Y. Observation of gyromagnetic spin wave resonance in NiFe films. *Phys Rev Lett.* 2020;124(21):217205. doi:10.1103/PhysRevLett.124.217205
- [65] Lan J, Yu W, Wu R, et al. Spin-wave diode. *Phys Rev X.* 2015;5(4):041049. doi:10.1103/PhysRevX.5.041049
- [66] Maezawa K, Fujii S, Yamanoi K, et al. Optical profiling of surface-acoustic-wave absorption due to elastically driven ferromagnetic resonance in nickel. In: 2023 IEEE International Magnetic Conference - Short Papers (INTERMAG Short Papers), Sendai, Japan; 2024. p. 1–2.
- [67] Maezawa K, Fujii S, Yamanoi K, et al. Spatiotemporal visualization of a surface acoustic wave coupled to magnons across a submillimeter-long sample by pulsed laser interferometry. *Phys Rev Appl.* 2024;21(4):044047. doi: 10.1103/PhysRevApplied.21.044047
- [68] Shao L, Gokhale VJ, Peng B, et al. Femtometer-amplitude imaging of coherent super high frequency vibrations in micromechanical resonators. *Nat Commun.* 2022;13(1):694. doi: 10.1038/s41467-022-28223-w
- [69] Casals B, Statuto N, Foerster M, et al. Generation and imaging of magnetoacoustic waves over millimeter distances. *Phys Rev Lett.* 2020;124(13):137202. doi: 10.1103/PhysRevLett.124.137202
- [70] Zhao CB, Zhang ZZ, Li Y, et al. Direct imaging of resonant phonon-magnon coupling. *Phys Rev Appl.* 2021;15(1):014052. doi: 10.1103/PhysRevApplied.15.014052
- [71] Stamm C, Murer C, Berritta M, et al. Magneto-optical detection of the spin Hall effect in Pt and W thin films. *Phys Rev Lett.* 2017;119(8):087203. doi:10.1103/PhysRevLett.119.087203
- [72] Ortiz VH, Coh S, Wilson RB. Magneto-optical Kerr spectra of gold induced by spin accumulation. *Phys Rev B.* 2022;106(1):014410. doi:10.1103/PhysRevB.106.014410
- [73] Tateno S, Kurimune Y, Matsuo M, et al. Einstein–de Haas phase shifts in surface acoustic waves. *Phys Rev B.* 2021;104(2):L020404. doi:10.1103/PhysRevB.104.L020404
- [74] Tateno S, Okano G, Matsuo M, et al. Electrical evaluation of the alternating spin current generated via spin-vorticity coupling. *Phys Rev B.* 2020;102(10):104406. doi:10.1103/PhysRevB.102.104406
- [75] Ando K, Takahashi S, Ieda J, et al. Inverse spin-Hall effect induced by spin pumping in metallic system. *J Appl Phys.* 2011;109(10):103913. doi:10.1063/1.3587173
- [76] Matsuo M, Bandurin DA, Ohnuma Y, et al. Spin hydrodynamic generation in graphene; 2020. Available from: <https://arxiv.org/abs/2005.01493>
- [77] Lange F, Ejima S, Fujimoto J, et al. Generation of current vortex by spin current in Rashba systems. *Phys Rev Lett.* 2021;126(15):157202. doi:10.1103/PhysRevLett.126.157202
- [78] Fujimoto J, Lange F, Ejima S, et al. Spin-charge conversion and current vortex in spin-orbit coupled systems. *APL Mater.* 2021;9(6):060904. doi:10.1063/5.0049882
- [79] Fujimoto J, Koshibae W, Matsuo M, et al. Zeeman coupling and Dzyaloshinskii-Moriya interaction driven by electric current vorticity. *Phys Rev B.* 2021;103(22):L220402. doi:10.1103/PhysRevB.103.L220402
- [80] Yu XZ, Morikawa D, Nakajima K, et al. Motion tracking of 80-nm-size skyrmions upon directional



- current injections. *Sci Adv.* **2020**;6(25):eaaz9744. doi:10.1126/sciadv.aaz9744.
- [81] Masudome H, Abe H. Chemical depth profiling of copper oxide film by ToF-SIMS using  $\text{Bi}_3^{++}$  cluster. *Surf & Interface Anal.* **2011**;43(1–2):664–668. doi:10.1002/sia.3504
- [82] Okano G, Matsuo M, Ohnuma Y, et al. Nonreciprocal spin current generation in surface-oxidized copper films. *Phys Rev Lett.* **2019**;122(21):217701. doi:10.1103/PhysRevLett.122.217701.
- [83] An H, Kageyama Y, Kanno Y, et al. Spin-torque generator engineered by natural oxidation of Cu. *Nat Commun.* **2016**;7(1):13069. doi:10.1038/ncomms13069
- [84] Gao T, Qaiumzadeh A, An H, et al. Intrinsic spin-orbit torque arising from the Berry curvature in a metallic-magnet/Cu-oxide interface. *Phys Rev Lett.* **2018**;121(1):017202. doi:10.1103/PhysRevLett.121.017202
- [85] Haku S, Musha A, Gao T, et al. Role of interfacial oxidation in the generation of spin-orbit torques. *Phys Rev B.* **2020**;102(2):024405. doi:10.1103/PhysRevB.102.024405
- [86] Go D, Jo D, Gao T, et al. Orbital Rashba effect in a surface-oxidized Cu film. *Phys Rev B.* **2021**;103(12):L121113. doi:10.1103/PhysRevB.103.L121113
- [87] Nakayama H, Horaguchi T, He C, et al. Spin-torque generation using a compositional gradient at the interface between titanium and tungsten thin films. *Phys Rev B.* **2023**;107(17):174416. doi:10.1103/PhysRevB.107.174416
- [88] Murray JL. The Ti-W (titanium-tungsten) system. *Bull Of Alloy Phase Diagrams.* **1981**;2(2):192–196. doi:10.1007/BF02881477
- [89] Murray JL, McAlister AJ. The Al-Si (aluminum-silicon) system. *Bull Of Alloy Phase Diagrams.* **1984**;5(1):74–84. doi:10.1007/BF02868729
- [90] Horaguchi T, He C, Wen Z, et al. Nanometre-thick Si/Al gradient materials for sustainable spin current generation. *Res Square.* **2021** nov;PREPRINT (Version 1); doi:10.21203/rs.3.rs-955888/v1
- [91] Massara R, Feschotte P. Le système binaire Pt-Si. *J Alloys And Compd.* **1993**;201(1):223–227. doi:10.1016/0925-8388(93)90888-T
- [92] Song J, He C, Scheike T, et al. Charge-to-spin conversion in fully epitaxial Ru/Cu hybrid nanolayers with interface control. *Nanotechnology.* **2023**;34(36):365704. doi:10.1088/1361-6528/acda36
- [93] Tang K, He C, Wen Z, et al. Enhanced orbital torque efficiency in nonequilibrium Ru50Mo50(0001) alloy epitaxial thin films. *APL Mater.* **2024**;12(3):031131. doi:10.1063/5.0195775
- [94] Gattinoni C, Michaelides A. Atomistic details of oxide surfaces and surface oxidation: the example of copper and its oxides. *Surf Sci Rep.* **2015**;70(3):424–447. doi:10.1016/j.surfrep.2015.07.001
- [95] Saitoh E, Ueda M, Miyajima H, et al. Conversion of spin current into charge current at room temperature: inverse spin-Hall effect. *Appl Phys Lett.* **2006**;88(18):182509. doi:10.1063/1.2199473
- [96] Silsbee RH, Janossy A, Monod P. Coupling between ferromagnetic and conduction-spin-resonance modes at a ferromagnetic—normal-metal interface. *Phys Rev B.* **1979**;19(9):4382–4399. doi:10.1103/PhysRevB.19.4382
- [97] Mizukami S, Ando Y, Miyazaki T. Effect of spin diffusion on Gilbert damping for a very thin permalloy layer in Cu/permalloy/Cu/Pt films. *Phys Rev B.* **2002**;66(10):104413. doi:10.1103/PhysRevB.66.104413
- [98] Tserkovnyak Y, Brataas A, Bauer GEW. Enhanced Gilbert damping in thin ferromagnetic films. *Phys Rev Lett.* **2002**;88(11):117601. doi:10.1103/PhysRevLett.88.117601
- [99] Huang SY, Fan X, Qu D, et al. Transport magnetic proximity effects in platinum. *Phys Rev Lett.* **2012**;109(10):107204. doi:10.1103/PhysRevLett.109.107204
- [100] Nakayama H, Althammer M, Chen YT, et al. Spin Hall magnetoresistance induced by a nonequilibrium proximity effect. *Phys Rev Lett.* **2013**;110(20):206601. doi:10.1103/PhysRevLett.110.206601
- [101] Althammer M, Meyer S, Nakayama H, et al. Quantitative study of the spin Hall magnetoresistance in ferromagnetic insulator/normal metal hybrids. *Phys Rev B.* **2013**;87(22):224401. doi:10.1103/PhysRevB.87.224401
- [102] Chen YT, Takahashi S, Nakayama H, et al. Theory of spin Hall magnetoresistance. *Phys Rev B.* **2013**;87(14):144411. doi:10.1103/PhysRevB.87.144411
- [103] Zheng S, Meng K, Liu Q, et al. Origin of large spin Hall magnetoresistance in Fe/CuO<sub>x</sub> bilayers. *Phys Lett A.* **2020**;384(9):126198. doi:10.1016/j.physleta.2019.126198
- [104] Taniguchi T. Magnetoresistance generated from charge-spin conversion by anomalous Hall effect in metallic ferromagnetic/nonmagnetic bilayers. *Phys Rev B.* **2016**;94(17):174440. doi:10.1103/PhysRevB.94.174440
- [105] Yang Y, Luo Z, Wu H, et al. Anomalous Hall magnetoresistance in a ferromagnet. *Nat Commun.* **2018**;9(1):2255. doi:10.1038/s41467-018-04712-9
- [106] Harder M, Gui Y, Hu CM. Electrical detection of magnetization dynamics via spin rectification effects. *Phys Rep.* **2016**;661:1–59. doi:10.1016/j.physrep.2016.10.002
- [107] Horaguchi T, Matsuo M, Nozaki Y. Highly accurate evaluation of spin-torque efficiency by measuring in-plane angular dependence of spin-torque ferromagnetic resonance. *J Magn Magn Mater.* **2020**;505:166727. doi:10.1016/j.jmmm.2020.166727
- [108] Avci CO, Garelo K, Ghosh A, et al. Unidirectional spin Hall magnetoresistance in ferromagnet/normal metal bilayers. *Nat Phys.* **2015**;11(7):570–575. doi:10.1038/nphys3356
- [109] Avci CO, Mendil J, Beach GSD, et al. Origins of the unidirectional spin Hall magnetoresistance in metallic bilayers. *Phys Rev Lett.* **2018**;121(8):087207. doi:10.1103/PhysRevLett.121.087207
- [110] Borisenko D IV, Urazhdin VE, S, et al. Relation between unidirectional spin Hall magnetoresistance and spin current-driven magnon generation. *Appl Phys Lett.* **2018**;113(6):062403. doi:10.1063/1.5044737
- [111] Zhang SSL, Vignale G. Theory of unidirectional spin Hall magnetoresistance in heavy-metal/ferromagnetic-metal bilayers. *Phys Rev B.* **2016**;94(14):140411. doi:10.1103/PhysRevB.94.140411
- [112] Kim KJ, Li T, Kim S, et al. Possible contribution of high-energy magnons to unidirectional magnetoresistance in metallic bilayers. *Appl Phys Express.* **2019**;12(6):063001. doi:10.7567/1882-0786/ab1b54
- [113] Bohland Filho J, Kuhnen CA. Electronic and magnetic structure of ordered Fe-Ni alloys. *Brazilian J. Phys.* **1993**;23(3):288–298.
- [114] Meservey R, Tedrow P. Spin-polarized electron tunneling. *Phys Rep.* **1994**;238(4):173–243. doi:10.1016/0370-1573(94)90105-8

## Appendices

### Appendix A. Evaluation methods for spin-torque efficiency in gradient materials

In this Appendix, we introduce two representative methods applicable for evaluating spin-torque efficiency in gradient materials, along with their measurement examples.

#### A.1 Spin-torque (ST) FMR method

Figure A1(a) shows a schematic setup for spin-torque ferromagnetic resonance (ST-FMR) measurement. An alternating current (AC) with a frequency  $f$  ( $= \omega/2\pi$ ) is applied from a signal generator (SG) to a non-magnetic/ferromagnetic bilayer strip, which is embedded in an electrically shorted coplanar waveguide (CPW). The AC current in the non-magnetic layer produces not only AC spin current via spin Hall effect but also AC Oersted field  $h_{Oe}$ , both of which produce AC magnetic torque on the ferromagnetic layer. Subsequently, precession of magnetization is resonantly excited as the frequency of AC is consistent with the FMR frequency of the ferromagnetic layer. An oscillation of the electrical resistivity due to anisotropic magnetoresistance (AMR) effect in the ferromagnetic layer leads to a rectification of the AC, which produces a direct current (DC) voltage  $V_{DC}$  appeared at the ends of the strip. In the ST-FMR,  $V_{DC}$  is measured at given external magnetic fields  $H$ . A bias-tee is used to protect the AC circuit from a damage due to the DC signals generated in the ferromagnetic layer. The external magnetic field is applied at an angle  $\varphi$  from the  $x$ -axis. The rectified voltage spectrum  $V_{DC}(H)$  in ST-FMR is given by

$$V(H) = V_s \frac{\Delta^2}{(\mu_0 H - \mu_0 H_r)^2 + \Delta^2} + V_a \frac{\Delta(\mu_0 H - \mu_0 H_r)}{(\mu_0 H - \mu_0 H_r)^2 + \Delta^2}, \quad (A1)$$

where  $H_r$  and  $\Delta$  represent the resonance field and linewidth of the spectrum, respectively.  $V_s$  and  $V_a$  are the amplitudes of the symmetric and antisymmetric Lorentzian components, respectively. When  $h_{Oe}$  and the spin polarization  $\sigma_s$  of the spin current are both parallel to the  $y$ -axis,  $V_s$  and  $V_a$  are given by

$$V_s = \frac{j_{rf} w d_{FM}}{2a\omega^+} \Delta R_{AMR} \tau_{DL} \sin 2\varphi \cos \varphi, \quad (A2)$$

$$V_a = \frac{j_{rf} w d_{FM}}{2a\omega^+} \Delta R_{AMR} \frac{\omega_2}{\omega_r} (\tau_{FL} + \tau_{Oe}) \sin 2\varphi \cos \varphi. \quad (A3)$$

Here,  $j_{rf}$ ,  $w$ ,  $d_{FM}$ ,  $\alpha$ , and  $\Delta R_{AMR}$  are the AC density, strip width, ferromagnetic layer thickness, the Gilbert damping constant, and maximum change in electric resistance due to the AMR effect, respectively. For simplicity, new symbols defined in Eqs. (A4)-(A7) are used. The spin-torque efficiency is then expressed using these symbols in Eq. (A8).

$$\omega_r = \sqrt{\omega_1 \omega_2} \quad (A4)$$

$$\omega_1 = \gamma \mu_0 H_r \quad (A5)$$

$$\omega_2 = \gamma(\mu_0 H_r + M_s) \quad (A6)$$

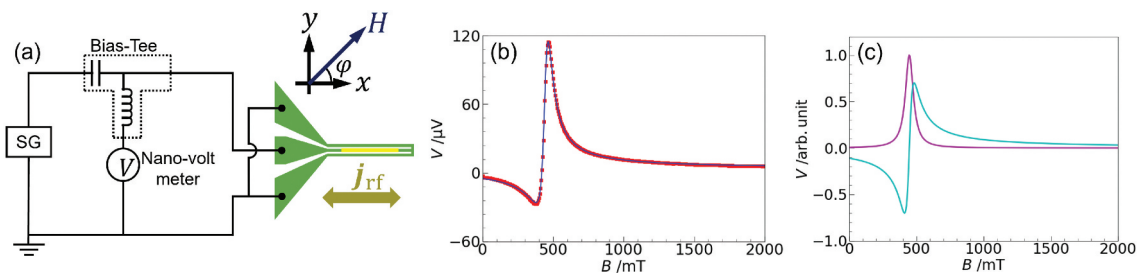
$$\omega^+ = \omega_1 + \omega_2 \quad (A7)$$

$$\xi_{FMR} = \frac{V_s}{V_a} \frac{e M_s d_{FM} d_{NM}}{\hbar} \sqrt{\frac{\omega_2}{\omega_1}} \quad (A8)$$

$$V_{s(a)} = V_{s(a)}^y \sin 2\varphi \cos \varphi + V_{s(a)}^z \sin 2\varphi \quad (A9)$$

Figure A1(b) shows a typical example of ST-FMR spectrum measured for Pt(10)/Ni<sub>95</sub>Cu<sub>5</sub>(10) bilayer, which can be well fitted by Eq. A1 as shown by solid curve. Figure A1(c) depicts symmetric and anti-symmetric Lorentzian components in the ST-FMR spectrum. The amplitudes of the symmetric and antisymmetric components,  $V_s$  and  $V_a$  exhibit an angular variation with  $\sin 2\varphi \cos \varphi$ . This arises from the angular dependence of the AMR effect ( $\sin 2\varphi$ ) and the torque that excites magnetization dynamics ( $\cos \varphi$ ). The maxima of  $V_s$  and  $V_a$ , with their  $\sin 2\varphi \cos \varphi$  dependence, occur at  $\varphi = \arcsin(\pm\sqrt{1/3})$  (approximately  $\pm 35^\circ$ ,  $\pm 145^\circ$ ), so that the ST-FMR experiments are typically conducted at  $\varphi = \pi/4$ . However, it is known that non-uniform current distribution due to asymmetric device geometry can generate an out-of-plane magnetic field component  $h_z$ , whose field torque produces a Lorentzian resonance spectrum [106]. Thus, estimating spin-torque efficiency from  $V_s$  and  $V_a$  measured at a single specific angle can lead to over- or underestimation. By fitting the symmetric component amplitude  $V_s$  and the antisymmetric component amplitude  $V_a$  to Eq. A9, which considers the angle dependence of  $V_s$  due to the out-of-plane field torque, the influence of the out-of-plane magnetic field can be separated.

Spin torque is composed of two orthogonal torques, i.e. damping-like (DL) and field-like (FL) torques. Generally, the DL and FL torque efficiencies can be evaluated from the ferromagnetic layer thickness dependence of  $\xi_{FMR}$ . The contributions of DL and FL torques due to  $y$ -polarized spin current and the  $y$ -axis oscillating magnetic field exhibit a  $\sin 2\varphi \cos \varphi$  dependence, while the torque from the out-of-



**Figure A1.** (a) Experimental setup for spin-torque FMR measurement. (b) Example of ST-FMR spectrum for Pt(10)/Ni<sub>95</sub>Cu<sub>5</sub>(10) bilayer. Blue solid curve represents the result of best fit with Eq. A1. (c) Symmetric (blue) and anti-symmetric (magenta) Lorentzian components in (b).

plane magnetic field  $h_{Oe,z}$  along the  $z$ -axis shows a  $\sin 2\phi$  dependence. The contribution of  $h_{Oe,z}$  to the symmetric spectrum amplitude  $V_s$  appears in the  $\sin 2\phi$  component. Utilizing this angular dependence, it has been confirmed that the contributions of  $\sigma_{s,y}$ ,  $h_{Oe,y}$ , and the out-of-plane magnetic field  $h_{Oe,z}$  necessary for evaluating the spin-torque efficiency can be separated [107].

## A. 2 Unidirectional spin Hall magnetoresistance (USMR) method

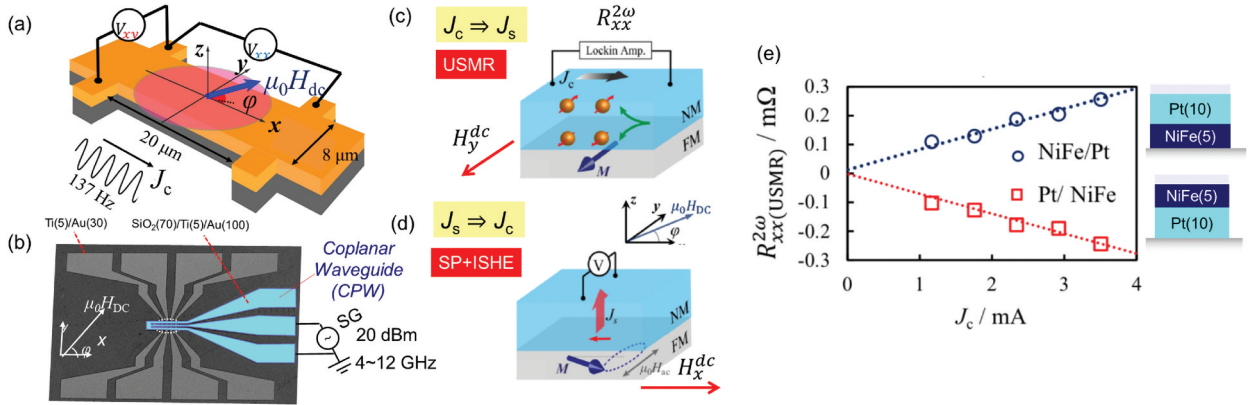
The unidirectional spin Hall magnetoresistance (USMR) effect is a nonlinear effect attributable to spin-dependent interfacial scattering of electrons caused by the spin accumulation at the interface between the ferromagnetic and nonmagnetic layers [108–112]. When an electric current is applied to the bilayer, the spin Hall effect in the NM layer leads to a spin accumulation at the interface, whose polarization depends on the current direction. The electric resistance of the FM film changes according to the polarity of the spin accumulation because of the spin-dependent sub-band structure of the FM film. Consequently, a unidirectional change in resistance (i.e. USMR signal) with respect to the current or magnetic field direction appears. The amplitude of the unidirectional change is in proportion to the product of spin Hall angle and charge current, so that we can evaluate the charge-to-spin conversion efficiency from the slope of the USMR signal as a function of charge current. From the angular dependence of the USMR signal, we can distinguish the USMR and anomalous Nernst effect owing to the thermal gradient along the conductivity gradient.

Figures A2(a) and (b) show the device configuration and measurement setup. All bilayers were patterned in the shapes of Hall bars followed by the deposition of coplanar

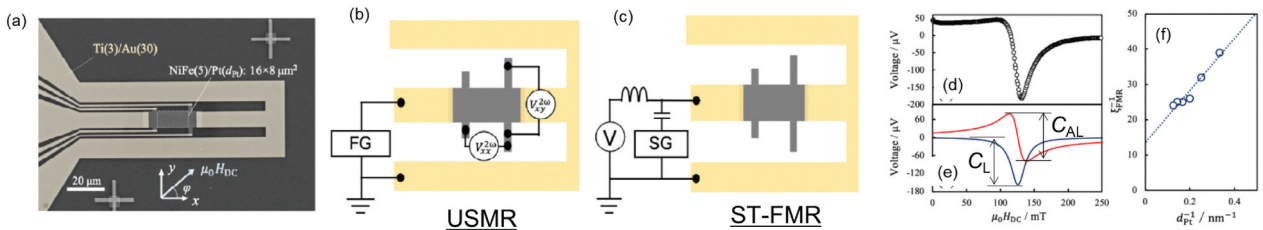
waveguide (CPW) for the spin pumping (SP) experiment. As schematically shown in Figures A2(c) and (d), the charge-to-spin conversion efficiency was evaluated using the USMR effect, where we measured the second-harmonic longitudinal resistance  $R_{2\omega}$  as a function of the in-plane orthogonal magnetic field. On the contrary, the spin-to-charge conversion efficiency was evaluated using SP and ISHE, where we measure the Hall voltage as a function of the in-plane longitudinal magnetic field.

Figures A2(e) show the USMR signals, i.e.  $R_{xx}^{2\omega}$ , for the subst./NiFe/Pt and subst./Pt/NiFe bilayers as a function of  $J_c$ .  $R_{xx}^{2\omega}$  shows linear variation, the polarity of whose slope depends on the stacking order of NiFe and Pt layers. This is attributed to that the polarization of spin accumulation is opposite between top and bottom interface of Pt layer. From an analytical expression for  $R_{xx}^{2\omega}$  derived by Zhang et al. [111], the spin Hall angle of Pt can be evaluated at 0.064 by using literature values for spin diffusion length, Fermi energy, spin asymmetry of conductivity, and spin polarization of NiFe [113,114].

For the accuracy of the evaluated charge-to-spin conversion efficiency, it is beneficial to compare the conversion efficiencies evaluated using the USMR and ST-FMR experiments for identical sample as shown in Figures A3(a-c). Similar to the general ST-FMR measurement, the DL torque efficiency was evaluated by measuring the relative amplitude of Lorentzian and anti-Lorentzian components of ST-FMR spectrum as a function of ferromagnetic layer thickness as shown in Figures A3(d-f). In a transparent limit of NiFe/Pt interface, the DL torque efficiency evaluated at 0.074 gives the spin Hall angle of Pt. This result suggests that the conversion efficiency can be correctly evaluated in both methods using Spin-torque FMR and USMR effects.



**Figure A2.** (a) Experimental setup and (b) photograph of device for USMR measurement. Schematic principles for measuring (c) charge-to-spin and (d) spin-to-charge conversions in (a). (e) USMR signals, i.e.  $R_{xx}^{2\omega}$ , for the NiFe/Pt and Pt/NiFe bilayers as a function of  $J_c$ . Preprinted from [82], copyright [2019, American Physical Society].



**Figure A3.** (a) Photograph of device fabricated for comparing the charge-to-spin conversion efficiencies evaluated using USMR and spin-torque FMR effects. Schematic setups for (b) USMR and (c) spin-torque FMR measurements. (d) Spin-torque FMR spectrum measured for NiFe/Pt bilayer film. (e) Symmetric and anti-symmetric Lorentzian components in (d). (f) Reciprocal of spin-torque efficiency as a function of reciprocal of Pt layer thickness. Preprinted from [82], copyright [2019, American Physical Society].